UC Riverside

UC Riverside Electronic Theses and Dissertations

Title

Variation of the Nebular and Stellar Dust Attenuation Curve With Physical Properties of Local and High-Redshift Star-Forming Galaxies

Permalink

https://escholarship.org/uc/item/6t4743nn

Author

Rezaee, Saeed

Publication Date

2023

Copyright Information

Peer reviewed|Thesis/dissertation

UNIVERSITY OF CALIFORNIA
RIVERSIDE

Variation of the Nebular and Stellar Dust Attenuation Curve With Physical
Properties of Local and High-Redshift Star-Forming Galaxies

A Dissertation submitted in partial satisfaction
of the requirements for the degree of

Doctor of Philosophy

in

Physics

by

Saeed Rezaee

June 2023

Dissertation Committee:

    Dr. Naveen A. Reddy, Chairperson
    Dr. George D. Becker
    Dr. Brian Siana

The Dissertation of Saeed Rezaee is approved:

_____

_____

_____

Committee Chairperson

University of California, Riverside

Acknowledgments

First and foremost, I am grateful to my mother for her unwavering commitment to my education, guiding me through every stage of my academic journey. Without your sacrifices, Mom, I wouldn't be where I am today. I also want to express my appreciation to my family for their constant belief in me and support during challenging times, especially Ali, Khalejoun, Azadeh, Roshanak, Afsaneh, Narges, Atena, Aghajoun.

My gratitude extends to my advisor, Dr. Naveen Reddy, for offering me the opportunity to learn under his guidance. Naveen, your exceptional expertise in science made me fortunate to have you as my advisor. I also want to express my heartfelt appreciation to Tara Fetherolf, my mentor, and postdoc advisor. Tara, your unwavering support has been invaluable, and I couldn't have asked for a better mentor. You were there for me during an extremely difficult period in my life, and that is something I will always remember. I also want to thank Irene, AliAhmad, Najmeh, and Shariar for their essential research advice and generous assistance throughout my journey.

Most importantly I want to thank my friends from back at home who were not with me in Riverside but have always supported me throughout this journey. Negin, Sadegh, Amirreza, Fati, Pouya, and Kimia, I am most grateful to have such wonderful friends. Lastly, during my time in Riverside, I was fortunate to meet many wonderful and supportive friends. Aisa, it's hard to put into words just how lucky I am to have you always there for me - and I am sure you will stick by my side, no matter what. Leyli, your impact on my life is immeasurable - you are a true gem. And Mahi, even though we became friends during my final few months in Riverside, your warm kindness has made a significant, enduring

difference in my life. I also want to thank some of my most amazing friends, Shakiba, Nami, Farima, Joobin, Kavoosi, Sahar, Toktam, Samantha, Nika, Shahneh, Nasim, Soroush B, and Sadaf.

had within the indigenous Hawaiian community. We are most fortunate to have the opportunity to conduct observations from this mountain. In conducting the analyses for this dissertation, I acknowledge the use of the following open source Python packages: Numpy (Oliphant 2007a), Astropy (The Astropy Collaboration et al. 2013; Collaboration et al. 2018), Matplotlib (Hunter 2007), SciPy (Oliphant 2007b), specline (Shivaei et al. 2018a), and adaptive Voronoi binning code (Cappellari & Copin 2003).

ABSTRACT OF THE DISSERTATION

Variation of the Nebular and Stellar Dust Attenuation Curve With Physical Properties of
Local and High-Redshift Star-Forming Galaxies

by

Saeed Rezaee

Doctor of Philosophy, Graduate Program in Physics
University of California, Riverside, June 2023
Dr. Naveen A. Reddy, Chairperson

Dust attenuation refers to the absorption and scattering of light by interstellar dust particles
within a galaxy. This effect, which depends on wavelength, is also known as dust redden-
ing due to its more pronounced impact on shorter wavelengths. Studying dust attenuation
is important in the field of galaxy evolution as it helps astronomers to gain insight into
various aspects of galaxy formation such as accurate measurements of galaxy properties,
star formation history, metallicity and chemical evolution, galaxy morphology and classi-
fication. Dust extinction/attenuation curves are used to express the dependency of dust
reddening on wavelength. I use the spectroscopic data from SDSS, MOSDEF, and MOS-
DEF/LRIS surveys to constrain the nebular and stellar dust attenuation curves and explore
their variations with physical properties of the local and high-redshift ($z \sim 2$) star-forming
galaxies.

My dissertation aims to examine how nebular and stellar attenuation curves relate
to physical properties of a galaxy including stellar mass, star formation rate, and metallic-
ity. To accomplish this, I utilize techniques such as the Balmer decrement and reconciling

various Hα− and SED-based star formation rates. The motivation for examining nebular attenuation curves stems from evidence suggesting a more significant reddening for nebular emission lines compared to the stellar continuum. This disparity could be due to the presence of dust grains with distinct size and mass properties in nebular regions, resulting from strong radiation fields around massive stars. Additionally, the dust/star geometry might differ between nebular and stellar regions. We use the spectroscopic data with availability of the first four Balmer emission lines from the SDSS survey and derive the nebular attenuation curve for a sample of 78,340 galaxies. Our results suggest that the nebular curve does not exhibit variations with respect to stellar mass, star formation rate, or metallicity.

Stellar dust attenuation curve plays a crucial role in modeling stellar populations within galaxies. These models are essential for understanding the formation and evolution of galaxies and require accurate accounting for dust attenuation effects on various stellar populations. Employing a sample of 412 star-forming galaxies with MOSFIRE optical spectra and BPASS models, we identify optimal model combinations for reconciling Hα and SED-based SFRs, finding sub-solar metallicity populations with SMC reddening provide the best agreement. We also explore stellar dust attenuation curve variations with stellar mass in 124 galaxies using Keck/LRIS far-UV spectra, revealing consistent average metallicities and the SMC curve as the best match for SFRs across both low- and high-mass galaxies.

Another focus of my dissertation is to test whether the Hα-to-UV luminosity ratio ($L(\mathrm{H}\alpha)/L(\mathrm{UV})$) is a reliable tracer of bursty star-formation histories (SFHs) of star-forming galaxies. Verifying the reliability of the Hα-to-UV ratio in tracing burstiness is crucial for accurately characterizing the star formation history of galaxies, interpreting observa-

tional data, and refining our understanding of galaxy formation and evolution. We analyze $L(\mathrm{H}\alpha)/L(\mathrm{UV})$ for 310 star-forming galaxies in two redshift bins from the MOSFIRE Deep Evolution Field (MOSDEF) survey. Using CANDELS/3D-HST imaging, we construct star-formation-rate surface density (Σ_{SFR}) and stellar age maps and examine far-UV spectra from a 124-galaxy subsample. Our results show no significant evidence of bursty star formation based on Σ_{SFR} distributions within a galaxy. We identify two populations with low and high average $L(\mathrm{H}\alpha)/L(\mathrm{UV})$ ratios, but find no variations in age-sensitive FUV spectral features. Thus, we cannot conclusively confirm the reliability of the $L(\mathrm{H}\alpha)/L(\mathrm{UV})$ ratio in tracing burstiness for ensembles of star-forming galaxies at $z \sim 2$. We introduce alternative tracers of recent star-forming activities, such as the equivalent widths of SiIV $\lambda\lambda 1393, 1402$, CIV $\lambda\lambda 1548, 1550$ P-Cygni, and HeII $\lambda 1640$ stellar wind features, which are less susceptible to uncertainties known to impact the reliability of the $L(\mathrm{H}\alpha)/L(\mathrm{UV})$ ratio. These tracers provide valuable insights into the properties of massive stars, stellar winds, and their surrounding environments. By using multiple indicators of recent star formation, we can gain a more comprehensive understanding of the star-forming activities in galaxies and reduce potential biases introduced by using a single metric like the $L(\mathrm{H}\alpha)/L(\mathrm{UV})$ ratio.

Contents

List of Figures

Chapter 1

Introduction

1.1 Dust Attenuation Curve

The study of the interstellar medium (ISM) is crucial for understanding the processes that drive the evolution of galaxies, including the formation and distribution of stars and planetary systems. One of the key components of the ISM is dust, which is predominantly composed of small particles of silicate and carbonaceous materials. The grain sizes typically range from a few nanometers to a few micrometers. In part of this dissertation, we present a comprehensive study of ISM dust obscuration, investigating its impact on observations and astrophysical processes in different environments.

Dust extinction and/or attenuation curve express the relationship between dust obscuration and wavelength. The derivation of extinction curves involves factors like the chemical composition and size distribution of dust grains, and these curves can be obtained by directly observing light that has traversed a dust screen along a particular line of sight. Attenuation curves represent the cumulative effect of dust obscuration on a group of stars,

taking into account the specific geometry between the stars and dust (Draine 2003). Extinction curves for the Milky Way (MW) and nearby galaxies, including the Large and Small Magellanic Clouds and M31, have been investigated by assessing the extinction across individual sightlines (e.g., Nandy et al. 1975, 1980; Rocca-Volmerange et al. 1981; Bianchi et al. 1996a; Clayton 2020). The average extinction curves for these galaxies are calculated by combining the individual sightlines (e.g., Seaton 1979; Prevot et al. 1984; Cardelli et al. 1989b; Pei 1992; Gordon et al. 2003a; Fitzpatrick & Massa 2007). Notably, the extinction curves derived from different sightlines within a galaxy, as well as the average curves for distinct galaxies, exhibit significant differences in both UV bump strengths and optical/UV slopes as some of them are shown in Figure 1.1.

The standard approach for determining the attenuation of nebular emission and stellar continuum in galaxies involves assuming different attenuation curves for each. This assumption arises from the fact that young and massive stars, which primarily contribute to nebular emission, are preferentially located in areas with higher dust covering fractions (e.g., for low-redshift galaxies: Johnson et al. 2007, Wild et al. 2011a, Battisti et al. 2016, Battisti et al. 2017, and for high-redshift samples: Kriek & Conroy 2013, Zeimann et al. 2015, Reddy et al. 2015, Salmon et al. 2016, Shivaei et al. 2020a). In addition, nebular regions may contain dust grains with different sizes and mass properties due to the strong radiation of massive stars (Draine 2003). And, the dust-star geometry may differ between the nebular and less-reddened stellar population regions. Thus, studying the variation of the dust attenuation curve is critical.
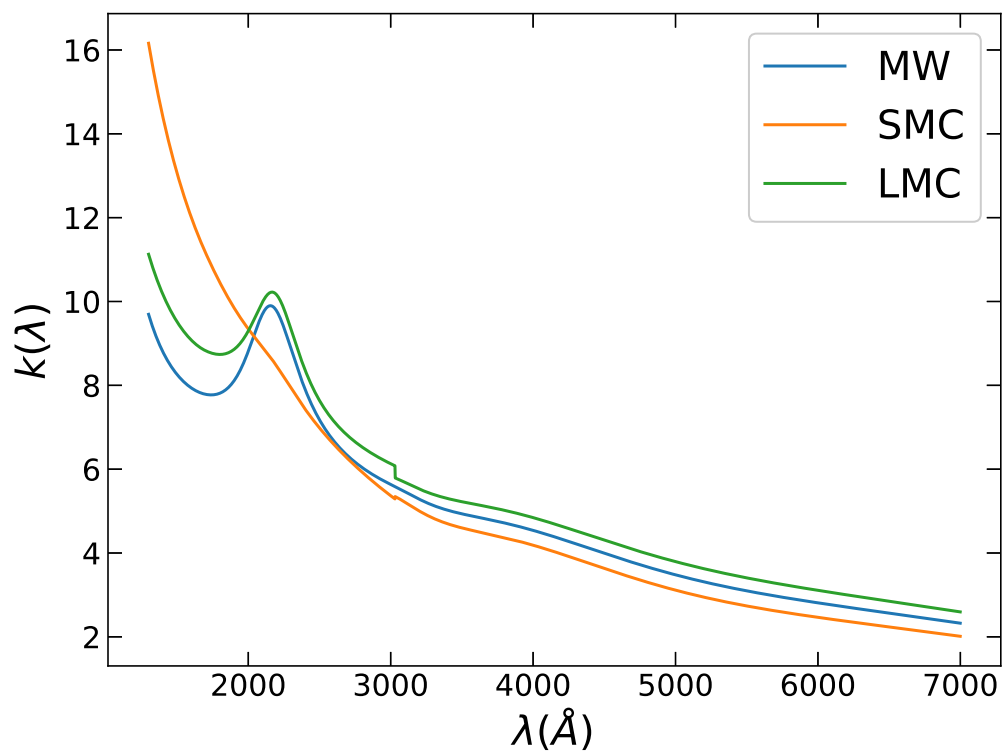
Figure 1.1: Comparison of the shape of the attenuation curve derived for the Milky Way, SMC , and LMC (Cardelli et al. 1989a; Fitzpatrick & Massa 1990a; Gordon et al. 2003a).

1.2   Star-formation History

Understanding how galaxies build their stellar mass over time is crucial for gaining insights into the process of galaxy formation and evolution. The rate at which a galaxy forms new stars is called the star formation rate (SFR). Star formation histories (SFHs) describe how the rate of star formation in a galaxy changes over time. The most commonly assumptions of the SFH are continuous and bursty star formation. In continuous star formation a galaxy forms stars at a relatively constant rate throughout its lifetime. Bursty star formation assumes that the star formation occurs in discrete bursts separated by periods of quiescence.

The star-forming main sequence (SFMS) represents a tight correlation between SFR and stellar mass of galaxies at a given redshift. However, a subset of galaxies exhibit significant deviations from this relationship, particularly those with elevated SFRs for their stellar mass. These so-called starburst galaxies can be attributed to various factors, including galaxy interactions and mergers, gas-rich environments, localized star formation events, and stochastic variations. One of the commonly used tracer of burstiness is Hα-to-UV luminosity ratio. Hα recombination line and FUV continuum are sensitive to star formation at different timescales. While the former is more sensitive to ongoing star formation within a timescale of $5-10\,\mathrm{Myr}$, the latter trace star formation on longer timescales of $\sim 100\,\mathrm{Myr}$. During and after a burst of star formation Hα emission increases and declines faster than the FUV continuum causing changes to the Hα-to-UV ratio from its equilibrium value. Although there exist other factors that affect the Hα-to-UV ratio such as variations in the ionizing photon production rate per unit SFR (Steidel et al. 2001; Shapley et al. 2006; Siana

et al. 2007), nebular and stellar dust reddening (Kewley et al. 2002; Lee et al. 2009; Reddy et al. 2012; Reddy et al. 2015; Shivaei et al. 2015, 2018a; Theios et al. 2019; Fetherolf et al. 2021), stellar metallicity (Bicker & Fritze-v. Alvensleben 2005; Boselli et al. 2009), and the relative optical depths of UV and Hα emission. Hence, it is important to validate the effectiveness of Hα-to-UV ratio against other indicators.

1.3 Dissertation Outline

This thesis is divided into three primary sections and structured as follows. Chapter 2 focuses on deriving the average nebular attenuation curve for a sample of local star-forming galaxies at $z \sim 0.04 - 0.1$. For the work presented in Chapter 2, we use the Sloan Digital Sky Survey data release 8 (Aihara et al. 2011). Our sample is constructed using the publicly available Galspec catalogs provided by the MPA/JHU group (Kauffmann et al. 2003; Brinchmann et al. 2004; Tremonti et al. 2004b) and includes 78,340 galaxies. Chapter 3 is a study of $z \sim 2$ star-forming galaxies which uses the MOSFIRE Deep Evolution Field (MOSDEF; Kriek et al. 2015), CADELS/3D-HST (Brammer et al. 2012; Skelton et al. 2014; Momcheva et al. 2016), and MOSDEF/LRIS (Topping et al. 2020; Reddy et al. 2022) surveys to examine the reliability of the globally-measured Hα-to-UV luminosity ratio in tracing bursty SFH. Chapter 4 presents a study of MOSDEF and MOSDEF/LRIS star-forming galaxies with the aim of exploring the variation of the shape of the stellar dust attenuation curve with stellar metallicity and stellar mass through the observed and model-based SFR reconciliation.

Chapter 2

Paper I: Variation of the Nebular Dust Attenuation Curve with the Properties of Local Star-forming Galaxies

Abstract We use a sample of $78,340$ star-forming galaxies at $z \simeq 0.04 - 0.1$ from the SDSS DR8 survey to calculate the average nebular dust attenuation curve and its variation with the physical properties of galaxies. Using the first four low-order Balmer emission lines ($\mathrm{H}\alpha, \mathrm{H}\beta, \mathrm{H}\gamma, \mathrm{H}\delta$) detected in the composite spectrum of all galaxies in the sample, we derive a nebular attenuation curve in the range of $0.41\,\mu\mathrm{m}$ to $0.66\,\mu\mathrm{m}$ that has a similar

---

shape and normalization to that of the Galactic extinction curve (Milky Way curve), the SMC curve and the nebular attenuation curve derived recently for typical star-forming galaxies at $z \sim 2$. We divide the galaxies into bins of stellar mass, gas-phase metallicity, and specific star-formation rate, and derive the nebular attenuation curve in each of these bins. This analysis indicates that there is very little variation in the shape of the nebular dust attenuation curve with the properties used to bin the galaxies, and suggests a near universal shape of the nebular dust attenuation curve at least among the galaxies and the range of properties considered in our sample.

2.1   Introduction

Many of the key inferred physical properties of galaxies are sensitive to the effects of dust. For instance, the use of the unobscured rest-frame UV light from massive young stars or the nebular emission lines to estimate star formation rate (SFR) must be accompanied by a proper dust correction to account for the light absorbed and re-radiated by dust (e.g., Kennicutt 1998; Kennicutt et al. 2009; Hao et al. 2011; Kennicutt & Evans 2012a). In general, the dust corrections applied to the stellar continuum may differ from those applied to nebular lines because the sightlines to HII regions may have a different distribution of dust (or dust with different properties) compared to sightlines towards non-ionizing stellar populations. (Calzetti et al. 1994; Charlot & Fall 2000a). Nebular regions may contain dust grains with different size and mass properties (Draine 2003) because of the presence of the strong radiation fields around massive stars (Martínez-González et al. 2017; Hoang et al. 2019). In addition, many studies have found a larger reddening for nebular emission

lines versus the stellar continuum (e.g., Fanelli et al. 1988; Calzetti 1997; Calzetti et al. 2000a; Förster Schreiber et al. 2009a; Yoshikawa et al. 2010; Wild et al. 2011a; Wuyts et al. 2011; Kreckel et al. 2013; Kashino et al. 2013a; Wuyts et al. 2013; Price et al. 2014; Reddy et al. 2015; De Barros et al. 2016; Buat et al. 2018; Koyama et al. 2019; Shivaei et al. 2020a). Thus, knowledge of the dust geometry and properties in different regions within galaxies is crucial for identifying and applying the appropriate dust corrections. The dust extinction/attenuation curves provide invaluable information on dust properties and dust distribution (Draine & Li 2007).

Extinction curves have been studied for the Milky Way (MW) and nearby galaxies, such as the Large and Small Magellanic Clouds and M31, by measuring the extinction along individual sightlines (e.g., Nandy et al. 1980, 1975; Rocca-Volmerange et al. 1981; Bianchi et al. 1996b; Clayton et al. 2015). The average total extinction curves for these galaxies are determined by combining these individual sightlines (Seaton 1979; Prevot et al. 1984; Cardelli et al. 1989b; Pei 1992; Gordon et al. 2003a; Fitzpatrick & Massa 2007). There are major differences between the extinction curves derived for different sightlines within a galaxy and also the average curves for different galaxies. For example, Fitzpatrick & Massa (1990b) showed a broad range of extinction curves for various Milky Way sight lines. In addition, comparing the average curves derived for the Milky Way (Cardelli et al. 1989b), Magellanic clouds (Fitzpatrick & Massa 2007; Gordon et al. 2003a), and M31 (Bianchi et al. 1996b) shows variations in both UV/optical slope and strength of the UV bump (a broad extinction feature of the curve near 2175 Å). For external galaxies, extinction curves cannot be directly measured due to limited spatial resolution. Nevertheless, one

can compute attenuation curves that reflect the average wavelength dependence of dust obscuration and which depend on both the properties of the dust and the geometry of that dust with respect to the stars (Charlot & Fall 2000a; Calzetti 2001; Weingartner & Draine 2001; Li & Draine 2001; Conroy et al. 2010a; Conroy 2013; Chevallard et al. 2013; Kriek & Conroy 2013; Reddy et al. 2015; Shivaei et al. 2020a; Buat et al. 2011, 2012a). A wide range of attenuation curves that apply to the stellar continuum have been derived with different UV bump strengths and optical/UV slopes (Calzetti et al. 2000a; Conroy et al. 2010b; Chevallard et al. 2013; Reddy et al. 2015; Salim et al. 2018). Many of these same studies, as well as others, have suggested that these variations in the stellar attenuation curve may be correlated with certain properties of galaxies, including their stellar mass, SFR, and metallicity (e.g., for low-redshift galaxies: Johnson et al. 2007, Wild et al. 2011a, Battisti et al. 2016, Battisti et al. 2017, and for high-redshift samples: Kriek & Conroy 2013 , Zeimann et al. 2015, Reddy et al. 2015, Salmon et al. 2016, Shivaei et al. 2020a). In parallel, theoretical work has explored the variation in curves due to dust-star geometry and age (Witt & Gordon 2000; Weingartner & Draine 2001; Narayanan et al. 2018a).

On the other hand, despite very recent work in quantifying the shape of the nebular dust attenuation curve at high redshift (Reddy et al. 2020, hereafter refer to as R20), there is little information on how the shape of the nebular curve may vary from galaxy-to-galaxy and with galaxy properties. The shape of the nebular dust curve is critical to inferring several important physical parameters of the ISM including gas-phase metallicity, ionization parameters, and star-formation rate derived from Balmer lines. The MW curve (Cardelli et al. 1989b) is preferred to correct the nebular lines for the dust extinction as

it is derived based on the sightline measurements of nebular regions (Calzetti et al. 1994; Wild et al. 2011b; Liu et al. 2013; Salim & Narayanan 2020). Additionally, R20 found that the nebular attenuation curve for high-redshift galaxies is similar to that of the MW at rest-frame optical wavelengths. However, the small sample size in that work prevented a detailed study of how the nebular dust attenuation curve varies with galaxy properties. To better understand the conditions that may shape the nebular attenuation curve, we take advantage of a large sample of local star-forming galaxies for which the nebular attenuation curve can be inferred.

In this paper, we derive the nebular attenuation curve for local star-forming galaxies and examine its variation with stellar mass, specific SFR (sSFR), and gas-phase abundances, with the goal of understanding how these properties may influence the shape of the nebular attenuation curve, and hence dust properties and geometry, as a function of these properties. The initial work of R20 laid the foundation for deriving the nebular attenuation curve for high-redshift galaxies. Here, we expand upon this work by examining the variation of the curve with stellar mass, sSFR, and oxygen abundance using a large sample of local star-forming galaxies drawn from the SDSS. The large sample size allows us to group the galaxies by various properties and still retain a sufficient number of galaxies in each bin to robustly derive the nebular attenuation curve.

The structure of this paper is as follows. In Section 4.2, we outline the sample used in this work. Section 2.3 presents the approach to constructing composite spectra. Section 2.4 describes the method used to derive the shape of the nebular attenuation curve. Section 2.5 discusses the comparison between the nebular attenuation curves derived for
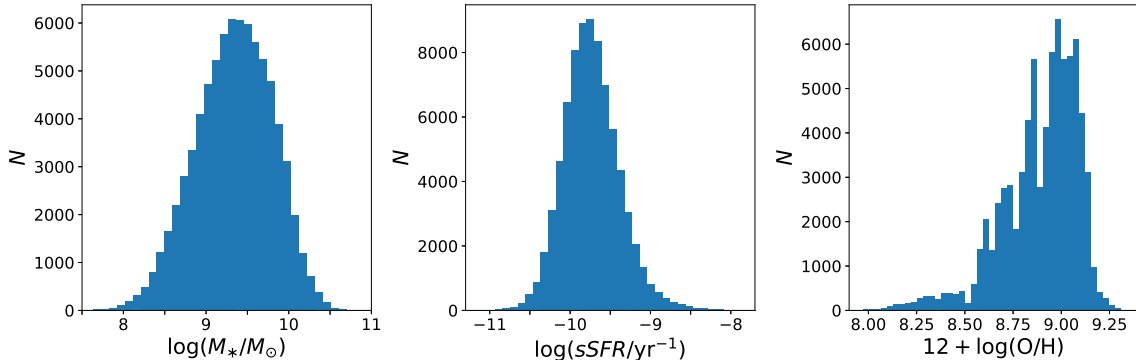
Figure 2.1: Distribution of stellar mass (left), sSFR(middle), and gas-phase metallicity (right) of the sample analyzed in this work, and includes a total of $78,340$ low-redshift star-forming galaxies from the SDSS.

each subsample in stellar mass, metallicity, and sSFR. Section 2.6 presents a discussion of the variation of the curve with the aforementioned properties. We adopt a cosmology with $H_0 = 70\,\mathrm{km\,s^{-1}\,Mpc^{-1}}$, $\Omega_\Lambda = 0.7$, and $\Omega_\mathrm{m} = 0.3$. All wavelengths are presented in the vacuum frame.

2.2 sample

In this study, we use optical spectroscopic observations of galaxies from the Sloan Digital Sky Survey Data Release 8 (Aihara et al. 2011). Our sample is constructed using the publicly-available *Galspec* catalogs provided by the MPA/JHU group (Kauffmann et al. 2003; Brinchmann et al. 2004; Tremonti et al. 2004a), and includes $78,340$ galaxies, all meeting the following criteria:

- **(i) Only star-forming galaxies**: galaxies that lie below the active galactic nucleus (AGN) demarcation line of Kauffmann et al. (2003).

- **(ii) A redshift range of** $0.04 \leq z \leq 0.1$: to ensure that the portion of galaxy which

    is measured inside the fiber aperture is reasonably representative of the entire galaxy.

The *Galspec* catalogs include emission line measurements and inferences of galaxy properties. We refer the reader to Aihara et al. (2011) for further details. In brief, line fluxes are corrected for the effect of stellar absorption using Bruzual & Charlot (2003) stellar population synthesis models. The measurements of individual galaxy properties correspond to those obtained for the $3''$ SDSS fiber, and include stellar mass, sSFR, and gas-phase abundances. Stellar masses are based on fitting stellar population models to *ugriz* photometry, and assume a Kroupa (2001) initial mass function. Gas-phase abundance $(12 + \log(\text{O/H}))$, hereafter referred to as the metallicity, are calculated from the strong optical emission lines ([OII]λ3727, Hβ, [OIII]λ5007, [NII]λ6548, 6584, and [SII]λ6717, 6731) using the Bayesian methodology from Tremonti et al. (2004a), and Brinchmann et al. (2004). Star-formation rates are based on dust-corrected Hαemission as described in Brinchmann et al. (2004). The sample used in this work spans the following range in physical properties: $6.68 < \log(M_*/M_\odot) < 11.46$, $-11.79 < \log(\text{sSFR/yr}^{-1}) < -7.05$, and $7.85 < 12 + \log(\text{O/H}) < 9.40$. Figure 2.1 shows the distribution of the physical properties of galaxies in this sample.
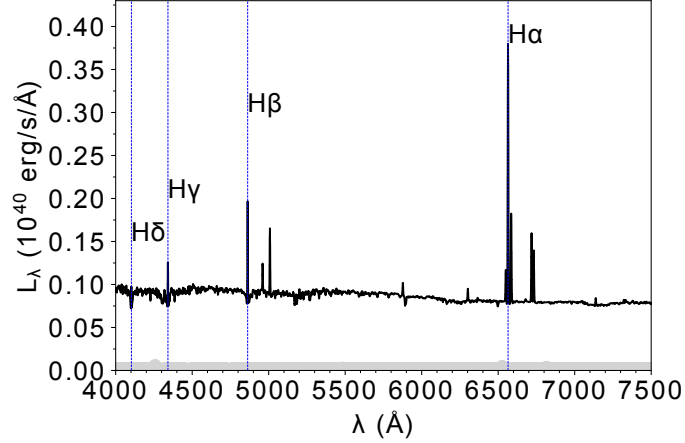
Figure 2.2: The composite spectrum constructed for all the galaxies in sample shown in black. The grey region indicates the $\pm 1\sigma$ uncertainty in the spectrum. Hα, Hβ, Hγ, and Hδ emission lines are indicated by blue dotted lines.

2.3   composite spectrum

2.3.1   Methodology of Constructing the Composite Spectrum

We use composite spectra in order to measure the weaker Balmer lines including Hγ and Hδ, which are typically not detected in the spectra of individual galaxies. The composite spectra are constructed by averaging, or stacking, the spectra of individual galaxies using the procedures given in R20 and **specline**[1] (Shivaei et al. 2018b). In brief, the science and error spectrum of each galaxy are shifted to the rest-frame based on the spectroscopic redshift, converted to luminosity density, and interpolated to a wavelength grid with spacing of 0.4 Å. The composite spectrum at each wavelength is calculated as an average of the luminosity densities of individual spectra that are weighted by their inverse variance. The error in the composite spectrum is derived using bootstrap resampling, where we randomly selected 2000 objects from the sample, perturbed their spectra according to the error spectra, and

---

[1] https://github.com/IreneShivaei/specline/
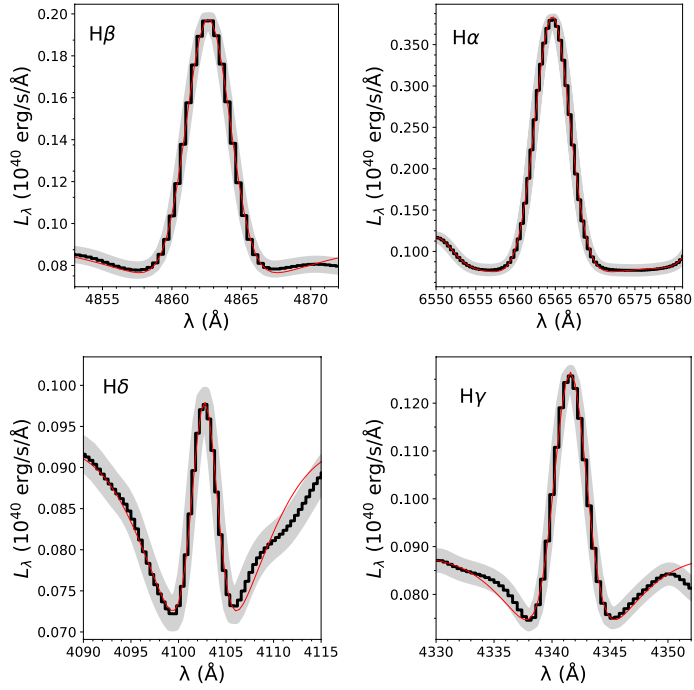
Figure 2.3: $H\alpha, H\beta, H\gamma, H\delta$ emission lines observed in the composite spectrum of all galaxies in the sample, shown in black. The red lines show the best-fit Gaussian models that account for both emission and absorption for each line. The gray filled bands show the 1σ uncertainty of the spectrum.

reconstructed the composite spectrum from these realizations. This process is repeated many times, and the resulting standard deviation in luminosity densities at each wavelength point gives the composite error spectrum. Figure 3.5 shows the composite spectrum and its error constructed for the 78, 340 objects in the sample.

Table 2.1: Luminosity (L) measurements

Line[a]	$L(10^{40}\mathrm{erg/s})$[b]	Fitting Window (Å)[c]
Hα	1.743 ± 0.0017	$6442 - 6692$
Hβ	0.5062 ± 0.0026	$4813 - 4913$
Hγ	0.2088 ± 0.0010	$4265 - 4416$
Hδ	0.1040 ± 0.0016	$4015 - 4200$

[a] Balmer Recombination Lines

[b] Luminosity and its error measured from the composite spectrum. Error in the line luminosity measured using the Monte Carlo method discussed in Section 2.3.2.

[c] Wavelength range over which the lines are fit.

2.3.2 Measurements of the Balmer emission lines from the composite spectrum

$H\alpha, H\beta, H\gamma$, and $H\delta$ emission lines (Figure 2.3) are measured from the stacked spectrum. We chose not to include the $H\epsilon$ emission line ($\lambda = 3971.20$ Å) in our analysis as it is blended with, and not well-resolved from, the [NeIII]$\lambda 3969$ line.

All lines have been measured by fitting two Gaussian functions, one to the absorption and one to the emission line except for the $H\alpha$ line. $H\alpha$ is fit simultaneously along with the [NII] doublet and the underlying Balmer absorption. The velocity widths used to fit the $H\beta$, $H\gamma$, and $H\delta$ emission lines were constrained to be within the 20% of the width obtained for $H\alpha$. The Balmer absorption measured from the composite spectrum is consistent with those inferred from the stellar population models (Bruzual & Charlot 2003, $Z = 0.020$ "solar") that best fit the broadband photometry of galaxies contributing to the composite spectrum. The luminosity uncertainties are calculated by perturbing the stacked spectrum according to its error spectrum and remeasuring the line luminosities many times using the same method described in this section. The standard deviation of the values obtained in these iterations is adopted as the luminosity error. Table 2.1 reports the measured line luminosities from the composite spectrum for the entire sample.

2.4 Shape of the Nebular Attenuation Curve

2.4.1 Definitions

Here we discuss the methodology for determining the shape of the nebular attenuation curve. The intrinsic Balmer line ratios reported in Table 2.2 are well determined and

depend weakly on the local conditions such as electron density and temperature. The typical conditions assumed for the intrinsic $H\alpha/H\beta$ ratio are $n_e = 100 \text{ cm}^{-3}$ and $T_e = 10000$ K (Osterbrock 1989). The relationship between the observed luminosity, $L(\lambda)$, and the intrinsic luminosity, $L_0(\lambda)$, can be expressed as follows:

$$L(\lambda) = L_0(\lambda) \times 10^{-0.4A(\lambda)}, \tag{2.1}$$

where $A(\lambda)$ is the attenuation in magnitudes at wavelength λ. The total nebular dust attenuation curve is defined as $k(\lambda)$:

$$k(\lambda) = \frac{A(\lambda)}{E(B-V)_{\text{neb}}}, \tag{2.2}$$

where $E(B-V)_{\text{neb}} = A(B) - A(V)$ is defined as the color excess . The B and V bands are taken to be at 4400 Å and 5500 Å, respectively.

2.4.2   Methodology

We use the methodology introduced by R20 to calculate the shape of the nebular attenuation curve. In brief, R20 expressed the attenuation in magnitudes relative to $H\alpha$ as follows:

$$A'(\lambda) = 2.5 \left[\log_{10}\left(\frac{L(H\alpha)}{L(\lambda)}\right) - \log_{10}\left(\frac{L_0(H\alpha)}{L_0(\lambda)}\right)\right] + 1, \tag{2.3}$$

where $L(H\alpha)/L(\lambda)$ is the observed ratio of the $H\alpha$ luminosity to that of a higher-order Balmer line ($H\beta$, $H\gamma$, $H\delta$), $L_0(H\alpha)/L_0(\lambda)$ denotes the intrinsic ratio, and $A'(\lambda)$ is equivalent

Table 2.2: Balmer Line Ratios

Line[a]	λ (Å)[b]	Line Ratios (Å)[c]
Hα	6564.60	2.860
Hβ	4862.71	1.000
Hγ	4341.69	0.468
Hδ	4102.89	0.259

[a] Balmer Recombination Lines.

[b] Rest-frame Vacuum wavelength.

[c] Intensity of line relative to Hβ for Case B recombination, $n_{\mathrm{e}} = 10^2$ cm^{-3} and $T_{\mathrm{e}} = 10^4$ K (Osterbrock 1989).
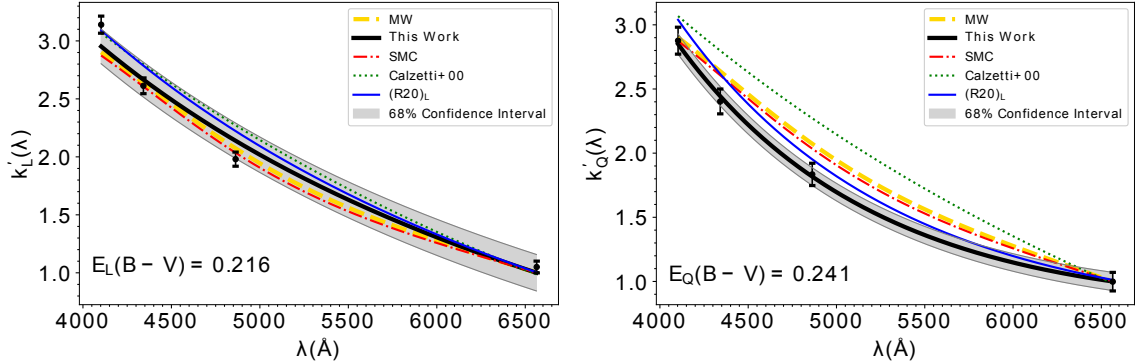
Figure 2.4: Average nebular dust attenuation curve, $k'(\lambda)$, versus λ, for the linear (left) and quadratic (right) polynomial forms. Attenuation curve measurements are shown by black circles along with their error bars. The best fit 68% confidence intervals are shown by grey region and grey lines. For comparison, the MW extinction curve, SMC, Calzetti et al. (2000a) and the curves derived in R20 are shown and have been shifted, to have the same value at the wavelength of Hα as the curves derived here. The subscripts used for R20 refers to the curves based on fitting a linear or quadratic function. As it is indicated in the figure above, the reddening, $A'(4400$ Å$) - A'(5500$ Å$)$, calculated by the linear form of the $A'(\lambda)$ is $\sim 10\%$ smaller than the one obtained by the quadratic form.

to $A(\lambda) + [1 - A(\text{H}\alpha)]$. The line luminosities measured from the composite spectrum are then used in conjunction with Equation 2.3 to calculate the attenuation in magnitudes (relative to Hα) for each of the higher-order Balmer lines. We then fit linear and quadratic functions to $A'(\lambda)$.

The shape of the attenuation curve, $k'(\lambda)$, can be related to $A'(\lambda)$ as follows:

$$
\begin{aligned}
k'(\lambda) &\equiv \frac{A'(\lambda)}{A'(4400 \text{ Å}) - A'(5500 \text{ Å})} \\
&= k(\lambda) + \frac{[1 - A(\text{H}\alpha)]}{E(B-V)_{\text{neb}}}.
\end{aligned} \tag{2.4}
$$

Note that $k'(\lambda)$ and $k(\lambda)$ differ by an offset of $[1 - A(\text{H}\alpha)]/E(B-V)_{\text{neb}}$ which is independent of λ. Therefore, $k'(\lambda)$ and $k(\lambda)$ are equivalent except for a normalization factor. In order to calculate $k'(\lambda)$, $A'(4400$ Å$) - A'(5500$ Å$)$ is determined using linear-in-$1/\lambda$

$(A'(\lambda) = a_0 + a_1/\lambda)$ and quadratic-in-1/λ $(A'(\lambda) = a_0 + a_1/\lambda + a_1/\lambda^2)$ fits to $A'(\lambda)$, and then $k'(\lambda)$ is computed using Equation 2.4. Next, we use the linear and quadratic polynomial forms discussed above to fit $k'(\lambda)$ vs. λ. More complicated functional forms are not considered due to the limited number of data points available to derive the attenuation curve. The uncertainty in a given $k'(\lambda)$ point is propagated throughout these calculations. The line ratios measurements are perturbed according to their errors, then $A'(\lambda)$, $E(B-V)_{\mathrm{neb}}$ and $k'(\lambda)$ are recalculated many times to then determine the propagated measurement uncertainty in a given $k'(\lambda)$ point. The functional forms of the attenuation curves are:

$$k'_{\mathrm{L}}(\lambda) \;\; = \;\; -2.253 + \frac{2.135}{\lambda}, \tag{2.5}$$

$$k'_{\mathrm{Q}}(\lambda) \;\; = \;\; 2.705 - \frac{3.083}{\lambda} + \frac{1.290}{\lambda^2}, \tag{2.6}$$

where λ is in units of μm, in the range $0.41 \leq \lambda \leq 0.66\,\mu$m. Note that $k'_{\mathrm{L}}(\lambda)$ and $k'_{\mathrm{Q}}(\lambda)$ denote the curves based on fitting a linear-in-1/λ and quadratic-in-1/λ function, respectively, and the curves are all normalized such that their values at the wavelength of Hα is equal to one to aid in comparing them with other curves in the literature. We consider both the linear and quadratic functions to demonstrate the associated systematic uncertainty in the resulting nebular attenuation curve.

The nebular attenuation curve derived here is shown in Figure 2.4. The Galactic extinction curve (Cardelli et al. 1989b), Calzetti et al. (2000a) curve, SMC, and the nebular curves derived for redshift $z \sim 2$ galaxies in R20 are also shown in Figure 2.4. The MW curve is typically used for the extinction correction of nebular lines, while Calzetti et al.

([2000a](#)) and SMC are often used for the reddening of the stellar continuum in high-redshift galaxies. Figure [2.4](#) shows that the average nebular dust attenuation curve derived for low-redshift star-forming galaxies is similar to the nebular curves presented in [R20](#) within 1σ, the MW and SMC curves within 2σ confidence. These results imply that the combined effects of dust properties and geometry yield a shape of the curve that is similar to other common extinction and attenuation curves at rest-frame optical wavelengths. We do not have sufficient information to disentangle changes in dust properties and geometry, and radiation transfer models indicate that curves of similar shape can be produced by dust distributions with substantially different properties (e.g., [Witt & Gordon 2000](#); [Seon & Draine 2016](#)). Note that there are small differences in $k'_\mathrm{L}(\lambda)$ and $k'_\mathrm{Q}(\lambda)$ because the values of $A'(4400\,\text{Å})$ and $A'(5500\,\text{Å})$ depend on the functional form (i.e., linear or quadratic) used to determine these values.

To obtain the normalized total nebular dust attenuation curve $k(\lambda)$ (Equation [2.2](#)) from $k'(\lambda)$ (Equation [2.4](#)), $k'_\mathrm{L}(\lambda)$ is extrapolated to $\lambda = 2.8\,\mu\text{m}$, corresponding to the wavelength at which other common curves (e.g., MW, SMC, and LMC) approach zero ([Gordon et al. 2003a](#); [Reddy et al. 2015](#)). Similarly, $k_\mathrm{Q}(\lambda)$ is assumed to have the same functional behavior as $k_\mathrm{L}(\lambda)$ at long wavelength. Therefore, $k_\mathrm{Q}(\lambda)$ is normalized such that it is equal to $k_\mathrm{L}(\lambda)$ at $\lambda = 0.66\,\mu\text{m}$ in order to obtain a continuous function. The final form of $k(\lambda)$ is:

$$
k_\mathrm{L}(\lambda) = -0.762 + \frac{2.135}{\lambda},
$$

$$
0.41 \leq \lambda \leq 0.66\,\mu\text{m}. \tag{2.7}
$$

$$
\begin{aligned}
k_{\mathrm{Q}}(\lambda) \;&=\; 4.182 - \frac{3.083}{\lambda} + \frac{1.290}{\lambda^2}, \\[4pt]
&\quad 0.41 \leq \lambda \leq 0.66 \, \mu\mathrm{m}; \\[4pt]
&=\; -0.762 + \frac{2.135}{\lambda}, \\[4pt]
&\quad \lambda > 0.66 \, \mu\mathrm{m}.
\end{aligned}
\tag{2.8}
$$

The total to selective absorption ratio is $R_{\mathrm{V}} = 3.12$ and 2.84 for the linear and quadratic forms, respectively. There are two sources of systematic uncertainty in R_{V}. One is associated with the functional form used to fit the nebular attenuation curve. This error can be estimated by the difference in the values of R_{V} obtained for k_{Q} and k_{L} as $\Delta R \simeq 0.28$. The other systematic error in R_{V} originates from utilizing different normalization methods, for example, using another value of the wavelength (rather than $2.8\,\mu\mathrm{m}$) to set the nebular attenuation curve to zero (Reddy et al. 2020). This error is $\delta R \simeq 0.05$ if we set the zero-point to $3\,\mu\mathrm{m}$ instead. Overall, our result here is consistent within the uncertainty with the $R_{\mathrm{V}} = 3.1$ reported by Cardelli et al. (1989b) for the average MW curve, $R_{\mathrm{V}} = 2.9$ and 2.74 reported by Pei (1992) and Gordon et al. (2003a) for the SMC curve. Our results are also consistent with the R_{V} values reported for the two linear-in-$1/\lambda$ and quadratic-in-$1/\lambda$ attenuation curves derived in R20 ($R_{\mathrm{V}} = 3.34$ and 3.09, respectively).

Table 2.3: Properties of subsamples, Reddenings, R_{V}

Property [a]	Subsample	Bin Range [b]	Median [c]
$\log(M_*/M_\odot)$	M1	6.68 , 8.94	8.71
	M2	8.94 , 9.23	9.10
	M3	9.23 , 9.48	9.36
	M4	9.48 , 9.75	9.61
	M5	9.75 , 11.46	9.92
$\log(sSFR/\mathrm{yr}^{-1})$	S1	-11.79 , -10.02	-10.15
	S2	-10.02 , -9.83	-9.92
	S3	-9.83 , -9.67	-9.75
	S4	-9.67 , -9.46	-9.58
	S5	-9.46 , -7.05	-9.29
$12 + \log(\mathrm{O/H})$	Z1	7.85 , 8.73	8.63
	Z2	8.73 , 8.87	8.82
	Z3	8.87 , 8.98	8.94
	Z4	8.98 , 9.06	9.01
	Z5	9.06 , 9.40	9.11

[a] First, second, and third five rows indicate bins in stellar mass, sSFR, and metallicity, respectively. Sample size is 15,668 galaxies in each bin.

[b] The range of the associated physical property in each bin.

[c] Median value of the associated physical property in each bin.

2.5 Nebular Attenuation Curve vs. Galaxy Properties

To examine whether the curve varies with galaxy properties, we subdivide our sample into five bins each of stellar mass, sSFR, and metallicity, with each containing $15,668$ galaxies. Composite spectra are constructed for each of the subsamples following the method outlined in Section 2.3.1, and we use the same methodology outlined in 2.4.2 to derive the nebular attenuation curve. Table 2.4 reports the physical properties of galaxies
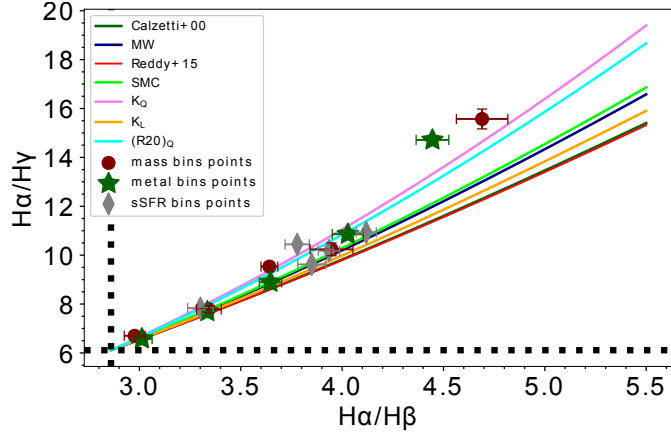
Figure 2.5: Ratios of $H\alpha/H\gamma$ vs $H\alpha/H\beta$ for stellar mass, metallicity, and sSFR bins. The error bars are also indicated for each point. The dotted black lines indicate the intrinsic line ratios. The relationship between these line ratios for different extinction/attenuation curves are indicated by the curves.

in each of the subsamples, and the properties of the derived nebular attenuation curves for each of the bins.

Figure 2.5 shows $H\alpha/H\gamma$ versus $H\alpha/H\beta$ measured from the stellar mass, metallicity and sSFR bins. All the bins are consistent with k_Q curve within their 1σ uncertainties, except for the one bin with the highest metallicity that covers the k_Q curve within its 2σ uncertainty, which is reasonable enough that we cannot rule out k_Q curve for this bin. In comparison to k_L, k_Q is found to best match the line ratio measurements. This is not particularly surprising given the additional free parameter of the quadratic fit versus the linear fit. The higher-order polynomial functional form reflects the wavelength behavior exhibited by the other common extinction and attenuation curves (e.g., Cardelli et al.
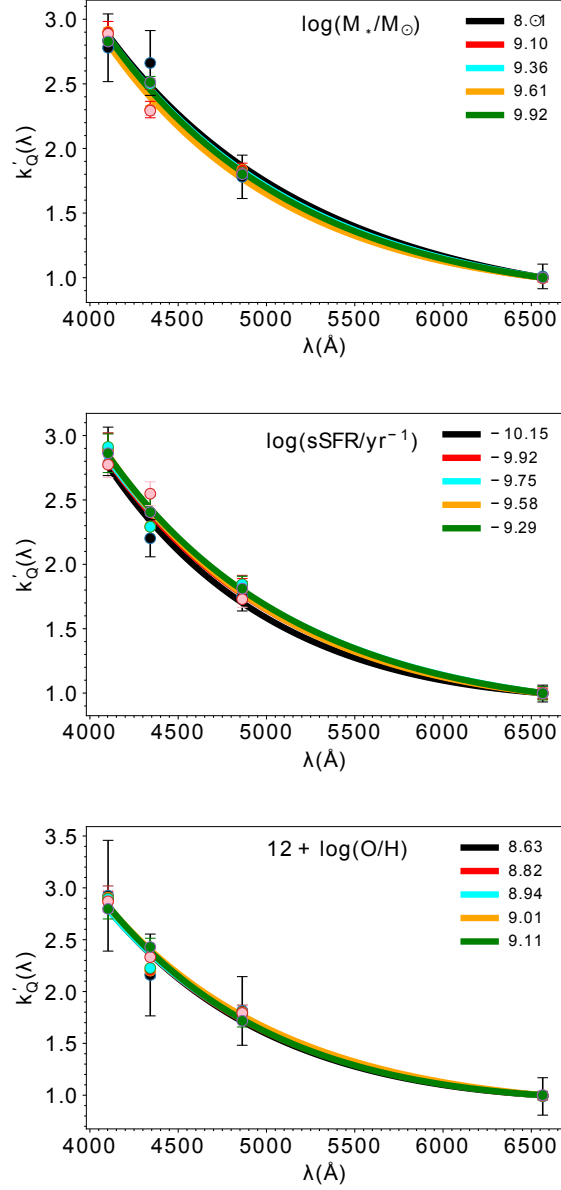
Figure 2.6:   Top, middle, and bottom panels indicate the curves derived for each bin of stellar mass, sSFR, and metallicity, respectively. The curves have been shifted so that their values at the wavelength of Hα are set equal to one. The attenuation curve points are shown by colored circles along with their error bars. The median values of the physical property in each of the bins are shown in the top right corner of each panel.

1989b; Calzetti et al. 2000a; Gordon et al. 2003a),[2] which is another reason why k_Q is preferred in this analysis.

The nebular attenuation curves (k'_Q) derived for the bins of stellar mass, metallicity, and sSFR are shown in Figure 2.6. The curves in each panel of Figure 2.6 are consistent with each others within their 1σ confidence interval, suggesting that the shape of the nebular attenuation curve shows little to no variations when binned by stellar mass, sSFR, and metallicity. The ratio of the total to selective absorption at V-band (R_V) are computed for each of the curve fits (Table 2.4). The R_V values for the curves in each associated physical property are consistent with each others within their 1σ systematic uncertainties. This implies that the normalization of the nebular attenuation curve does not vary with the aforementioned properties.

2.6 Discussion

Our results indicate that there is no significant variation in the shape of the nebular attenuation curve in the range of $0.41\,\mu$m to $0.66\,\mu$m with stellar mass, metallicity, and sSFR for low-redshift star-forming galaxies. This lack of variation may be related to the fact that the nebular attenuation curve is only probing those sightlines towards massive stars, where in a simplified scenario, the dust configuration can be approximated as a foreground screen and the dust size distribution is dictated by the radiation field of the youngest stellar populations. Because of the latter, one might not expect much variation in the shape of the curve as a function of globally-derived properties that are not solely sensitive to the

---

[2]For the longer-wavelength ($\lambda > 7000$ Å) their shape is typically characterized by an inverse power-law in λ.

youngest stellar populations. Although, there still exists the possibility that identical curves in the optical regions can be attributed to dust distribution with different properties.

The overall combination of the dust geometry and composition dictates the shape of the nebular attenuation curve. In addition to that, the connection between the extinction and attenuation curves can be complicated. Therefore, it is difficult to identify any particular similarities in the dust properties of the various bins solely based on the fact that the attenuation curves have identical shapes.

2.7   Summary

We use $78,340$ spectra of local star-forming galaxies with the redshift range of $z \simeq 0.04 - 0.1$ to investigate whether the shape of the nebular attenuation curve varies with the inferred physical properties of the sample. We use the first four detected Balmer lines $(\mathrm{H}\alpha, \mathrm{H}\beta, \mathrm{H}\gamma, \mathrm{H}\delta)$ from the stacked spectrum of all the galaxies in the sample to derive an average nebular attenuation curve using linear and quadratic polynomial functional forms in terms of $1/\lambda$.

The curves derived in this work are consistent with the nebular attenuation curves presented in R20 for high-redshift galaxies within 1σ and the MW and SMC curves within 2σ confidence interval. The R_{V} values obtained for the curves derived in this work are consistent with the ones computed for the Galactic extinction and SMC curves, and the curves presented in R20, showing that the curves are also similar to that of the MW, SMC, and nebular curves derived in R20 in terms of the normalization.

We calculate the nebular attenuation curve for galaxies in bins of stellar mass, metallicity, and sSFR, and compare their shapes. The curves derived in these various bins are identical to each other within the uncertainties.

The analysis outlined here may be extended to also examine the nebular curve in galaxies hosting AGN, and to determine if the presence of the hard radiation field of AGN may influence dust grain size distributions and/or geometry.

2.8 Acknowledgement

tion Group, University of Tokyo, University of Utah, Vanderbilt University, University of Virginia, University of Washington, and Yale University.

Data Availability

The spectra of galaxies analyzed in this work are publicly available from the SDSS survey. We use the SDSS Data Release 8 (Aihara et al. 2011) for the purpose of this work. We get the spectra of galaxies in our sample by submitting a query in `https://skyserver.sdss.org/casjobs/`. The SDSS catalogs (*Galspec*) containing the basic information and line measurements for each spectrum are provided by MPA/JHU group (Kauffmann et al. 2003; Brinchmann et al. 2004; Tremonti et al. 2004a) and are available from: `http://www.sdss3.org/dr8/spectro/galspec.php`.

Table 2.4: Properties of subsamples, Reddenings, R_V

Property [a]	$E_\mathrm{L}(B-V)$[d]	$E_\mathrm{Q}(B-V)$[e]	$(R_\mathrm{V})_\mathrm{L}$[f]	$(R_\mathrm{V})_\mathrm{Q}$[g]
$\log(M_*/M_\odot)$	0.059 ± 0.004	0.064 ± 0.006	3.189 ± 0.263	2.931 ± 0.263
	0.179 ± 0.003	0.201 ± 0.005	3.117 ± 0.306	2.815 ± 0.306
	0.292 ± 0.003	0.323 ± 0.005	3.106 ± 0.274	2.837 ± 0.274
	0.381 ± 0.004	0.432 ± 0.007	3.040 ± 0.305	2.739 ± 0.305
	0.608 ± 0.007	0.672 ± 0.012	3.036 ± 0.269	2.772 ± 0.269
$\log(sSFR/\mathrm{yr}^{-1})$	0.452 ± 0.020	0.525 ± 0.034	2.948 ± 0.374	2.613 ± 0.374
	0.377 ± 0.011	0.428 ± 0.019	3.041 ± 0.305	2.740 ± 0.305
	0.338 ± 0.008	0.380 ± 0.014	3.062 ± 0.285	2.781 ± 0.285
	0.349 ± 0.007	0.341 ± 0.012	3.132 ± 0.327	2.809 ± 0.327
	0.179 ± 0.006	0.191 ± 0.010	3.145 ± 0.302	2.847 ± 0.302
$12 + \log(\mathrm{O/H})$	0.059 ± 0.007	0.068 ± 0.011	3.162 ± 0.372	2.793 ± 0.372
	0.180 ± 0.003	0.207 ± 0.004	3.089 ± 0.349	2.744 ± 0.349
	0.288 ± 0.008	0.331 ± 0.014	3.046 ± 0.332	2.718 ± 0.332
	0.413 ± 0.010	0.468 ± 0.017	3.038 ± 0.306	2.736 ± 0.306
	0.587 ± 0.013	0.668 ± 0.023	2.984 ± 0.331	2.657 ± 0.331

[a] Subsample's names

[b] Reddening computed from the linear form of $A'(\lambda)$ (Equation 2.3).

[c] Reddening computed from the quadratic form of $A'(\lambda)$ (Equation 2.3).

[d] Total to selective absorption ratio calculated using the linear form of the total nebular dust attenuation curve.

[e] Total to selective absorption ratio calculated using the quadratic form of the total nebular dust attenuation curve.

Chapter 3

Exploring the Correlation between Hα-to-UV Ratio and Burstiness for Typical Star-forming Galaxies at $z \sim 2$

Abstract The Hα-to-UV luminosity ratio ($L(\mathrm{H}\alpha)/L(\mathrm{UV})$) is often used to probe bursty star-formation histories (SFHs) of star-forming galaxies and it is important to validate its efficiency against other indicators. To address this issue, we present a statistical analysis of the resolved distribution of star-formation-rate surface density (Σ_{SFR}) as well as stellar age and their correlations with the globally measured $L(\mathrm{H}\alpha)/L(\mathrm{UV})$ for a sample of 310

---

star-forming galaxies in two redshift bins of $1.37 < z < 1.70$ and $2.09 < z < 2.61$ observed by the MOSFIRE Deep Evolution Field (MOSDEF) survey. We use the multi-waveband CANDELS/3D-HST imaging of MOSDEF galaxies to construct Σ_{SFR} and stellar age maps. We also analyze the composite rest-frame far-UV spectra of a subsample of MOSDEF targets obtained by the Keck Low Resolution Imager and Spectrometer (LRIS), which includes 124 star-forming galaxies (MOSDEF-LRIS) at redshifts $1.4 < z < 2.6$, to examine the average stellar population properties, and the strength of age-sensitive FUV spectral features in bins of $L(\mathrm{H}\alpha)/L(\mathrm{UV})$. Our results show no significant evidence that individual galaxies with higher $L(\mathrm{H}\alpha)/L(\mathrm{UV})$ are undergoing a burst of star formation based on the resolved distribution of Σ_{SFR} of individual star-forming galaxies. We segregate the sample into subsets with low and high $L(\mathrm{H}\alpha)/L(\mathrm{UV})$. The high -$L(\mathrm{H}\alpha)/L(\mathrm{UV})$ subset exhibits, on average, an age of $\log[\mathrm{Age/yr}] = 8.0$, compared to $\log[\mathrm{Age/yr}] = 8.4$ for the low-$L(\mathrm{H}\alpha)/L(\mathrm{UV})$ galaxies, though the difference in age is significant at only the 2σ level. Furthermore, we find no variation in the strengths of SiIV $\lambda\lambda 1393, 1402$ and CIV $\lambda\lambda 1548, 1550$ P-Cygni features from massive stars between the two subsamples, suggesting that the high-$L(\mathrm{H}\alpha)/L(\mathrm{UV})$ galaxies are not preferentially undergoing a burst compared to galaxies with lower $L(\mathrm{H}\alpha)/L(\mathrm{UV})$. On the other hand, we find that the high-$L(\mathrm{H}\alpha)/L(\mathrm{UV})$ galaxies exhibit, on average, more intense HeII $\lambda 1640$ emission, which may suggest the presence of a higher abundance of high-mass X-ray binaries.

3.1 Introduction

While most galaxies follow a tight sequence in star-formation rate (SFR) versus stellar mass (M_*), there are some that are significantly offset above this relation at any given redshift, suggestive of a recent burst of star formation (Schmidt 1959; Kennicutt 1989; Somerville & Primack 1999; Springel 2000; Springel et al. 2005; Noeske et al. 2007; Kereš et al. 2009; Knapen & James 2009; Dobbs & Pringle 2009; Genzel et al. 2010; Governato et al. 2010; **?**; Rodighiero et al. 2014; Hopkins et al. 2014; Shivaei et al. 2015; Hayward & Hopkins 2017; Fujimoto et al. 2019). For example, the apparent increase in scatter of the relationship between SFR and M_* at low stellar masses suggests that such galaxies are characterized by bursty star-formation histories (Noeske et al. 2007; Hopkins et al. 2014; Asquith et al. 2018; Dickey et al. 2021; Atek et al. 2022). In addition, simulations with resolved scaling comparable to the star forming clouds suggest that the burst amplitude and frequency increases with redshift (e.g., Feldmann et al. 2017; Sparre et al. 2017; Ma et al. 2018). Given that bursty SFHs are inferred to be the likely mode of galaxy growth for at least lower mass galaxies at high-redshift (e.g., Atek et al. 2022 found evidence of bursty SFHs for lower mass galaxies with $M_* < 10^9 \, M_\odot$ at $z \sim 1.1$), it is important to determine the effectiveness of commonly-used proxies for burstiness.

A key method that has been used to infer the burstiness of star-forming galaxies is to compare SFR indicators that are sensitive to star formation on different timescales. Two of the widely used SFR indicators are derived from the Hα nebular recombination line ($\lambda = 6564.60 \, \text{Å}$) and far-ultraviolet (FUV) continuum ($1300 \, \text{Å} < \lambda < 2000 \, \text{Å}$). The H$\alpha$ emission line originates from the recombination of the ionized gas around young massive

stars ($M_* \gtrsim 20\,M_\odot$) and traces SFR over a timescales of $\sim 10\,\mathrm{Myr}$ (Kennicutt & Evans 2012b). The UV continuum is sensitive to the same stars that are responsible for Hα, as well as lower-mass stars (B stars, and A stars at wavelengths redder than 1700 A) with lifetimes of $\sim 100\,\mathrm{Myr}$ and $M_* \gtrsim 3M_\odot$. As a result, when compared to the Hα emission line, the FUV continuum traces SFRs averaged over a longer timescale. Therefore, variations in the dust-corrected Hα-to-UV luminosity ratio ($L(\mathrm{H}\alpha)/L(\mathrm{UV})$) may reveal information about recent burst activity (Glazebrook et al. 1999; Iglesias-Páramo et al. 2004; Lee et al. 2009; Meurer et al. 2009; Hunter et al. 2010; Fumagalli et al. 2011; Lee et al. 2011; Weisz et al. 2012; da Silva et al. 2012, 2014; Domínguez et al. 2015; Emami et al. 2019; Caplar & Tacchella 2019; Faisst et al. 2019).

For a constant star-formation history (SFH), the Hα-to-UV luminosity ratio will reach to its equilibrium after a few tens of Myr (e.g., ?). However, variations in the inferred integrated Hα-to-UV ratio may result from a number of effects, including variations in the IMF (Leitherer & Heckman 1995; Elmegreen 2006; Pflamm-Altenburg et al. 2007; Meurer et al. 2009; Pflamm-Altenburg et al. 2009; Hoversten & Glazebrook 2008; Boselli et al. 2009; Mas-Ribas et al. 2016), nebular and stellar dust reddening (Kewley et al. 2002; Lee et al. 2009; Reddy et al. 2012; Reddy et al. 2015; Shivaei et al. 2015, 2018a; Theios et al. 2019), ionizing escape fraction (Steidel et al. 2001; Shapley et al. 2006; Siana et al. 2007), and binary stellar evolution (Eldridge 2012; Eldridge et al. 2017; Choi et al. 2017). In addition, comparing the mock HST and JWST galaxy catalogs with 3D-HST observations of $z \sim 1$ galaxies, Broussard et al. (2019) finds that the average Hα-to-UV ratio is not impacted significantly by variations in the high-mass slope of the IMF, and metallicity.

Similar studies also show that the average Hα-to-UV is not a good indicator of business but rather a probe of the average SFH or dust law uncertainties (Broussard et al. 2019, 2022). Given these possibilities, any interpretation about the burstiness of galaxies based on the variations in $L(\mathrm{H}\alpha)/L(\mathrm{UV})$ must be approached with caution.

The MOSFIRE Deep Evolution Field (MOSDEF) survey is ideally suited to examine the extent to which variations in $L(\mathrm{H}\alpha)/L(\mathrm{UV})$ trace burstiness. MOSDEF probes galaxies at $z \sim 2$, which marks a key epoch for galaxy growth when the cosmic star-formation density reaches its maximum (Madau et al. 1996; Hopkins & Beacom 2006; Madau & Dickinson 2014). Additionally, the deep Hubble Space Telescope (HST) imaging of the MOSDEF galaxies obtained by CANDELS (Grogin et al. 2011; Koekemoer et al. 2011) enables the construction of stellar population maps that can be used to assess burstiness on smaller (resolved) spatial scales (e.g., Wuyts et al. 2011, 2012; Hemmati et al. 2014; Jafariyazani et al. 2019; Fetherolf et al. 2020). Moreover, the availability of follow-up Keck/LRIS rest-FUV spectra of a subset of 259 MOSDEF galaxies (Topping et al. 2020; Reddy et al. 2022) allows us to investigate the relationship between the $L(\mathrm{H}\alpha)/L(\mathrm{UV})$ ratio and age-sensitive FUV spectral features.

The goal of this study is to determine whether the dust-corrected Hα-to-UV luminosity ratio is a reliable tracer of a bursty SFH at $z \sim 2$. We address this question by examining the correlations between the differences in properties of the stellar populations and the $L(\mathrm{H}\alpha)/L(\mathrm{UV})$ ratio. The structure of this paper is as follows. In Section 4.2, we introduce the samples used in this work, and outline the sample selection criteria and data reduction. In Section 3.3, we describe the method used for constructing the stellar

population maps, and the result of the morphology analysis. Our approach for construct-

ing rest-FUV composite spectra is described in Section 3.4. Our results on variations of

the average physical properties of galaxies, and the strength of age-sensitive FUV spectral

features in bins of $L(\mathrm{H}\alpha)/L(\mathrm{UV})$ are presented in Section 3.5. Finally, the conclusions are

summarized in Section 3.6. Wavelengths are in the vacuum frame. We adopt a flat cosmol-

ogy with $H_0 = 70\,\mathrm{km\,s^{-1}}$, $\Omega_\Lambda = 0.7$, and $\Omega_m = 0.3$. A Chabrier (2003) IMF is assumed

throughout this work.

3.2 Sample

3.2.1 Rest-Frame Optical MOSDEF Spectroscopy, CANDELS/3D-HST Imaging

The MOSDEF survey (Kriek et al. 2015) used the Keck/MOSFIRE spectrograph

(McLean et al. 2012) to obtain rest-frame optical spectra of ~ 1500 H-band-selected star-

forming galaxies and active galactic nuclei (AGNs). The five extragalactic legacy fields

(GOODS-S, GOODS-N, COSMOS, UDS, AEGIS) covered by the CANDELS survey (Gro-

gin et al. 2011; Koekemoer et al. 2011) were targeted. The targets were chosen to lie in three

redshift bins: $1.37 < z < 1.70$, $2.09 < z < 2.61$, and $2.95 < z < 3.80$ where the strong rest-

frame optical emission lines (OII$\lambda 3727, 3730$, Hβ, OIII$\lambda\lambda 4960, 5008$, H$\alpha$, NII$\lambda\lambda 6550, 6585$,

and SII$\lambda 6718, 6733$) are redshifted into the YJH, JHK, and HK transmission windows,

respectively. Further details of the survey and MOSFIRE spectroscopic data reduction are

provided in Kriek et al. (2015).
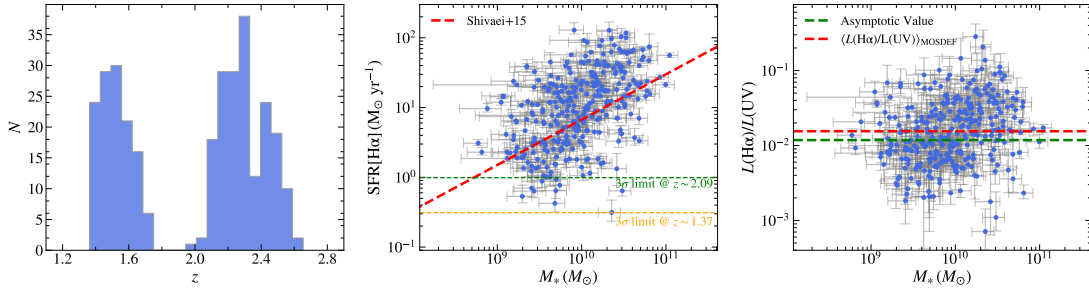
Figure 3.1: Physical properties of 310 star-forming galaxies in the MOSDEF/MORPH sample used in this work. *Left*: The histogram indicates the MOSDEF spectroscopic redshift distribution in two bins with the average redshifts of $z \sim 1.5$ and $z \sim 2.3$. *Middle*: SFR[Hα] vs. M_* relationship. SFR[Hα] is computed using the dust-corrected Hα luminosity. The conversion factor between the Hα luminosity and SFR[Hα], as well as stellar mass are derived using the SED modeling. The dashed red line shows Shivaei et al. (2015) relationship between SFR[Hα] and M_*, which has been adjusted to represent the assumptions used in this work, based on the first two years of MOSDEF (including galaxies with undetected Hβ). The horizontal dashed lines represent the 3σ detection limits of the SFR[Hα] determined for the two redshift bins ($1.37 < z < 1.70$, and $2.09 < z < 2.61$) using H and K band line sensitivities (Kriek et al. 2015). *Right*: The distribution of dust-corrected $L(H\alpha)/L(UV)$ with respect to the stellar mass where $L(H\alpha)$ and $L(UV)$ are dust-corrected using the Cardelli et al. (1989a) and SMC extinction curves, respectively. The red dashed line indicates the average dust-corrected $L(H\alpha)/L(UV)$ of all the galaxies in the MOSDEF parent sample that have coverage of Hα and Hβ emission lines with $S/N \geq 3$. The green dashed line indicates the asymptotic value of $L(H\alpha)/L(UV)$ for a constant SFH using BPASS SED models (Section 3.2.3).

We use the spectroscopic redshifts and emission lines measured by the MOSDEF survey. The spectroscopic redshift for each target was measured from the observed wavelength centroid of the highest signal-to-noise emission line in each spectrum. Emission line fluxes were measured from the 1D-spectra of the individual objects by fitting Gaussian functions along with a linear continuum. The Hα was fit simultaneously with the NII doublet using three Gaussian functions. The Hα emission line flux was corrected for the underlying Balmer absorption, which was measured from the best-fit stellar population model (Section 3.2.3). Line flux uncertainties were calculated by perturbing the observed spectra according to their error spectra and remeasuring the line fluxes 1000 times. The 68th percentile of the distribution obtained from these iterations was adopted to represent the upper and lower flux uncertainties (e.g., Reddy et al. 2015; Freeman et al. 2017).

Resolved broad-band photometry of the MOSDEF galaxies was obtained by CANDELS using HST/ACS in the $F435W$ (B_{435}), $F606W$ (V_{606}), $F775W$ (i_{775}), $F813W$ (I_{814}), and $F850LP$ (z_{850}) filters and HST/WFC3 in the $F125W$ (J_{125}), $F140W$ (JH_{140}), and $F160W$ (H_{160}) filters. CANDELS imaging covered $\sim 960\,\mathrm{arcmin}^2$ up to a 90% completeness in the H_{160} filter at a magnitude of $25\,\mathrm{mag}$. To construct stellar population maps for the sample galaxies, we use the processed CANDELS images provided by the 3D-HST grism survey team (Momcheva et al. 2016; Skelton et al. 2014; Brammer et al. 2012) along with the publicly available[1] photometric catalogs with coverage from $0.3\,\mu\mathrm{m}$ to $0.8\,\mu\mathrm{m}$. The HST images provided by the 3D/HST team were drizzled to a $0.06\,\mathrm{arcsec\ pixel}^{-1}$ scale and smoothed to produce the same spatial resolution as the H_{160} images ($0.18\,\mathrm{arcsec}$).

---

[1] https://archive.stsci.edu/prepds/3d-hst/

The final sample used in this work contains 310 typical star-forming galaxies at $1.36 < z < 2.66$, all meeting the following criteria. They all have spectroscopic redshifts from the MOSDEF survey and detections of Hα and Hβ emission lines with $S/N \geq 3$. AGNs were identified and excluded from the sample based on the IR properties, X-ray luminosities, or NIIλ6584/Hα line ratio criteria as described in Coil et al. (2015), Azadi et al. (2017, 2018), and Leung et al. (2019). Additional S/N and resolution constraints were applied to the HST photometry as a result of our approach of grouping pixels which will be discussed in Section 3.3.

The final sample described above is used to analyze the morphological information of the MOSDEF galaxies in the first part of this work (i.e., Section 3.3), and is referred to as the MOSDEF/MORPH sample throughout this work. This sample is based on that used by Fetherolf et al. (2022, submitted). The MOSDEF/MORPH sample covers a range of stellar mass of $8.77 < \log[M_*/M_\odot] < 11.04$, and a SFR[H$\alpha$] range of $0.40 < (\mathrm{SFR[H\alpha]}/M_\odot\mathrm{yr}^{-1}) < 130$. As shown in the middle panel of Figure 3.1, the MOSDEF/MORPH sample galaxies lie systematically above the mean main-sequence relation found by Shivaei et al. (2015) based on the first two years of MOSDEF. This is due to the S/N and resolution criteria (Section 3.3) imposed on the HST photometry of MOSDEF galaxies. Using these requirements results in a sample that is biased against low-mass and compact galaxies (Fetherolf et al. 2020). The S/N requirement for Hβ emission line is necessary to obtain a more reliable Balmer decrement measurement for each galaxy and does not introduce a significant bias in the sample (Shivaei et al. 2015; Reddy et al. 2015; Sanders et al. 2018; Fetherolf et al. 2021). As evidenced in the middle panel of Figure 3.1, our sample

galaxies do not display any substantial bias against the mean relation determined by Shiv-aei et al. (2015), which was derived irrespective of Hβ detection. The MOSDEF/MORPH sample galaxies exhibit a similar range of $L(\mathrm{H}\alpha)/L(\mathrm{UV})$ to the MOSDEF parent sample galaxies that have coverage of Hα and Hβ with significant detections ($S/N \geq 3$) and include galaxies with $L(\mathrm{H}\alpha)/L(\mathrm{UV})$ that lie at least 5σ below the mean ratio for the MOSDEF parent sample. The S/N requirement for Hβ emission does not significantly impact the average $L(\mathrm{H}\alpha)/L(\mathrm{UV})$ ratio. If we consider those galaxies where Hβ is not detected at the $S/N \geq 3$ but still covered by the observation, the average $L(\mathrm{H}\alpha)/L(\mathrm{UV})$ decreases by approximately 31%, which falls within the measurement uncertainty when considering the $S/N \geq 3$ requirement. Regardless of the Hβ detection requirement, the average $L(\mathrm{H}\alpha)/L(\mathrm{UV})$ values and the asymptotic $L(\mathrm{H}\alpha)/L(\mathrm{UV})$ are consistent within the measurement uncertainties. As mentioned earlier in this section, $L(\mathrm{H}\alpha)$ used here is obtained by the MOSDEF survey, and is corrected for the effect of dust using a MW extinction curve (Cardelli et al. 1989a) which is shown to best represent the nebular attenuation curve for both high-redshift and local galaxies (Reddy et al. 2020; Rezaee et al. 2021). UV luminosity ($L(\mathrm{UV})$) is estimated from the best-fit SED model (Section 3.2.3) at $\lambda = 1500\,\text{Å}$. We correct $L(\mathrm{UV})$ for dust using the SMC extinction curve (Fitzpatrick & Massa 1990a; Gordon et al. 2003b) and SED-based continuum reddening ($E(B - V)_{\mathrm{cont}}$).

3.2.2 MOSDEF/LRIS Rest-FUV Spectroscopy

A subset of 259 objects from the MOSDEF parent sample were selected for deep rest-FUV spectroscopic follow-up observations with the Keck I/Low Resolution Imager and Spectrometer (LRIS; Oke et al. 1995; Steidel et al. 2004). We refer the reader to Topping

et al. (2020) and Reddy et al. (2022) for further details about the MOSDEF/LRIS survey data collection and reduction procedures. In brief, targets were prioritized based on $S/N \geq 3$ detection of the four emission lines ([OIII], Hβ, [NII]λ6584, and Hα) measured by the MOSDEF survey. Objects with available Hα, Hβ, and [OIII] as well as an upper limit on [NII] were accorded the next highest priority. The objects with available spectroscopic redshifts from the MOSDEF survey, as well as those without a secure redshift measurements, were also included. The lowest priority was assigned to the objects that were not included in the MOSDEF survey, but had photometric redshifts and apparent magnitudes from the 3D-HST catalogs that were within the MOSDEF survey redshift ranges.

Rest-FUV LRIS spectra were obtained within 9 multi-object slit masks with $1''.2$ slits in four extragalactic legacy fields: GOODS-S, GOODS-N, AEGIS, COSMOS. The d500 dichroic was used to split the incoming beam at $\simeq 5000\,\text{Å}$ were used to obtain the LRIS spectra. The blue and red-side channels of LRIS were observed with the 400 line/mm grism blazed at 4300 Å, and the 600 line/mm grating blazed at 5000 Å, respectively. This configuration yielded a continuous wavelength range from the atmospheric cutoff at $3100\,\text{Å}$ to $\sim 7650\,\text{Å}$ (the red wavelength cutoff depends on the location of the slit in the spectroscopic field of view) with a resolution of $R \sim 800$ on the blue side and $R \sim 1300$ on the red side. The final MOSDEF/LRIS sample used in the second part of this work (i.e., Section 3.5) includes 124 star-forming galaxies at $1.42 < z < 2.58$, all meeting the same S/N and redshift measurement requirements as those mentioned in Section 3.2.1.

3.2.3 SED Modeling

We use the Binary Population and Spectral Synthesis (BPASS) version 2.2.1 models[2] (Eldridge et al. 2017; Stanway & Eldridge 2018) to infer UV luminosity (L(UV)), stellar continuum reddening ($E(B-V)_{\mathrm{cont}}$), stellar ages, conversion factors between luminosities and SFRs, as well as stellar masses (M_*). The effect of binary stellar evolution is included in the BPASS SED models, which has been found to be an important assumption in modeling the spectra of high redshift galaxies (Steidel et al. 2016; Eldridge et al. 2017; Reddy et al. 2022). These models are characterized by three sets of parameters, stellar metallicity (Z_*) ranging from 10^{-5} to 0.040 in terms of mass fraction of metals where solar metallicity ($Z_\odot$) is equal to 0.0142 (Asplund et al. 2009), the upper-mass cutoff of the IMF ($M_{\mathrm{cutoff}} = \{100M_\odot, 300M_\odot\}$), and the choice of including binary stellar evolution. These parameters divide the models into four sets of model assumptions with various M_{cutoff} and whether or not the binary effects are included. Throughout, we refer to these model combinations as 100bin, 300bin, 100sin, and 300sin where the initial number indicate the M_{cutoff} of the IMF and bin (sin) indicates that the binary evolution is (or is not) included (Reddy et al. 2022).

Stellar population synthesis (SPS) models are constructed by adding the original instantaneous-burst BPASS models for ages ranging from 10^7-10^{10} yr while adopting a constat star-formation history[3]. The choice of constant SFH over instantaneous burst models

---

[2]https://bpass.auckland.ac.nz/

[3]According to Reddy et al. (2012), if the stellar ages are constrained to be older than the typical dynamical timescale, SED models with either constant or exponentially rising star formation histories (SFHs) are best at reproducing the star formation rate (SFR) of galaxies at $z \sim 2$. The study also found that assuming exponentially rising SFHs leads to stellar population age estimates that are on average 30% older than those obtained under the assumption of constant SFHs. Our sample of galaxies, assuming both exponentially rising and declining SFHs, exhibit SFRs that are typically within 0.03 dex of those obtained under constant SFHs, which is within the usual measurement uncertainties of SED-derived SFRs.

is based on the fact that the latter are better suited for the individual massive star clusters that are more age-sensitive than the entire high-redshift star-forming galaxies, which have dynamical times that are typically far greater than a few Myr (Shapley et al. 2001; Papovich et al. 2001; Reddy et al. 2012). The reddening of the stellar continuum is added to the models assuming the following attenuation curves: the SMC (Gordon et al. 2003a), Reddy et al. (2015), and Calzetti et al. (2000b), with stellar continuum reddening in range of $E(B - V)_{\rm cont} = 0.0 - 0.60$. Based on earlier studies, these curves are shown to best represent the shape of the dust attenuation curves for the majority of high-redshift galaxies (e.g., Reddy et al. 2018a; Fudamoto et al. 2020; Shivaei et al. 2020b).

When fitting the broadband photometry, the stellar metallicity is held fixed at $\langle Z_* \rangle = 0.001$ as this value was found to best fit the rest-FUV spectra of galaxies in the MOSDEF/LRIS sample (Topping et al. 2020; Reddy et al. 2022). The stellar population ages of the models are permitted to range between $\sim 10\,\rm Myr$ and the age of the universe at the redshift of each galaxy. Unless mentioned otherwise, the BPASS model with binary stellar evolution, an upper-mass cutoff of $100\,M_\odot$ (100bin), and the SMC extinction curve are adopted for this analysis. Previous studies (e.g., Reddy et al. 2022) have shown that using the SMC dust attenuation curve results in better agreement between Hα and SED derived SFRs. Assuming the $Z_* = 0.001$ 100bin BPASS SPS models in fitting the broadband photometry yields a conversion factor of $2.12 \times 10^{-42}\,M_\odot \rm yr^{-1} erg^{-1} s$ between the dust-corrected Hα luminosity and SFR[Hα]. The dust-corrected $L(\rm UV)$ is determined using the best-fit model at $\lambda = 1500\,\text{Å}$ and the best-fit stellar continuum reddening.

The best-fit SED model is chosen by fitting the aforementioned models to the broadband photometry. The parameters of the model with the lowest χ^2 relative to the photometry are considered to be the best-fit values. The errors in the parameters are calculated by fitting the models to many perturbed realizations of the photometry according to the photometric errors. The resulting standard deviations in the best-fit model values give the uncertainties in these values.

3.3   Morphology Analysis

In this section we present a methodology to construct resolved stellar population maps that may unveil galaxies undergoing bursts of star formation on smaller ($\sim$10 kpc) spatial scales. We also examine the correlation between the resolved stellar population properties and $L(\mathrm{H}\alpha)/L(\mathrm{UV})$.

3.3.1   Pixel Binning

Rather than studying the individual images pixel by pixel, we group pixels using the two-dimensional Voronoi binning technique introduced by Cappellari & Copin (2003) and further modified by Fetherolf et al. (2020). The point spread function of the CANDELS imaging is larger than the individual pixels (0$''$18), such that we apply a Voronoi binning technique to the imaging in order to avoid correlated noise between individual analyzed elements. In brief, each of the 3D-HST images (Section 3.2.1) is divided into sub-images 80 pixels on a side. We use the SExtractor (Bertin, E. & Arnouts, S. 1996) segmentation map to mask pixels in each sub-image that are not associated with the galaxy. The pixels are
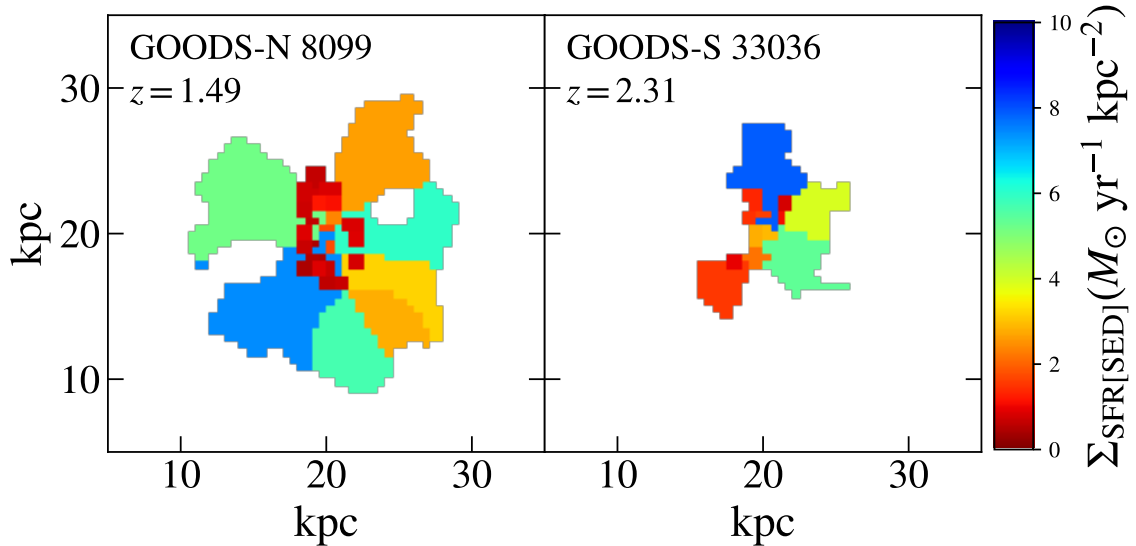
Figure 3.2: Examples of star-formation-rate surface density ($\Sigma_{\mathrm{SFR[SED]}}$) maps using Voronoi bins. The field name and 3D-HST Version 4.0 ID of each galaxy, as well as their redshifts, are indicated in the top left corner of each panel.

grouped following the algorithm presented in Cappellari & Copin (2003) to attain $S/N \geq 5$ in at least five different filters (e.g., see Fetherolf et al. 2020). Alongside CANDELS imaging, we use unresolved $Spitzer$/IRAC photometry to cover the rest-frame near-infrared part of the spectrum. As the HST and Spitzer/IRAC photometry have different spatial resolutions, we assign IRAC fluxes to each of the Voronoi bins proportionally according to the H_{160} flux (see Fetherolf et al. 2020 for further details). The stellar population properties for each Voronoi bin are inferred using the SED models (see Section 3.2.3) that best fit the resolved 3D-HST photometry. We calculate star-formation-rate surface density ($\Sigma_{\mathrm{SFR[SED]}}$) for each Voronoi bin by dividing the SFR determined from the best-fit resolved SED model by the area of each Voronoi bin. Figure 3.2 shows examples of the Voronoi bins and stellar population maps for two galaxies in the sample, one in each targeted redshift range.
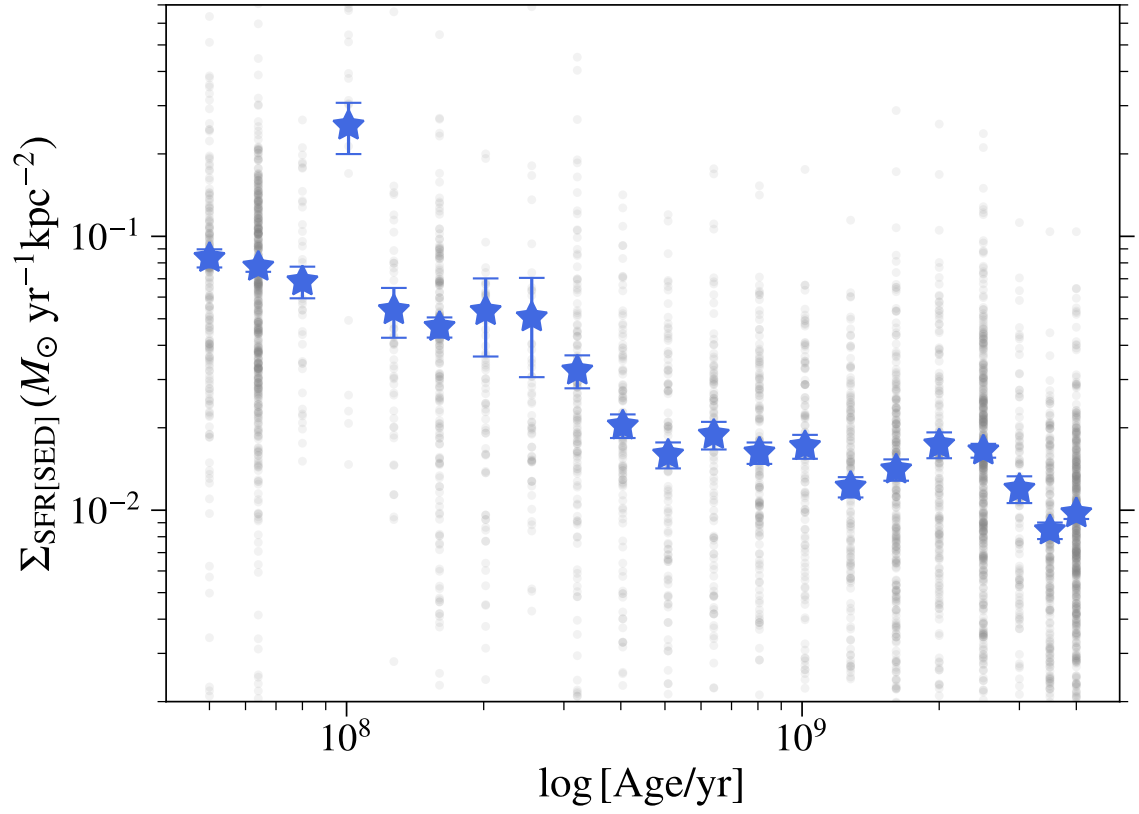
Figure 3.3: Star-formation-rate surface density vs. stellar age of Voronoi bins constructed for all the galaxies in the MOSDEF/MORPH sample (gray). Average values of $\Sigma_{\mathrm{SFR[SED]}}$ in bins of stellar age log[Age/yr] are shown by the blue stars.
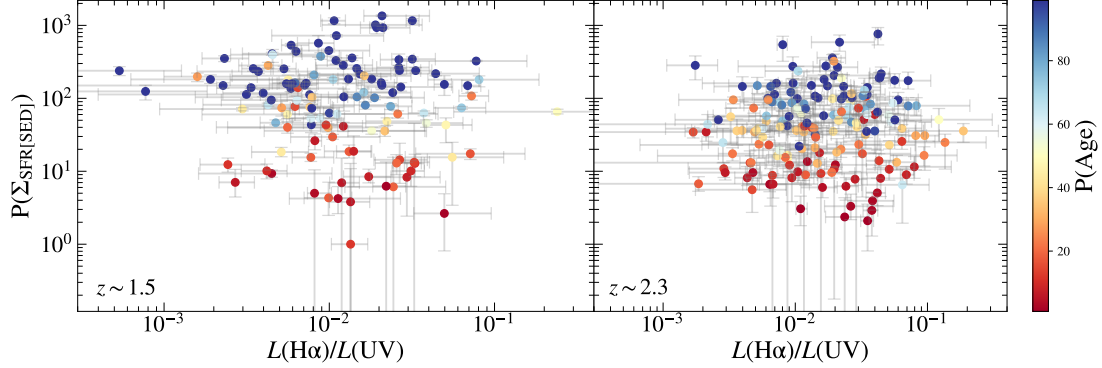
Figure 3.4: The MOSDEF/MORPH sample: $P(\Sigma_{\mathrm{SFR[SED]}})$ versus dust-corrected $L(\mathrm{H}\alpha)/L(\mathrm{UV})$ for two redshift bins centered at $z \sim 1.5$ (*left*) and $z \sim 2.3$ (*right*). The points are colored by patchiness of the stellar age. No significant correlations is found between $L(\mathrm{H}\alpha)/L(\mathrm{UV})$ and $P(\Sigma_{\mathrm{SFR[SED]}})$, or between $L(\mathrm{H}\alpha)/L(\mathrm{UV})$ and $P(\mathrm{Age})$. The Spearman correlation properties for the relations shown in this figure are reported in Table 3.1.

3.3.2 Patchiness

Patchiness (P) is a recently introduced morphology metric (Fetherolf et al. 2022) that evaluates the Gaussian likelihood that each of the distinct components of a distribution are equal to the weighted average of the distribution. In this analysis, individual elements are values of a parameter measured for each of the resolved Voronoi bins. The area-weighted average of the parameter X measured from individual Voronoi bins is defined by

$$\langle X \rangle = \frac{\sum_{i=1}^{N_{\mathrm{bins}}} n_{\mathrm{pix},i} X_i}{\sum_{i=1}^{N_{\mathrm{bins}}} n_{\mathrm{pix},i}}, \tag{3.1}$$

where X_i are the values measured for the parameter X inside each of the Voronoi bins with uncertainty σ_i, N_{bins} is the total number of Vornoi bins in a galaxy photometry, and n_{pix} is the total number of pixels inside a single Voronoi bin (area). The patchiness, $P(X)$, can be calculate by Equation 2 in Fetherolf et al. 2022 as:

$$P(X) = -\ln\left\{ \prod_{i=1}^{N_{bins}} \frac{1}{\sqrt{2\pi}\sigma_i} \exp\left[-\frac{(X_i - \langle X \rangle)^2}{2\sigma_i^2} \right] \right\}. \tag{3.2}$$

47

Table 3.1: Results of Spearman correlation tests between $L(\mathrm{H}\alpha)/L(\mathrm{UV})$ and $P(\mathrm{Age})$, as well as $L(\mathrm{H}\alpha)/L(\mathrm{UV})$ and $P(\Sigma_{\mathrm{SFR[SED]}})$.

Redshift bins		ρ_s[a]	P_n[b]
$z \sim 1.5$	$P(\mathrm{Age})$[c]	-0.04	0.62
	$P(\Sigma_{\mathrm{SFR[SED]}})$[d]	-0.09	0.30
$z \sim 2.3$	$P(\mathrm{Age})$	0.06	0.43
	$P(\Sigma_{\mathrm{SFR[SED]}})$	0.07	0.36

[a] The Spearman correlation coefficient between $L(\mathrm{H}\alpha)/L(\mathrm{UV})$ and each of the listed parameters using the MOSDEF/MORPH sample.

[b] The probability of null correlation between $L(\mathrm{H}\alpha)/L(\mathrm{UV})$ and each of the listed parameters using the MOSDEF/MORPH sample.

[c] Patchiness of the stellar population age.

[d] Patchiness of the star-formation-rate surface density.

A detailed discussion of the patchiness metric properties is presented in Fetherolf et al. 2022. In brief, patchiness can be compared most reliably between galaxies with similar redshifts. Thus, we divide galaxies into two bins of redshift and analyze the patchiness separately for galaxies in each bin. Moreover, patchiness can be used on parameters with large dynamic range or parameters with values close to zero. We study patchiness of $\Sigma_{\mathrm{SFR[SED]}}$ which traces the concentration of star formation within the Voronoi bins over a few Myr timescale, and exhibits a large dynamic range among our sample galaxies. A

physical example of how patchiness can be used is presented in Fetherolf et al. 2022, where higher patchiness values of stellar reddening indicate a more complex dust distribution.

A burst of star formation on top of an underlying constant SFH can result in an increase in Σ_{SFR}. An element of a resolved population containing a burst of star formation has a higher Σ_{SFR} and a younger stellar age compared to other elements, resulting in a larger $P(\Sigma_{\text{SFR[SED]}})$, and $P(\text{Age})$. Therefore, large $P(\Sigma_{\text{SFR[SED]}})$ may suggest the presence of bursts in localized (Voronoi) regions of galaxies. Figure 3.3 indicates the relationship between the stellar age and $\Sigma_{\text{SFR[SED]}}$ derived for Voronoi bins constructed for all the galaxies in the MOSDEF/MORPH sample. The figure indicates that younger stellar populations are found in regions with higher SFR surface densities. The relationship between SFR surface density and stellar age can be complex and influenced by various factors, such as the stellar mass, morphology, and environment. At $z \sim 2$, the Universe was experiencing a peak in star formation activity (Hopkins & Beacom 2006). This can be attributed to several factors, including the higher gas content in galaxies, which led to more efficient star formation and higher SFR surface densities.

3.3.3 Patchiness of $\Sigma_{\textbf{SFR[SED]}}$ vs. $L(\textbf{H}\alpha)/L(\text{UV})$

This section presents our results on the correlation between $P(\Sigma_{\text{SFR[SED]}})$ and $L(\text{H}\alpha)/L(\text{UV})$. Given that star-formation mode varies in strength, duration, or a combination of both factors in different regions of a galaxy (Reddy et al. 2012; Dale et al. 2016, 2020; Smith et al. 2021), and patchiness is sensitive to outliers below and above the average, we expect $P(\Sigma_{\text{SFR[SED]}})$ to be large for galaxies that are undergoing a burst of star formation that could be detected on resolved scales.

Due to surface brightness dimming, higher-redshift objects on average have fewer and larger Voronoi bins. To control for this effect, we divide the MOSDEF sample into two subsmaples in the redshift ranges of $1.37 < z < 1.70$ ($z \sim 1.5$) and $2.09 < z < 2.61$ ($z \sim 2.3$). Figure 3.4 shows the relationship between $P(\Sigma_{\text{SFR[SED]}})$ and $L(\text{H}\alpha)/L(\text{UV})$ for galaxies in each redshift bin. Based on a Spearman correlation test, we find no significant correlation between the two for both the $z \sim 1.5$ and $z \sim 2.3$ subsamples, with probabilities of $P_{\text{n}} = 0.30$ and 0.36, respectively, of a null correlation. As shown by the stellar age color-coded points, a higher $P(\Sigma_{\text{SFR[SED]}})$ corresponds to a higher $P(\text{Age})$, which is expected given that stellar age and star-formation-rate surface density are correlated for a given SPS model. There is also a lack of correlation between $L(\text{H}\alpha)/L(\text{UV})$ and $P(\text{Age})$ with correlation properties reported in Table 3.1.

One possible cause for the absence of correlation is the large uncertainties in $L(\text{H}\alpha)/L(\text{UV})$ and $P(\Sigma_{\text{SFR[SED]}})$ and $P(\text{Age})$[4]. Using $L(\text{H}\alpha)/L(\text{UV})$ as a tracer of stochastic star formation may be complicated by uncertainties in dust corrections and aperture mismatches between the Ha and UV measurements (e.g., Brinchmann et al. 2004; Kewley et al. 2005; Salim et al. 2007; Richards et al. 2016; Green et al. 2017; Fetherolf et al. 2022). These issues are discussed in more detail below.

Although there is a consensus that the Cardelli et al. (1989a) curve is an adequate description for the dust reddening of nebular recombination lines such as Hα (Reddy et al.

---

[4]The SED parameters, such as SFR, stellar age, etc., are determined for individual Voronoi bins by performing SED fitting on resolved scales, as explained in Section 3.2.3. However, determining the uncertainty or noise in each SED parameter is a time-consuming process due to the large number of Voronoi bins and galaxies involved (?). To address this challenge, we chose 50 galaxies with stellar population parameters similar to the overall sample and perturbed the resolved photometric fluxes based on their respective errors. We conducted SED fitting on these perturbed values, and the standard deviation of the SED parameters from the models with the lowest chi-squared were treated as the 1σ uncertainty in the SED parameters.

2020; Rezaee et al. 2021), a variety of different stellar attenuation curves have been found for high redshift galaxies, depending on their physical properties. For example, several studies have found that more massive galaxies ($M_* > 10^{10.4}\,M_\odot$) tend to have a slope of the attenuation curve that is similar to the Calzetti et al. (2000b), while the SMC extinction curve has been shown to be applicable for less massive galaxies (Reddy et al. 2015; Du et al. 2018; Shivaei et al. 2020b). We obtain the same lack of correlation between $P(\Sigma_{\mathrm{SFR[SED]}})$ and $L(\mathrm{H}\alpha)/L(\mathrm{UV})$ when the Reddy et al. (2015) and the metallicity-dependent Shivaei et al. (2020b) curves are used to dust-correct $L(\mathrm{UV})$. We find that the degree by which the variation in the attenuation curves affects the $P(\Sigma_{\mathrm{SFR[SED]}})$ and $L(\mathrm{H}\alpha)/L(\mathrm{UV})$ correlation is insignificant as long as a fixed curve is assumed to dust-correct $L(\mathrm{UV})$. However, a correlation may still be washed out if the attenuation varies from galaxy to galaxy systematically as a function of $L(\mathrm{H}\alpha)/L(\mathrm{UV})$ ratio.

Another factor that might cause the Hα-to-UV luminosity ratios of high redshift galaxies to deviate from their true values is aperture mismatch. $L(\mathrm{UV})$ is measured using broadband photometry, while Hα luminosity is measured using slit spectroscopy. However, Fetherolf et al. (2021) conducted an aperture-matched analysis utilizing a MOSDEF sample comparable to the one used in this study and found that the variations between Hα and UV SFRs are not caused by the aperture mismatches. Another possible reason for the absence of correlation is that the variations in SFH may be occurring in regions that are still spatially unresolved with the HST imaging (i.e., on scales smaller than a few kpc). Additionally, the lack of correlation could be expected if variations in the SFH are occurring on even shorter timescales than the typical dynamical timescale of the spatial region probed by a Voronoi

bin ($\sim 50\,\mathrm{Myr}$). In this case, such short and localized bursts of star formation may only affect the Hα-to-UV ratio on similar spatial scales.

3.4 Rest-FUV Composite Spectra Construction, And Model-Predicted $L(\mathbf{H}\alpha)/L(\mathrm{UV})$

Aside from patchiness, there are several key FUV spectral features that are age-sensitive and can potentially be used to probe bursty SFHs. In this section, we outline a stacking analysis methodology that allows us to measure the average strength of FUV features in bins of $L(\mathrm{H}\alpha)/L(\mathrm{UV})$.

3.4.1 Rest-FUV Composite Spectra Construction

Rest-FUV spectra are averaged together to produce high S/N composite spectra. Individual LRIS spectra have limited S/N to make measurements on the FUV spectral features. Using the stacked spectra, we measure the average physical properties of galaxies contributing to each composite, as well as measuring FUV spectral features associated with massive stellar populations. We use the procedures that are outlined in Reddy et al. (2016, 2022) to construct the composites. In brief, the science and error spectrum of sample galaxies are shifted to the rest-frame based on the MOSDEF spectroscopic redshift (Section 3.2.1), converted to luminosity density, and interpolated to a grid with wavelength steps $\Delta\lambda = 0.5\,\text{Å}$. The composite spectrum at each wavelength point is calculated as the average luminosity density after rejecting 3σ outliers. The error in the composite spectrum is calculated by perturbing the individual spectra according to their error, and using boot-

strap resampling to construct the stacked spectrum for those perturbed spectra 100 times. The standard deviation of the luminosity densities at each wavelength point gives the error in the composite spectrum.

3.4.2 Continuum Normalization

Rest-FUV composite spectra must be continuum-normalized in order to accurately measure the average strength of the FUV stellar features. We use the `SPS+Neb` models discussed in Reddy et al. (2022) to aid in the normalization process. `SPS+Neb` models consist of the `BPASS` SPS models described in Section 3.2.3 as the stellar component. Each `BPASS` SPS model is used as an input to the `Cloudy`[5] version 17.02 radiative transfer code (Ferland et al. 2017) to compute the nebular continuum. The final `SPS+Neb` models are then built by combining the stellar and nebular components. We refer the reader to Reddy et al. (2022) for more details. In brief, all the `BPASS` SPS models with a range of stellar ages of $\log[\mathrm{Age/yr}] = \{7.0, 7.3, 7.5, 7.6, 7.8, 8.0, 8.5, 9.0\}$ are interpolated to construct models with stellar metallicities comparable to the values expected for $z \sim 2$ galaxies (Steidel et al. 2016) rather than the original metallicity values of `BPASS` models described in Section 3.2.3. This results in a grid of models with stellar metallicities ranging from $Z_* = 10^{-4}$ to 3×10^{-3} spaced by 2×10^{-4}. Our assumptions for the ionization parameter (U) and gas-phase oxygen abundance (i.e., nebular metallicity; Z_{neb}) match the average values for the MOSDEF/LRIS sample where $\log[Z_{\mathrm{neb}}/Z_\odot] = -0.4$ and $\log U = -3.0$ (Topping et al. 2020; Reddy et al. 2022).

---

[5]https://gitlab.nublado.org/cloudy/cloudy/-/wikis/home

We fit the composite spectra with `SPS+Neb` models to model the continuum. The `SPS+Neb` models are normalized for a constant SFR of 1 $M_\odot$/yr. To re-normalize the models to the observed spectra, these models are forced to have the same median luminosity as the composites in the Steidel et al. (2016) Mask 1 wavelength windows. These wavelength windows are chosen to include regions of the spectrum that are not affected by interstellar absorption and emission features. We smooth the `SPS+Neb` models for wavelengths below 1500Å to have the same rest-frame resolution as the MOSDEF/LRIS spectra. To identify the best-fit `SPS+Neb` model for a composite spectrum, the χ^2 between the models and the composite are computed. The model that yields the smallest χ^2 is taken as the best-fit model. Using the median luminosity densities defined in the Rix et al. (2004) wavelength windows, a spline function is fitted to the best-fit model. Finally, the composite spectrum is divided by that spline function to produce a continuum-normalized spectrum.

Any line measurements derived from the continuum-normalized spectra are affected by uncertainties in the normalization of the composite spectra. In order to compute this uncertainty, the normalization process outlined above is applied to 100 realizations of the composite spectrum constructed by bootstrap resampling, and fitting the `SPS+Neb` models to those realizations. The standard deviation of the best-fit models gives the uncertainty in the continuum normalization at each wavelength point. In addition, all of the model parameters and their uncertainties, including stellar age, metallicity, continuum reddening, and SFR[SED] are derived using the mean and standard deviation of the best-fit values when fitting those realizations, respectively. Figure 3.5 shows an example of the comparison between the composite spectrum computed for all the galaxies in the MOS-
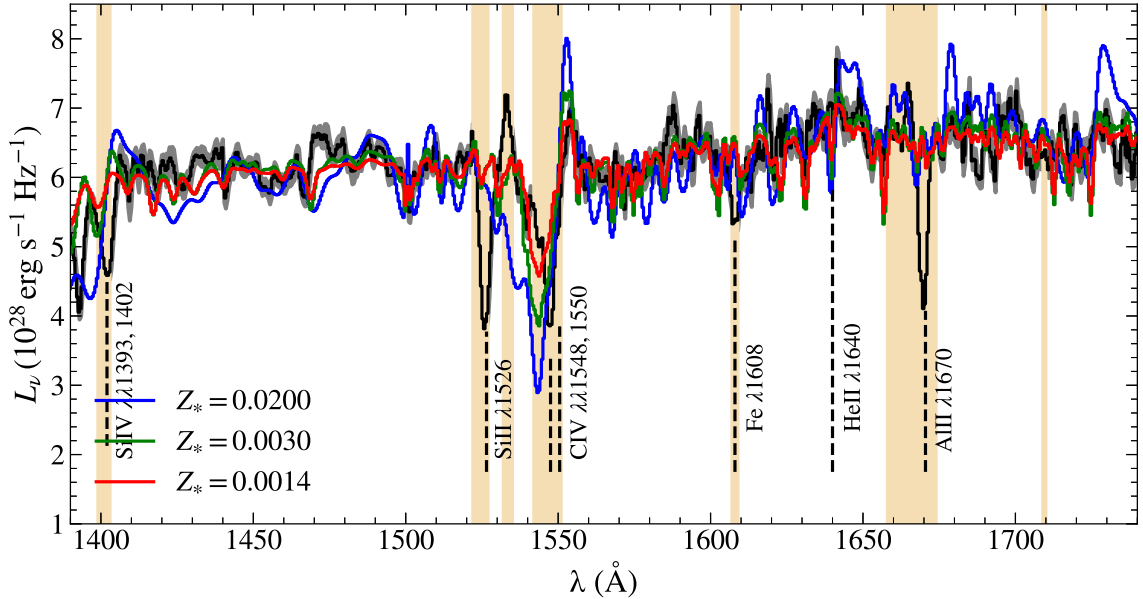
Figure 3.5: Composite spectrum constructed for the 124 galaxies in the MOSDEF/LRIS sample (black) with 1σ uncertainty (gray). The `SPS+Neb` models with fixed stellar age of $\log[\mathrm{Age/yr}] = 8.0$ and various stellar metallicities are shown alongside. Some of the prominent FUV spectral features are labeled. Regions that are not included in the fitting process are shaded in orange. The wavelengths that have been excluded are the ones that are impacted by interstellar absorption and emission features.

DEF/LRIS sample along with `SPS+Neb` models of different stellar metallicities. Models with lower metallicities are more consistent with the observed composite spectrum of $z \sim 2$ galaxies (Steidel et al. 2016; Reddy et al. 2022).

3.4.3 $L(\mathrm{H}\alpha)/L(\mathrm{UV})$ Predicted by the `SPS+Neb` Models versus Physical Properties and Model Assumptions

In this section, we examine how the Hα-to-UV ratio varies with stellar population properties, including stellar age, metallicity, inclusion of binaries, and M_{cutoff} of the
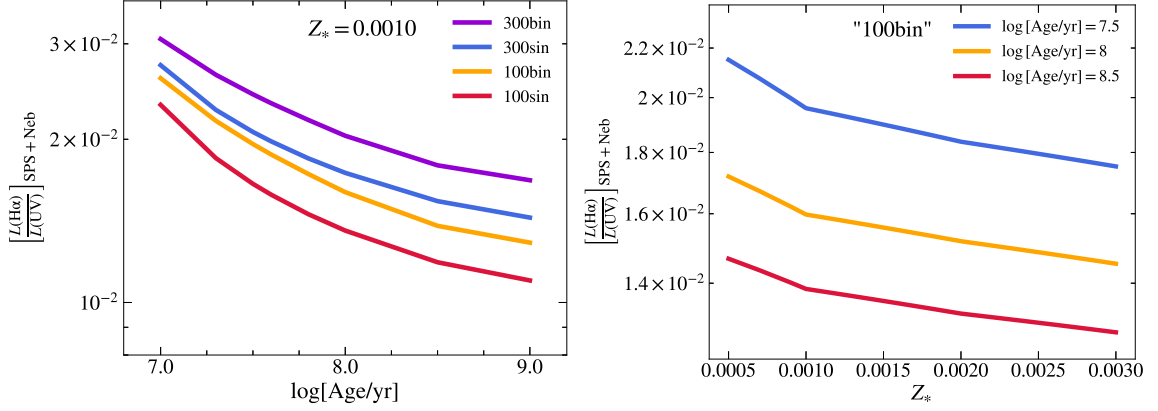
Figure 3.6: Variation of the Hα-to-UV luminosity ratio derived from the `SPS+Neb` models with physical properties including stellar age, stellar metallicity, inclusion of binary stellar evolution, and upper-mass cutoff of the IMF.

IMF using the `SPS+Neb` models. These relations are shown in Figure 3.6 and are used to study the systematic variation observed in $L(\mathrm{H}\alpha)/L(\mathrm{UV})$ of the MOSDEF/LRIS galaxies in Section 3.5. We calculate the Hα luminosity of each model using the relation:

$$L(\mathrm{H}\alpha)\,[\mathrm{erg\,s^{-1}}] = 1.37 \times 10^{-12}\, N(\mathrm{H}^0)\,[\mathrm{s^{-1}}] \tag{3.3}$$

where $N(H^0)$ is the hydrogen ionizing photon rate. We calculate $N(H^0)$ by integrating the model spectrum below 912Å. $L(\mathrm{UV})$ is calculated using the `SPS+Neb` model at $\lambda = 1500\,\text{Å}$.

The left panel of Figure 3.6 indicates that the ratio predicted by the constant SFH models ($[L(\mathrm{H}\alpha)/L(\mathrm{UV})]_{\texttt{SPS+Neb}}$) at a fixed stellar metallicity is influenced by both the choice of upper-mass cutoff of the IMF and inclusion of binary stellar evolution. The Hα luminosity increases by the presence of extremely massive stars with masses greater than $100 M_\odot$ and inclusion of energetic binary systems. For example, at $\log[\mathrm{Age/yr}] = 8.0$, the $L(\mathrm{H}\alpha)/L(\mathrm{UV})$ ratio grows by a factor of 1.2, and 1.3, respectively, from 100sin to the 100bin and 300bin models. The number of ionizing photons (and thus $L(\mathrm{H}\alpha)$) will decrease as massive O-stars

evolve off the main sequence, whereas less massive stars will still contribute significantly to the non-ionizing UV luminosity. As a result, the $L(\mathrm{H}\alpha)/L(\mathrm{UV})$ ratio decreases with increasing age as shown in the left panel of Figure 3.6.

The right panel of Figure 3.6 shows the sensitivity of $[L(\mathrm{H}\alpha)/L(\mathrm{UV})]_{\texttt{SPS+Neb}}$ of "100bin" model assumption to the stellar metallicity at various stellar population ages of the models. At a fixed stellar age, decreasing stellar metallicity increases the $\mathrm{H}\alpha$-to-UV luminosity ratio. For example, $[L(\mathrm{H}\alpha)/L(\mathrm{UV})]_{\texttt{SPS+Neb}}$ grows by a factor of ~ 1.1 from $Z_* = 0.0020$ to $Z_* = 0.0010$ models, at $\log[\mathrm{Age/yr}] = 8.0$. This relationship is expected given that lower-metallicity stellar atmospheres (less opaque) result in higher effective temperatures and therefore harder ionizing spectra (Bicker & Fritze-v. Alvensleben 2005).

3.5 Variations of the average Physical properties of galaxies with $L(\mathbf{H}\alpha)/L(\mathrm{UV})$

In addition to variations in the physical properties of galaxies such as stellar age and metallicity, variations in the strength of age-sensitive FUV spectral features with $L(\mathrm{H}\alpha)/L(\mathrm{UV})$ may contain important information on burstiness. To investigate the above-mentioned variations, we divide the MOSDEF/LRIS sample into two $L(\mathrm{H}\alpha)/L(\mathrm{UV})$ sub-samples (hereafter referring to as $low-$ and $high-L(\mathrm{H}\alpha)/L(\mathrm{UV})$ bin) with an equal number of galaxies in each. When binning the galaxies, we are using the $\mathrm{H}\alpha$-to-UV luminosity ratio rather than the SFR[$\mathrm{H}\alpha$]-to-SFR[UV] ratio because the latter requires some assumptions of the SFH to convert luminosity to SFR, and when trying to probe the SFH (i.e., whether a galaxy has a bursty or constant SFH), it is useful to use a probe which is independent of

such assumptions. The results of the measurements on the two subsamples are presented in the following sections.

3.5.1 Physical Properties of Galaxies vs. $L(\mathrm{H}\alpha)/L(\mathrm{UV})$

The bestfit `SPS+Neb` models to the rest-FUV composites are used to derive the average stellar age, metallicity, and continuum reddening of galaxies in each of the $L(\mathrm{H}\alpha)/L(\mathrm{UV})$ bins (Table 3.2). In order for the `SPS+Neb` models to self-consistently explain all the observations, we checked that the $L(\mathrm{H}\alpha)/L(\mathrm{UV})$ predicted by the best-fit `SPS+Neb` model to each composite is in agreement with the mean ratio of all individual galaxies contributing to the composite as well as the average ratio directly measured from the rest-FUV and optical composite spectra [6].

Table 3.2 reports the average physical properties of galaxies in each $L(\mathrm{H}\alpha)/L(\mathrm{UV})$ bin. The *high-*$L(\mathrm{H}\alpha)/L(\mathrm{UV})$ subset exhibits, on average, an stellar population age of $\log[\mathrm{Age/yr}] = 8.0$, compared to $\log[\mathrm{Age/yr}] = 8.4$ for the *low-*$L(\mathrm{H}\alpha)/L(\mathrm{UV})$ galaxies, though the difference in age is significant at only the 2σ level. The stellar population age of the *high-*$L(\mathrm{H}\alpha)/L(\mathrm{UV})$ galaxies is $100\,\mathrm{Myr}$, longer than the dynamical timescale of a few tens of Myr, implying that the *high-*$L(\mathrm{H}\alpha)/L(\mathrm{UV})$ galaxies are not necessarily undergoing a burst of star formation. Using the `SPS+Neb` models, $L(\mathrm{H}\alpha)/L(\mathrm{UV})$ increases by a factor of ~ 1.1 from $\log[\mathrm{Age/yr}] = 8.4$ to $\log[\mathrm{Age/yr}] = 8.0$ for a fixed stellar metallicity (Figure 3.6). The *high-*$L(\mathrm{H}\alpha)/L(\mathrm{UV})$ subset exhibits an average $L(\mathrm{H}\alpha)/L(\mathrm{UV})$ which is ~ 5 times larger than that of the *low-*$L(\mathrm{H}\alpha)/L(\mathrm{UV})$ subset. This implies that the difference

---

[6]The same procedure outlined in Section 3.4.1 is applied to construct the optical composite spectrum (e.g., Shivaei et al. 2018a; Reddy et al. 2020; Rezaee et al. 2021). The `Python` code presented in https://github.com/IreneShivaei/specline/ is used in constructing the optical composite spectra here.

in the average $L(\mathrm{H}\alpha)/L(\mathrm{UV})$ ratio of the subsets cannot be solely attributed to the variation in the stellar age of those subsets. It is essential to examine other burst indicators, such as the strength of the FUV P-Cygni features in both bins, to find whether there is any strong evidence that the $high\text{-}L(\mathrm{H}\alpha)/L(\mathrm{UV})$ subset traces recent starbursts. This is further discussed in the next section.

The effective radius (R_e) of each galaxy is taken from van der Wel et al. (2014), and is defined as the radius that contains half of the total $HST/F160W$ light. The star-formation-rate surface density ($\Sigma_{\mathrm{SFR}[\mathrm{H}\alpha]}$) of individual galaxies is then computed as:

$$\Sigma_{\mathrm{SFR}[\mathrm{H}\alpha]} = \frac{\mathrm{SFR}[\mathrm{H}\alpha]}{2\pi R_\mathrm{e}^2}. \tag{3.4}$$

For an ensemble of galaxies, $\langle\mathrm{SFR}[\mathrm{H}\alpha]\rangle$ is computed by multiplying the dust-corrected $\langle L(\mathrm{H}\alpha)\rangle$ measured from the optical composite spectrum by the conversion factor determined from the best-fit SPS+Neb model. $\langle\Sigma_{\mathrm{SFR}[\mathrm{H}\alpha]}\rangle$ is then computed using $\langle\mathrm{SFR}[\mathrm{H}\alpha]\rangle$ and mean R_e of individual galaxies in each ensemble. $\langle\mathrm{SFR}[\mathrm{H}\alpha]\rangle$ and $\langle\Sigma_{\mathrm{SFR}[\mathrm{H}\alpha]}\rangle$ increase significantly with increasing $\langle L(\mathrm{H}\alpha)/L(\mathrm{UV})\rangle$ between the two subsamples. While the instantaneous SFR (i.e., $\mathrm{SFR}[\mathrm{H}\alpha]$) differs significantly between the two subsamples, SFR[SED] that covers a timescale of $\sim 50\,\mathrm{Myr}$ does not change significantly within the measurement uncertainties. By design, galaxies with higher $L(\mathrm{H}\alpha)/L(\mathrm{UV})$ have on average higher Hα luminosities. However, this does not necessarily imply that these galaxies have higher Hα-based SFRs than UV-based SFRs. The conversion factor that relates the dust-corrected $L(\mathrm{H}\alpha)$ with SFR depends on stellar age, metallicity, and the hardness of the ionizing spectrum. As we show below, there is evidence that galaxies with higher $L(\mathrm{H}\alpha)/L(\mathrm{UV})$ have a harder

ionizing spectrum than those with lower $L(\mathrm{H}\alpha)/L(\mathrm{UV})$ and, as such, they are likely to have a higher Hα flux per unit SFR (see discussion in Section 3.5.2, and Section 3.6). The difference between the nebular and stellar reddening in the $high\text{-}L(\mathrm{H}\alpha)/L(\mathrm{UV})$ bin is $\simeq 2.1$ times larger when compared to the $low\text{-}L(\mathrm{H}\alpha)/L(\mathrm{UV})$. The higher nebular reddening measured for the $high\text{-}L(\mathrm{H}\alpha)/L(\mathrm{UV})$ bin is not surprising given that galaxies with larger $L(\mathrm{H}\alpha)$ (i.e., higher SFRs) tend to be dustier (Förster Schreiber et al. 2009b; Reddy et al. 2010; Kashino et al. 2013b; Reddy et al. 2015, 2020).

3.5.2   Photospheric and stellar wind FUV spectral features vs. $L(\mathbf{H}\alpha)/L(\mathrm{UV})$

Some FUV spectral features are strongly correlated with starburst age, metallicity, and IMF properties, making them excellent proxies for constraining the physical properties of the massive star population (Lamers et al. 1999; Pettini et al. 2000; Leitherer et al. 2001; Mehlert et al. 2002; Smith et al. 2002; Shapley et al. 2003; Keel et al. 2004; Rix et al. 2004; Steidel et al. 2004; Leitherer et al. 2010; Cassata et al. 2013; Gräfener & Vink 2015; Chisholm et al. 2019; Reddy et al. 2022).

In continuous star formation, stars form at a relatively constant rate over time. As a result, the galaxy maintains a steady population of young, massive stars. This leads to a relatively stable presence of FUV P-Cygni features. In contrast, bursty star formation involves periods of intense star formation activity followed by periods of relative quiescence. During a starburst episode, the galaxy produces a large number of massive stars in a short period, which can lead to stronger FUV P-Cygni features as a result of the increased population of massive stars. And, during a post-burst episode, the equivalent widths of the

Table 3.2: Average stellar population properties

Properties	$low\text{-}\frac{L(H\alpha)}{L(\mathrm{UV})}$	$high\text{-}\frac{L(H\alpha)}{L(\mathrm{UV})}$
$\langle L(\mathrm{H}\alpha)/L(\mathrm{UV})\rangle$[a]	0.007 ± 0.002	0.035 ± 0.005
$\langle z \rangle$[b]	2.132 ± 0.031	2.185 ± 0.029
$\langle \log[M_*/M_\odot] \rangle$[c]	9.88 ± 0.05	9.96 ± 0.06
$\langle R_\mathrm{e} \rangle \, (\mathrm{kpc})$[d]	2.94 ± 0.23	2.33 ± 0.14
$\langle 12 + \log(\mathrm{O/H}) \rangle$[e]	8.52 ± 0.02	8.39 ± 0.02
$\langle Z_*/Z_\odot \rangle$[f]	0.099 ± 0.010	0.085 ± 0.015
$\langle \log[\mathrm{Age/yr}] \rangle$[g]	8.4 ± 0.1	8.0 ± 0.2
$\langle E(B-V)_\mathrm{cont} \rangle$[h]	0.090 ± 0.010	0.074 ± 0.008
$\langle \mathrm{SFR[SED]} \rangle (\mathrm{M_\odot \, yr^{-1}})$[i]	9.61 ± 2.73	10.64 ± 3.35
$\langle \mathrm{SFR[H\alpha]} \rangle (\mathrm{M_\odot \, yr^{-1}})$[j]	8.57 ± 1.96	22.12 ± 2.04
$\langle \Sigma_\mathrm{SFR[H\alpha]} \rangle (\mathrm{M_\odot \, yr^{-1} kpc^{-2}})$[k]	0.16 ± 0.04	0.65 ± 0.10
$\langle E(B-V)_\mathrm{neb} \rangle$[l]	0.29 ± 0.03	0.49 ± 0.06
$\langle W_\lambda(\mathrm{SiIV}) \rangle \, (\mathrm{\AA})$[m]	0.103 ± 0.018	0.146 ± 0.015
$\langle W_\lambda(\mathrm{Civ}) \rangle \, (\mathrm{\AA})$[n]	0.206 ± 0.034	0.113 ± 0.024
$\langle W_\lambda(\mathrm{HeII}) \rangle \, (\mathrm{\AA})$[o]	0.428 ± 0.032	0.684 ± 0.033

[a] Mean dust-corrected Hα-to-UV luminosity ratio.
[b] Mean redshift.
[c] Mean stellar mass.
[d] Mean effective radius.
[e] Mean gas-phase abundances
[f] Stellar metallicity ($Z_\odot = 0.0142$ from Asplund et al. 2009).
[g] Stellar population age.
[h] Stellar continuum reddening.
[i] SED star-formation rate measured from the FUV composite spectrum.
[j] Hα star-formation rate measured from the optical composite spectrum.
[k] Hα star-formation-rate surface density.
[l] Nebular reddening measured from the optical composite spectrum.
[m] Equivalent width of SiIV $\lambda\lambda 1393, 1403$.
[n] Equivalent width of CIV $\lambda\lambda 1548, 1550$.
[0] Equivalent width of HeII $\lambda 1640$.

features are expected to weaken (Walborn et al. 1985; Pellerin et al. 2002; Leitherer 2005; Vidal-García et al. 2017; Calabrò et al. 2021). The FUV spectral features discussed in this work are the P-Cygni component of SiIV $\lambda\lambda 1393, 1402$, CIV $\lambda\lambda 1548, 1550$, and the stellar component of HeII$\lambda 1640$. The presence of CIV and SiIV P-Cygni features in a galaxy's spectrum suggests the existence of massive stars with $M_* \geqslant 30 M_\odot$ and short main-sequence lifetime of $\sim 2-5\,\mathrm{Myr}$, and therefore is an indicative of a very recent burst of star formation (Leitherer & Heckman 1995; Pettini et al. 2000; Leitherer et al. 2001; Shapley et al. 2003; Quider et al. 2009). The origin of the broad HeII$\lambda 1640$ stellar wind emission observed in the spectra of local galaxies is the massive short-lived and extremely hot Wolf-Rayet stars (Schaerer 1996; de Mello et al. 1998; Crowther 2007; Shirazi & Brinchmann 2012; Cassata et al. 2013; Visbal et al. 2015; Crowther et al. 2016; Nanayakkara et al. 2019). The fraction of WR stars declines with decreasing stellar metallicity. Therefore, another mechanism is needed to explain the observation of HeII$\lambda 1640$ at high redshift galaxies where the metallicity is lower compared to local galaxies. One possible explanation for such observation is the abundance of binary systems at high redshifts that can result in an increase in the fraction of WR stars in low metallicity environments (Shapley et al. 2003; Cantiello, M. et al. 2007; de Mink et al. 2013). In fact, according to previous studies, when single evolution stellar population synthesis models are compared to the models including binary evolution in low stellar metallicity, the HeII stellar feature is best reproduced by the latter (Shirazi & Brinchmann 2012; Steidel et al. 2016; Gutkin et al. 2016; Stanway et al. 2016; Senchyna et al. 2017; Eldridge et al. 2017; Smith et al. 2018; Chisholm et al. 2019; Saxena et al. 2020; Reddy et al. 2022). Therefore, fitting the observed rest-FUV composite spectra with the

SPS models that include binary stellar evolution is necessary in order to study the variations in the strength of stellar HeII $\lambda1640$ emission.

`SPS+Neb` Model Predictions of FUV Spectral Features

Based on the `SPS+Neb` models, we show an example of the sensitivity of SiIV, CIV, and HeII stellar features to the stellar age, metallicity, and M_{cutoff} of the IMF in Figure 3.7. The equivalent widths (W_λ) of these features are also shown in the inset panels. These equivalent widths are measured by directly integrating across each line (above the line of unity) in the continuum-normalized models. In each panel, we only adjust one physical parameter at a time and keep the other two unchanged. The fixed values are chosen based on the average parameters derived from the composite spectra of all galaxies in the MOSDEF/LRIS sample.

The top panel of Figure 3.7 compares three constant SFH models with fixed stellar population age of $\log[\mathrm{Age/yr}] = 8.0$, fixed upper-mass cutoff of $M_{\mathrm{cutoff}} = 100\,M_\odot$, and varying metallicities of $Z_* = \{0.0010, 0.0020, 0.0030\}$. As depicted by the inset panels, as the metallicity increases from $Z_* = 0.0010$ to $Z_* = 0.0030$, the equivalent widths of CIV and SiIV P-Cygni emission become ~ 2.3 and ~ 2.5 times larger, respectively. This is due to the fact that these P-Cygni features are extremely sensitive to mass-loss rate, which increases as metallicity increases. In the case of HeII, the model with lowest metallicity ($Z_* = 0.0010$) exhibits the largest equivalent width compare to the higher metallicity models. This is due to the fact that stars with lower metallicity at given ages have harder ionizing spectra.
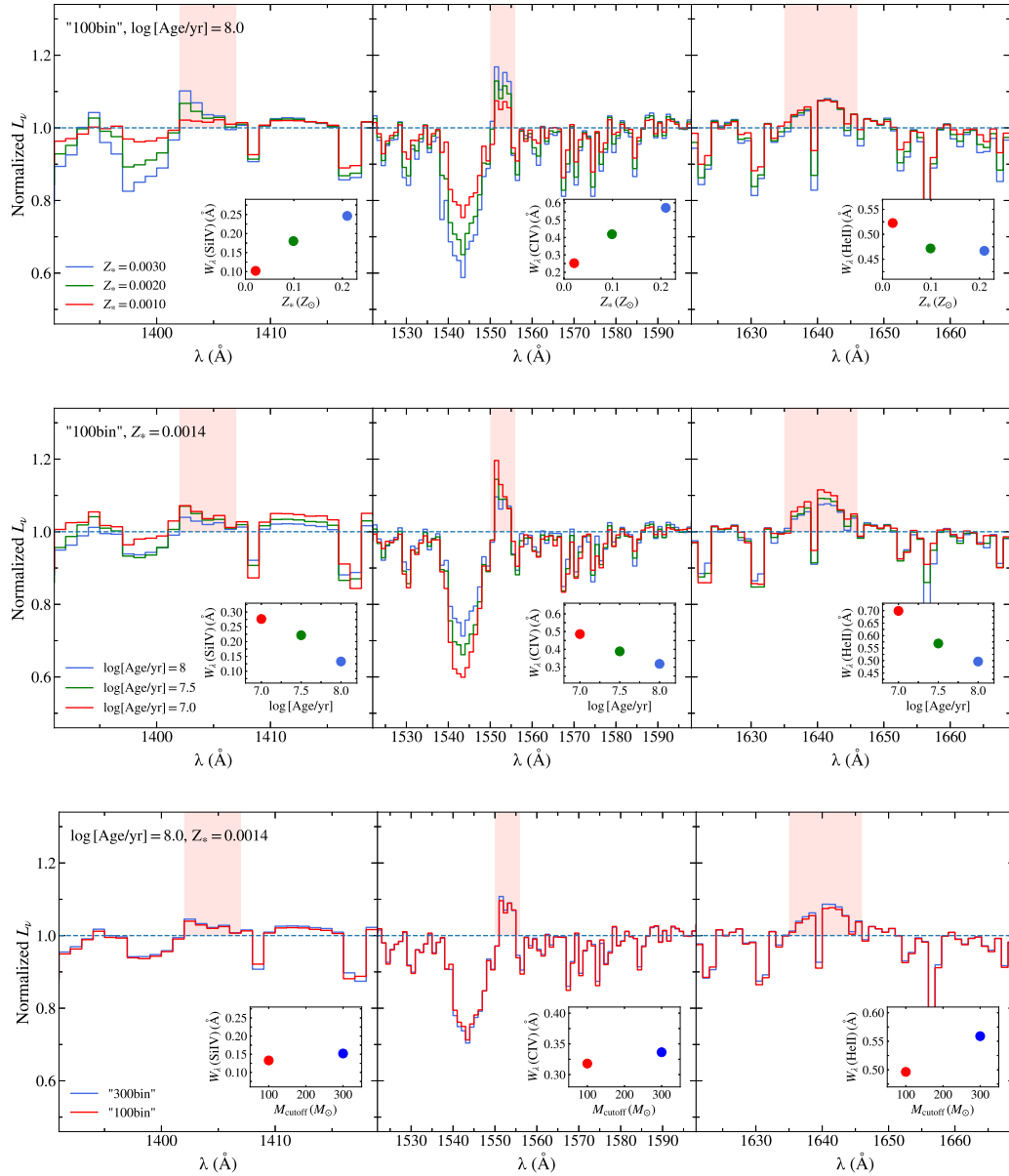
Figure 3.7: Variation of the continuum-normalized SPS+Neb models with stellar metallicity (*top*), stellar age (*middle*), and upper-mass cutoff of the IMF (*bottom*). In each panel only the specified parameter in the lower left is relaxed to change, while the parameters indicated in the upper left are held fixed. In all panels the ionization parameter and nebular metallicity are held fixed to the average values of the MOSDEF-LRIS sample ($\log U = -3.0$, $\log[Z_{\rm neb}/Z_\odot] = -0.4$; from Reddy et al. 2022). The inset panels indicate the equivalent width of each line in each model. The shaded pink indicates the regions by which the width measurements are performed for each feature.

The middle panel of Figure 3.7 shows three models with fixed metallicity of $Z_* = 0.0014$, fixed mass cutoff of $M_{\mathrm{cutoff}} = 100\,M_\odot$, and varying stellar ages of $\log[\mathrm{Age/yr}] = \{7.0, 7.5, 8.0\}$. The inset panels demonstrate that the younger stellar population model $(\log[\mathrm{Age/yr}] = 7.0)$ show a larger equivalent width of SiIV, CIV, and HeII by a factor of ~ 2.1, ~ 1.6, and ~ 1.5, respectively, when compared to the model with a higher age $(\log[\mathrm{Age/yr}] = 8.0)$. This prediction again demonstrates that the photospheric and stellar wind spectral features are strong at the early stages of star-formation.

The bottom panel of Figure 3.7 depicts two `SPS+Neb` models with fixed stellar age of $\log[\mathrm{Age/yr}] = 8.0$ and stellar metallicity of $Z_* = 0.0014$ and varying upper-mass cutoff of $M_{\mathrm{cutoff}}/M_\odot = \{100, 300\}$. The inset panels indicate that changing the mass cutoff of the IMF from $100\,M_\odot$ to $300\,M_\odot$ causes the equivalent widths of SiIV, CIV, and HeII to grow ~ 1.1, ~ 1.1, and ~ 1.2 times larger.

Observed FUV spectral features in bins of $L(\mathrm{H}\alpha)/L(\mathrm{UV})$

As shown in Section 3.5.2, the model-predicted equivalent widths of SiIV, CIV, and HeII are sensitive to stellar age, metallicity, and less sensitive to the high-mass cutoff of the IMF. In this section, we examine the variations in the observed equivalent widths of those FUV spectral features from the composite spectra of the two $L(\mathrm{H}\alpha)/L(\mathrm{UV})$ subsamples. The advantage of analyzing equivalent widths of the observed features is that they are unaffected by dust or aperture uncertainties. In addition, the observed equivalent widths are insensitive to the model assumptions (e.g., constant vs. instantaneous burst SFH).

The average rest-frame equivalent widths ($\langle W_\lambda \rangle$) for each of the above-mentioned FUV spectral features are measured by directly integrating across each line in each of

the continuum-normalized composite spectra shown in Figure 3.8 and are reported in Table 3.2. To ensure unbiased measurements, we utilize identical wavelength intervals for each bin. These wavelength intervals are derived based on the regions that the lines occupy in the `SPS+Neb` models. These regions are highlighted in Figure 3.7. The errors in W_λ are measured by perturbing the continuum-normalized spectra according to the error in spectra and repeating the measurements many times. The uncertainty is determined by the standard deviation of these perturbations. The final reported uncertainties include the error associated with the normalization process.

Figure 3.9 shows the comparison between the average rest-frame equivalent widths of SiIV, CIV, and HeII in the $L(\mathrm{H}\alpha)/L(\mathrm{UV})$ subsamples. No significant differences are found in $\langle W_\lambda(\mathrm{SiIV})\rangle$, and $\langle W_\lambda(\mathrm{CIV})\rangle$ between the *low-* and *high-*$L(\mathrm{H}\alpha)/L(\mathrm{UV})$ bins within the measurement uncertainties. However, $\langle W_\lambda(\mathrm{HeII})\rangle$ grows by a factor of ~ 1.7 from the *low-* to *high-*$L(\mathrm{H}\alpha)/L(\mathrm{UV})$ bin. If galaxies with higher $L(\mathrm{H}\alpha)/L(\mathrm{UV})$ are undergoing a burst of star formation, then we would expect them to have higher CIV and SiIV P-Cygni emission equivalent widths relative to galaxies with lower $L(\mathrm{H}\alpha)/L(\mathrm{UV})$.

While SiIV and CIV P-Cygni emissions are prominently stellar in origin, this is not the case for HeII. The extremely hot sources that produce stellar HeII emission also generate enough He^+ ionizing photons with wavelengths of $\lambda < 228\,\text{Å}$ to yield nebular HeII emission due to recombination, which complicates the interpretation of the HeII emission. Based on the previous studies (e.g., Steidel et al. 2016; Reddy et al. 2022), we adopt the following procedure to disentangle the stellar and nebular components. We measure the ob-
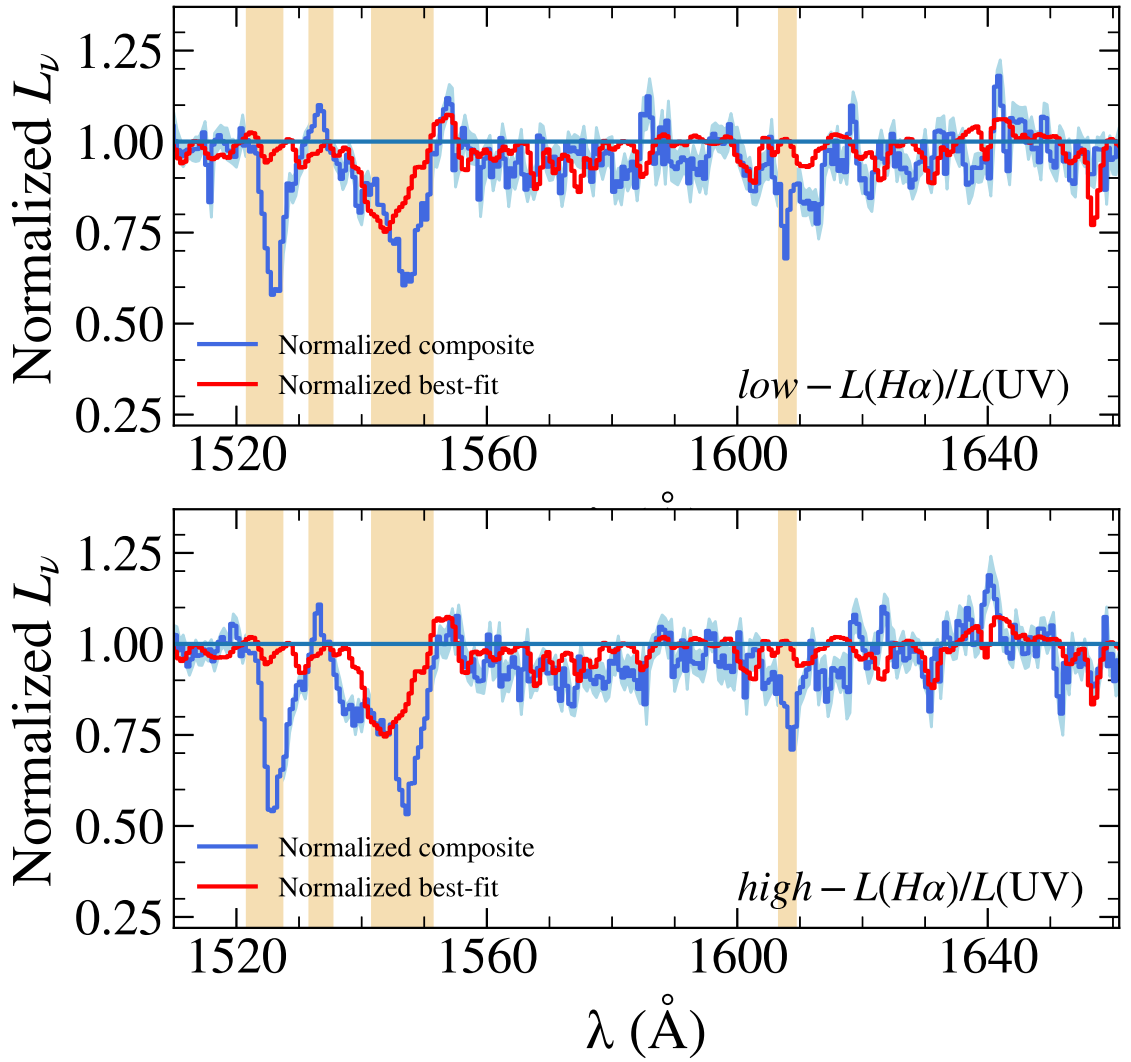
Figure 3.8: Continuum-normalized composite spectra (*blue*) of the two $L(\mathrm{H}\alpha)/L(\mathrm{UV})$ subsamples from which the equivalent width measurements are performed. The physical properties of each of the bins, as well as, $W_\lambda(\mathrm{SiIV})$, $W_\lambda(\mathrm{CIV})$, and $W_\lambda(\mathrm{HeII})$ measurements are listed in Table 3.2. Those regions that are not included in the fitting process are shaded in orange.
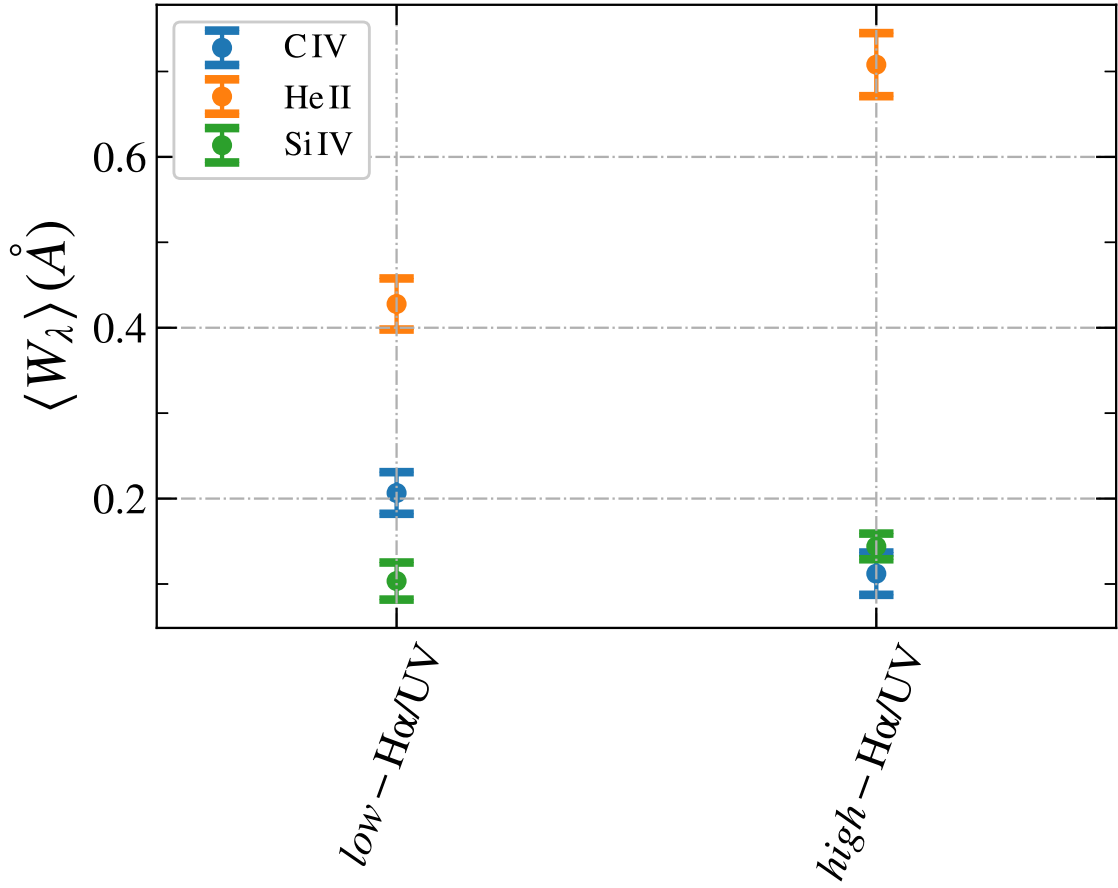
Figure 3.9: Comparison of the average equivalent widths of SiIV $\lambda\lambda1393, 1402$, CIV $\lambda\lambda1548, 1550$, and HeII$\lambda1640$ stellar emission lines measured from the continuum-normalized spectra of the two bins reported in Table 3.2.
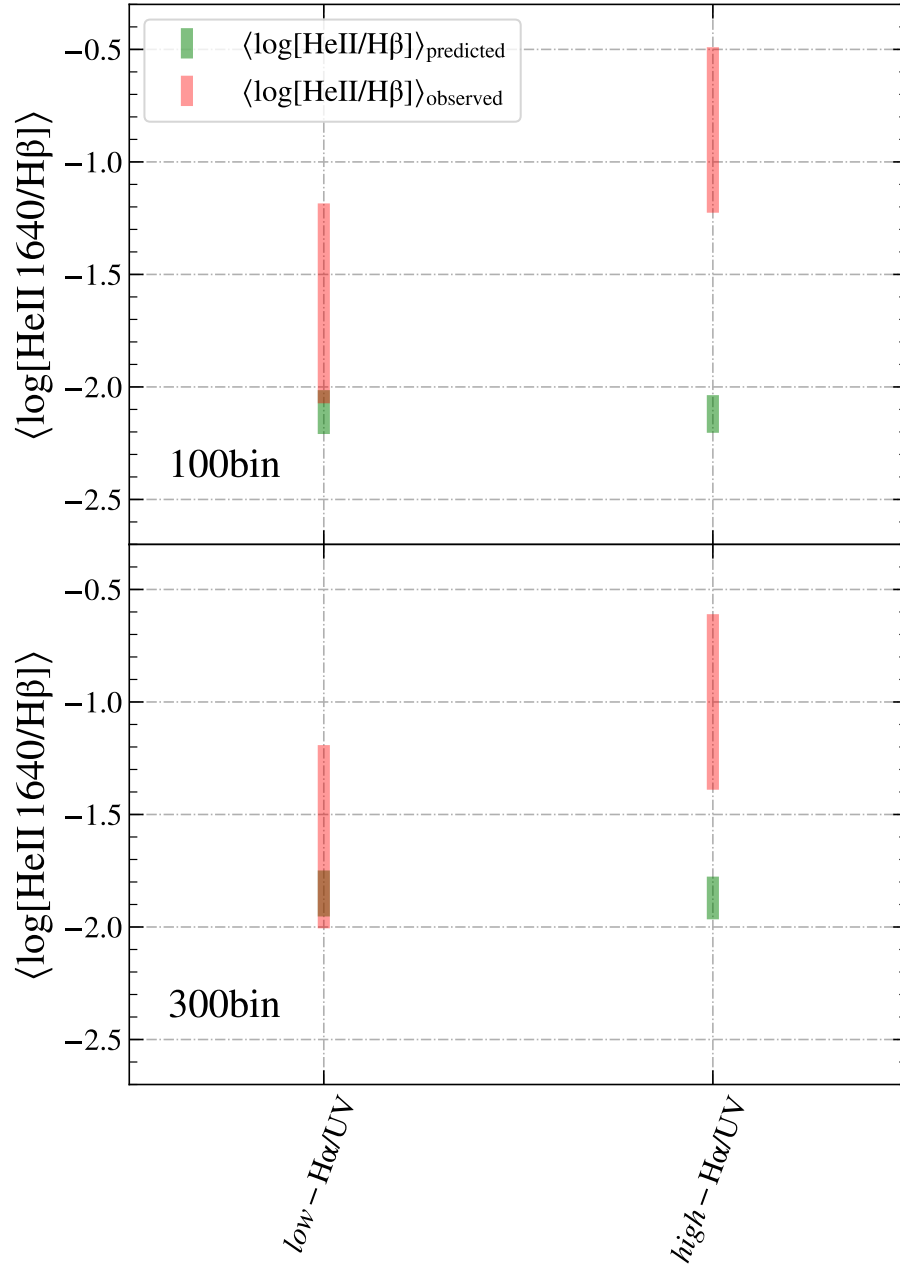
Figure 3.10: Comparison of the model-predicted nebular HeIIλ1640 relative intensity, $\langle$HeII/H$\beta\rangle$, derived from the `Cloudy` code and the observed dust-corrected relative intensity measured by subtraction of the best-fit `SPS+Neb` model from the composite spectrum for each $L(\text{H}\alpha)/L(\text{UV})$ subsample and different model assumptions. The colored bars show the $\pm 3\sigma$ range of the measurement uncertainties.

served nebular HeII intensity by subtracting the best-fit `SPS+Neb` model from the composite spectrum of each bin using the "100bin" and "300bin" [7] model assumptions. Because the best-fit model identifies the stellar component, the subtraction of the best-fit model from the observed spectrum is assumed to be purely nebular. The observed nebular HeII intensity is then dust-corrected assuming $\langle E(B-V)_{\mathrm{neb}} \rangle$ and the Cardelli et al. (1989a) extinction curve, where $\langle E(B-V)_{\mathrm{neb}} \rangle$ is measured directly from the optical composite spectrum. The model-predicted nebular HeII intensity is derived by using the best-fit `SPS` model of each bin as an input to the `Cloudy` photoionization code. The comparison between the model-predicted and observed nebular HeII emission in terms of relative intensity, $\langle \mathrm{HeII}/\mathrm{H}\beta \rangle$, is shown in Figure 3.10 for the $L(\mathrm{H}\alpha)/L(\mathrm{UV})$ subsamples. The model-predicted and observed nebular HeII intensities measured for the *low*-$L(\mathrm{H}\alpha)/L(\mathrm{UV})$ bin agree within the 3σ uncertainty for both of the mass cutoff assumptions. However, the model prediction of the nebular HeII intensity does not fully account for the observed nebular HeII intensity in the *high*-$L(\mathrm{H}\alpha)/L(\mathrm{UV})$ bin even with an increase in the upper-mass cutoff of the IMF.

Our results indicate that recent SF activity, and low metallicity cannot explain the difference in the HeII emission of galaxies in the two $L(\mathrm{H}\alpha)/L(\mathrm{UV})$ bins because the stellar age and metallicity derived for the two bins are similar within their respective uncertainties. Next, we investigate whether a top heavy IMF can account for such a difference. First, we separate the nebular and stellar components of the HeII emission. We then compare the observed nebular HeII intensity to that predicted by the `Cloudy` photoionization model

---

[7]When fitting the FUV composite spectra with the "300bin" `SPS+Neb` models, they can still reproduce all the FUV features discussed in this work. The best-fit stellar population age, metallicity, and continuum reddening of the *high*-$L(\mathrm{H}\alpha)/L(\mathrm{UV})$ subsample obtained with the "300bin" model are $\langle \log[\mathrm{Age/yr}] \rangle = 8.0 \pm 0.2$, $\langle Z_* \rangle = 0.084 \pm 0.011$, and $\langle E(B-V)_{\mathrm{cont}} \rangle = 0.067 \pm 0.005$.

using various assumptions on the upper-mass limit of the IMF. We find that even a top heavy IMF model ($M_{\text{cutoff}} = 300 M_\odot$) is unable to accurately predict the observed nebular HeII intensity of the $high\text{-}L(\text{H}\alpha)/L(\text{UV})$ bin. Another potential contributor that gives rise to the He$^+$ ionizing photons budget in low-metallicity star-forming galaxies is discussed below.

Schaerer et al. (2019) suggested that high mass X-ray binaries (HMXBs) are a primary source for producing He$^+$ ionizing photons in low-metallicity star-forming galaxies. They found that only SPS models that include HMXBs are able to reproduce the observed relative intensity of nebular HeII emission (HeII/Hβ). Studies of both the local and high-redshift universe have suggested that the X-ray luminosity (L_X) of HMXBs in star-forming galaxies increases with SFR (Nandra et al. 2002; Bauer et al. 2002; Seibert et al. 2002; Grimm et al. 2003; Reddy & Steidel 2004; Persic et al. 2004; Gilfanov et al. 2004; Persic & Rephaeli 2007; Lehmer et al. 2008, 2010), which is expected owing to the young ages of HXMBs ($\sim 10\,\text{Myr}$). Several studies have indicated that L_X per unit SFR in star-forming galaxies elevates at high redshift (e.g., Basu-Zych et al. 2013a; Lehmer et al. 2016; Aird et al. 2017). This enhancement in L_X/SFR with redshift may be due to the lower metallicities of high-redshift galaxies, which results in more luminous (and possibly more numerous) HMXBs (Brorby et al. 2016; Douna et al. 2015). In fact, observational studies have shown evidence of several ultraluminous X-ray sources in nearby galaxies with low metallicities (e.g., Mineo et al. 2012; Prestwich et al. 2013; Basu-Zych et al. 2013b). Following the idea that L_X/SFR is metallicity-dependent, Brorby et al. (2016) parameterized the L_X-SFR-Z

relationship, where Z is the gas-phase metallicity, for a sample of local star-forming galaxies as:

$$\log\left(\frac{L_\mathrm{X}/\mathrm{SFR}}{\mathrm{erg\,s^{-1}/(M_\odot\,yr^{-1})}}\right) = -0.59 \times (12 + \log(\mathrm{O/H}) - 8.69)$$
$$+39.49. \tag{3.5}$$

Fornasini et al. (2019) studied a sample of MOSDEF galaxies with available X-ray data to investigate the L_X/SFR and Z relationship at redshift $z \sim 2$. They found that for both $\mathrm{H}\alpha-$ and SED-based SFRs, the L_X-SFR-Z relation is in good agreement with that of the Brorby et al. (2016) relation for local galaxies (Equation 3.5). The results obtained were not affected by the assumed $L(\mathrm{H}\alpha)$ to SFR[Hα] conversion factor. We incorporate SFR[Hα] and SFR[SED] into Equation 3.5 to calculate the average X-ray luminosities for the $L(\mathrm{H}\alpha)/L(\mathrm{UV})$ subsets. We find that the average X-ray luminosity of the *high-$L(\mathrm{H}\alpha)/L(\mathrm{UV})$* subset is 3× greater with SFR[Hα], and 1.4× greater with SFR[SED] when compared to the average X-ray luminosity of the *low-$L(\mathrm{H}\alpha)/L(\mathrm{UV})$* subset. The statistical differences between the average X-ray luminosities derived using SFR[Hα] and SFR[SED] are at 5σ and 2σ levels, respectively. The increase in $\langle L_\mathrm{X} \rangle$ with increasing $L(\mathrm{H}\alpha)/L(\mathrm{UV})$ may indicate the presence of luminous HMXBs, which in turn could explain the high nebular HeII emission observed for galaxies with high $L(\mathrm{H}\alpha)/L(\mathrm{UV})$ ratios. Considering that an increase in $\langle L_\mathrm{X} \rangle$ is also observed when using SFR[SED], the conclusion about the existence of HMXBs may be reliably drawn. However, this conclusion is only robust at a 2σ statistical significance level owing to the large uncertainties of the average SED-based SFRs.

3.6 Summary and Conclusion

We examine the effectiveness of the dust-corrected globally measured Hα-to-UV luminosity ratio in tracing burstiness for typical star-forming galaxies at $z \sim 2$. We use the MOSDEF survey to explore stellar population properties differences in bins of $L(\mathrm{H}\alpha)/L(\mathrm{UV})$.

In the first part of this analysis, we employ the HST imaging of 310 star-forming galaxies (MOSDEF/MORPH sample) drawn from the MOSDEF survey to construct the star-formation-rate surface density and stellar age maps. We use a Voronoi binning technique to group the pixels based on their S/N. We then study the distribution of $\Sigma_{\mathrm{SFR[SED]}}$ and stellar age of Voronoi bins within each galaxy using a morphological metric called patchiness (P). Patchiness is sensitive to deviations from average, therefore galaxies that are undergoing a burst of star-formation contain regions with higher $\Sigma_{\mathrm{SFR[SED]}}$ and younger stellar age than the mean value for the entire galaxy and are expected to exhibit higher $P(\Sigma_{\mathrm{SFR[SED]}})$ and/or $P(\mathrm{Age})$. We find no correlation between $L(\mathrm{H}\alpha)/L(\mathrm{UV})$ and $P(\Sigma_{\mathrm{SFR[SED]}})$, as well as between $L(\mathrm{H}\alpha)/L(\mathrm{UV})$ and $P(\mathrm{Age})$. We suggest that the globally-averaged $L(\mathrm{H}\alpha)/L(\mathrm{UV})$ does not trace stochastic SFH over a time-scale of $\sim 10\,\mathrm{Myr}$, which is the typical dynamical timescale probed by the Voronoi bins. We suggest that this lack of correlation may be because of the uncertainties related to the variations in the stellar dust attenuation curve, limited dynamical time scale and spatial resolution probed by the Voronoi bins.

In the second part of this analysis, we use a rest-FUV spectroscopic sample obtained by LRIS (MOSDEF/LRIS sample) to study the average physical properties of $z \sim 2$

star-forming galaxies in bins of $L(\text{H}\alpha)/L(\text{UV})$. We use the `BPASS` constant SFH models combined with the nebular continuum emission generated by the `Cloudy` radiative transfer code (`SPS+Neb` models) as our theoretical basis to address the effect of different physical assumptions on the model-predicted $L(\text{H}\alpha)/L(\text{UV})$. As suggested by other studies, the Hα-to-UV ratio predicted by `SPS+Neb` models increases for younger stellar populations, or when the upper end of the IMF increases. Inclusion of binary stellar evolution or lowering the stellar metallicity of the models also cause a rise in the predicted ratio. We divide the 124 galaxies in the MOSDEF/LRIS sample into two bins of $L(\text{H}\alpha)/L(\text{UV})$ with an equal number of galaxies in each to investigate whether the variation observed in the dust-corrected Hα-to-UV ratio is related to differences in stellar age, metallicity, and/or upper end mass of the IMF as suggested by the SPS theoretical models. The main conclusions of the second part of the paper are as follows:

- The average stellar population age estimated for the *high*-$L(\text{H}\alpha)/L(\text{UV})$ bin is $\log[\text{Age/yr}] = 8.0 \pm 0.2$, compared to $\log[\text{Age/yr}] = 8.4 \pm 0.1$ for the *low*-$L(\text{H}\alpha)/L(\text{UV})$ bin. We find no significant variation in the stellar metallicity between the *low*- and *high*-$L(\text{H}\alpha)/L(\text{UV})$ bin within the measurement uncertainties. The stellar population age of $100\,\text{Myr}$ derived for the *high*-$L(\text{H}\alpha)/L(\text{UV})$ bin is longer than the dynamical timescale of a few tens of Myr, implying that the *high*-$L(\text{H}\alpha)/L(\text{UV})$ galaxies are not necessarily undergoing a burst of star formation.

- By design, galaxies with higher $L(\text{H}\alpha)/L(\text{UV})$ have on average higher Hα luminosities. Yet, this does not necessarily indicate that these galaxies possess higher SFR[Hα] than UV-based SFRs. The conversion factor that links the dust-corrected Hα lumi-

nosity with SFR is subject to variables such as stellar age, stellar metallicity, and the hardness of the ionizing spectrum. Upon studying the variations in the strength of the HeII $\lambda1640$ emission line, as discussed below, it appears that galaxies with a higher $L(\mathrm{H}\alpha)/L(\mathrm{UV})$ ratio tend to have a more intense ionizing spectrum compared to those with a lower ratio.

- We measure the observed equivalent widths of the SiIV $\lambda\lambda1393, 1402$, CIV $\lambda\lambda1548, 1550$, and HeII $\lambda1640$ emission lines for the two $L(\mathrm{H}\alpha)/L(\mathrm{UV})$ bins as these features are extremely sensitive to stellar population age, and metallicity. We find no significant variations between the EWs of the CIV and SiIV P-Cygni emissions observed in the composite spectra of the two $L(\mathrm{H}\alpha)/L(\mathrm{UV})$ bins. The EW of the HeII$\lambda1640$ emission grows significantly from the *low-* to *high-*$L(\mathrm{H}\alpha)/L(\mathrm{UV})$ bin. The lack of variations in the strength of the P-Cygni emissions between the two $L(\mathrm{H}\alpha)/L(\mathrm{UV})$ subsamples is expected given the insignificant differences found between the stellar age and metallicity of the two subsamples.

- The difference between the strength of the observed HeII emission of the *low-* and *high-*$L(\mathrm{H}\alpha)/L(\mathrm{UV})$ subsamples can be further investigated when the nebular and stellar components of the HeII line are disentangled. We find that the model-predicted nebular HeII intensity cannot accurately predict the observed amount for the *high-*$L(\mathrm{H}\alpha)/L(\mathrm{UV})$ bin even if the upper-mass limit of the IMF is increased from $M_{\mathrm{cutoff}} = 100\,M_\odot$ to $300\,M_\odot$. According to recent studies, low metallicity star-forming galaxies get the majority of their He^+ ionizing photons from high mass X-ray binaries (Schaerer et al. 2019). We measure the X-ray luminosity of each bin using the L_{X}-SFR-Z relation

found by Brorby et al. (2016). We find that the X-ray luminosity is on average larger for galaxies with higher $L(\text{H}\alpha)/L(\text{UV})$. This result may suggest the presence of luminous HMXBs, which could explain the high nebular HeII emission observed for galaxies with high Hα-to-UV ratios. As HMXBs have short lifespans (a few Myr), they effectively indicate recent star formation. Nonetheless, the potential abundance of HMXBs in the $high$-$L(\text{H}\alpha)/L(\text{UV})$ group does not directly imply that galaxies in this subset primarily experience a bursty SFH, since massive stars and HMXBs are being continuously formed even in a constant SFH. In addition, the idea that the $high$-$L(\text{H}\alpha)/L(\text{UV})$ sample is in a burst mode of star formation is not supported by the fact that the equivalent width of the CIV and SiIV P-Cygni features do not vary between the two subsamples. The presence of a more intense ionizing spectrum in galaxies with higher $L(\text{H}\alpha)/L(\text{UV})$ ratios can be backed by the abundance of HMXBs in these galaxies, potentially accounting for the observed differences in SFRs.

Our results cast doubt upon the reliability of Hα-to-UV luminosity ratio in tracing bursty SFH of typical star-forming galaxies at $z \sim 2$. This is due to the absence of evidence suggesting that galaxies with higher $L(\text{H}\alpha)/L(\text{UV})$ are experiencing a burst, based on their average stellar population age and the lack of variation in P-Cygni features compared to galaxies with lower $L(\text{H}\alpha)/L(\text{UV})$. There is one important implication of this work. It is proposed that star-forming galaxies may be in a bursty phase of star formation at the beginning of the reionization epoch, producing enough ionizing photons to reionize the intergalactic medium. If such is the case, it is important to validate the tracer of burstiness which commonly used in the literature, and whether there are other phenomenon that can

affect the Hα-to-UV ratio. Using the next generation telescopes, we will have access to even more high quality data to study the Hα-to-UV ratio variations in more details. For example, James Webb Space Telescope can provide high resolution rest-FUV spectra of high redshift galaxies to aid constraining the mode of star formation history and/or hardness of the ionizing spectrum and the causes of the variations in the Hα-to-UV ratio.

Several studies of high redshift galaxies have found evidence of bursty SFHs by comparing Hα and UV SFRs (e.g., Atek et al. 2022 at $z \sim 1.1$, and Faisst et al. 2019 at $z \sim 4.5$). These works suggest that the excess found in the Hα SFR relative to the UV SFR can only be explained by additional bursts of star formation on top of an underlying smooth star formation. The aforementioned studies have found that SFR[Hα]/SFR[UV] ratio is preferentially higher for lower mass galaxies. Galaxies of lower masses, which are also likely to have a lower metallicity, may be conducive to an IMF that is top-heavy (Tremonti et al. 2004b; Dalcanton 2007; Lara-López et al. 2010; Peeples & Shankar 2011; Lilly et al. 2013; Andrews & Martini 2013; Zahid et al. 2014; Chisholm et al. 2018), and therefore one must be very careful in interpreting the Hα-to-UV ratio for such galaxies. The equivalent width of the stellar photosphere features investigated in this work (Section 3.5.2) is less affected by the uncertainties associated with the $L(\text{H}\alpha)/L(\text{UV})$ ratio, such as variations in ionizing escape fraction, stochastic IMF, and dust reddening. Further research is necessary to better understand the effectiveness of these indicators in tracing starburst activity, as well as how to optimally use them in conjunction with resolved indicators.

Acknowledgements

Data Availability

In this work, we use spectroscopic redshifts and rest-frame optical line measurements obtained from the MOSFIRE Deep Evolution Field (MOSDEF) survey (Kriek et al. 2015). This is publicly available at `https://mosdef.astro.berkeley.edu/`.

We also use photometry obtained from the CANDELS (Grogin et al. 2011; Koekemoer et al. 2011) and reprocessed by the 3D-HST grism survey team (Brammer et al. 2012; Skelton et al. 2014; Momcheva et al. 2016). The data sets and catalogs can be found at `https://archive.stsci.edu/prepds/3d-hst/`.

We analyze the Far-UV spectra obtained by the Low Resolution Imagerand Spectrometer (LRIS; Oke et al. 1995; Steidel et al. 2004). Topping et al. (2020) and Reddy et al. (2022) contain information about the MOSDEF/LRIS data reduction. MOSDEF/LRIS data sets are available upon request.

Chapter 4

Optimum Stellar Metallicity and Dust Attenuation Curve Combinations to Reconcile Various Star-formation Rates

Abstract In this study, we examine the variation of the shape of the stellar dust attenuation curve with stellar metallicity through the reconciliation of star formation rates (SFRs) derived from Hα and SED modeling by analyzing optical and rest-frame far-UV spectra of $z \sim 2$ star-forming galaxies from the MOSFIRE Deep Evolution Field (MOSDEF) survey. Utilizing a sample of 412 star-forming galaxies with MOSFIRE optical spectra, we identify

optimal metallicity and dust curve combinations that reconcile Hα and SED-derived SFRs. Our results confirm that sub-solar metallicity stellar populations reddened with the SMC curve, and solar metallicity models reddened with the Calzetti curve, provide the best agreement between SFRs. Additionally, we investigate the potential variation of the dust attenuation curve with stellar mass using 124 star-forming galaxies with deep Keck/LRIS rest-frame far-UV spectra, divided into two ensembles of galaxies with low and high average stellar mass. We find that using SPS models that are reddened with the SMC curve offers a better match between the Hα and SED-derived SFRs for both populations compared to those reddened with the Calzetti curve. When using models reddened with the SMC curve, the high-mass subset exhibits, on average, a stellar metallicity of $Z_* = 0.153 \pm 0.014\,Z_\odot$, compared to $Z_* = 0.183 \pm 0.08\,Z_\odot$ for the low-mass galaxies. This outcome confirms that galaxies with sub-solar metallicities follow a stellar dust attenuation curve, which has a similar shape to that of the SMC curve.

4.1   introduction

One of the primary sources of uncertainty in determining the stellar population properties at high redshifts is the shape of the stellar dust attenuation curve and its potential dependence on the physical properties of galaxies. Dust attenuation can significantly impact the interpretation of galaxy properties, such as star formation rates, stellar metallicities, and stellar ages, especially at high redshifts where dust effects can be more pronounced (Kewley et al. 2002; Draine 2003; Lee et al. 2009; Reddy et al. 2012; Reddy et al. 2015; Shivaei et al. 2015, 2018a; Narayanan et al. 2018b; Theios et al. 2019). Therefore, understanding the

relationship between the shape of the stellar dust attenuation curve and galaxy physical properties is crucial for accurately characterizing the properties of high-redshift galaxies and their evolution over cosmic time.

Dust particles in the interstellar medium (ISM) affect starlight through wavelength-dependent obscuration or reddening. Dust extinction and/or attenuation curves are used to express the dependency of dust reddening as a function of wavelength. Extinction curves rely on many factors, such as the chemical composition and size distribution of dust grains, and can be directly measured by observing light that has passed through a dust screen along the line of sight. On the other hand, attenuation curves represent the overall effect of dust obscuration on a group of stars given a specific geometry between the stars and dust. In the local universe, observed extinction/attenuation curves along various sight-lines exhibit a broad range of behaviors (Salim & Narayanan 2020). Notable examples include curves from the Milky Way (Cardelli et al. 1989a), the Small and Large Magellanic Clouds (Fitzpatrick & Massa 1990a; Gordon et al. 2003b; Fitzpatrick & Massa 2007), M31 (Bianchi et al. 1996a), and the Calzetti et al. (2000b) curve which is based on local starburst galaxies, all of which display distinct characteristics in terms of the UV bump and slope.

Variations in extinction/attenuation curves have also been observed in the high-redshift universe (Bianchi et al. 1996a; Gordon et al. 2003b; Fitzpatrick & Massa 2007; Salim et al. 2007). The shape of the dust attenuation curve for these galaxies has been shown to be consistent with the SMC, Calzetti et al. (2000b) curve, or an intermediate form, depending on properties such as stellar mass, metallicity, and sSFR (Reddy et al. 2006a; Daddi et al. 2007; Pannella et al. 2009; Reddy et al. 2010; Reddy et al. 2012; Buat et al.

2012b; Reddy et al. 2015, 2018b; McLure et al. 2018; Fudamoto et al. 2020; Shivaei et al. 2020b). Notably, in a study of high-redshift ($z \sim 2$) galaxies, Shivaei et al. (2020b) found that those with high gas-phase metallicities have an average curve resembling the Calzetti curve, while those with low metallicities display a steeper slope similar to the SMC curve. In another study of $z \sim 2$ star-forming galaxies, Reddy et al. (2018b) demonstrated that the correlation between dust attenuation (IRX) and UV slope (β) for sub-solar metallicity stellar populations is best predicted with the SMC curve, whereas the Calzetti curve accurately reproduces this correlation for solar metallicity populations.

Understanding dust attenuation at high redshifts is of paramount importance for accurately estimating galaxy properties and, consequently, the star formation history and evolution of the Universe. However, accurately measuring dust attenuation curves at high redshifts presents numerous challenges, such as the limited availability of direct measurements and the reliance on indirect methods or extrapolations from local galaxies (Charlot & Fall 2000b; Capak et al. 2007; Reddy et al. 2012; Scoville et al. 2015). One effective method to constrain the relative shape of the dust attenuation curve involves reconciling the Hα- and UV-derived SFRs (Gilbank et al. 2010). Under the assumption of a constant or slowly rising star-formation history (SFH) with a characteristic timescale of $\tau \gtrsim 50\,\mathrm{Myr}$ (Papovich et al. 2001; Reddy et al. 2012), the Hα-to-UV luminosity ratio achieves equilibrium after several tens of Myr (Leitherer & Heckman 1995; Elmegreen 2006; Pflamm-Altenburg et al. 2007; Meurer et al. 2009; Pflamm-Altenburg et al. 2009; Hoversten & Glazebrook 2008; Boselli et al. 2009; Mas-Ribas et al. 2016). The Hα-to-UV luminosity equilibrium is contingent upon minimal variations in factors such as the ionizing photon production rate per unit

SFR (Steidel et al. 2001; Shapley et al. 2006; Siana et al. 2007), nebular and stellar dust reddening (Kewley et al. 2002; Lee et al. 2009; Reddy et al. 2012; Reddy et al. 2015; Shivaei et al. 2015, 2018a; Theios et al. 2019; Fetherolf et al. 2021), stellar metallicity (Bicker & Fritze-v. Alvensleben 2005; Boselli et al. 2009), and the relative optical depths of UV and Hα emission.

To mitigate the above-mentioned factors that effect Hα-to-UV ration, one approach is to conduct a stacking analysis and examine the average SFRs of galaxy ensembles. In this case, the mean Hα- and UV-derived SFRs of a galaxy ensemble, which have varying sensitivities to factors such as metallicity, IMF, and dust, should yield consistent SFR values provided the treatment of these factors is uniform. In addition to these considerations, it is crucial to ensure that the assumptions of a constant star formation history (SFH) and a universal initial mass function (IMF) hold true when reconciling Hα and UV SFRs. When investigating an entire high-redshift galaxy rather than individual massive star clusters, the integrated emission of numerous unresolved H II regions is considered, featuring average dynamical timescales considerably longer than a few million years (Shapley et al. 2001; Papovich et al. 2001; Reddy et al. 2012). Consequently, the galaxy-averaged SFH and IMF are more accurately represented by a continuous SFH as opposed to an instantaneous burst model and varying IMF (Meurer et al. 2009; Rezaee et al. 2022).

The MOSFIRE Deep Evolution Field (MOSDEF) survey (Kriek et al. 2015), which covered the CANDELS fields (Grogin et al. 2011; Koekemoer et al. 2011), offers an exceptional dataset for this study for several reasons. First, the availability of rest-frame optical spectra targeting Balmer recombination lines allows for the probing of short timescale SFRs

($\sim 10\,\mathrm{Myr}$) in the $z \sim 2$ star-forming galaxies. Second, the deep HST imaging of MOS-DEF targets is essential, as it enables the estimation of SFRs on longer timescales ($50\,\mathrm{Myr}$) using broadband photometry-based SED modeling. Finally, the availability of rest-frame far-UV spectra from the MOSDEF-LRIS survey for these targets presents an opportunity to estimate the stellar metallicity of ensembles of galaxies, further enriching the analysis. In addition to the previously mentioned factors, the availability of IR data for some MOSDEF galaxies, detected in the *Spitzer*/MIPS $24\,\mu\mathrm{m}$ band or *Herschel*/PACS 100 and $160\,\mu\mathrm{m}$ bands, allows us to calculate bolometric SFRs. Comparing bolometric SFRs with those derived from Hα or SED-fitting helps evaluate the decoupling between UV and IR emission, as well as providing insights into optically-thick star-forming regions within a galaxy (e.g., Casey et al. 2009, 2014; Reddy et al. 2012; Miettinen, O. et al. 2017).

The primary goal of this study is to investigate the variation of the shape of the stellar dust attenuation curve with galaxy properties, such as stellar metallicity and stellar mass, in $z \sim 2$ galaxies. This is achieved by reconciling Hα-derived and UV-derived SFRs using different combinations of attenuation curves and stellar metallicities. By incorporating IR data and comparing bolometric SFRs with Hα and SED-derived SFRs, we also aim to gain a deeper understanding into the amount and geometry of dust obscuration within these galaxies. The structure of this paper is organized as follows. Section 4.2 introduces the samples used in this study, along with a description of the sample selection criteria and data reduction procedures. Section 4.3 outlines the methods used for SED modeling and the construction of composite spectra. Section 4.4 presents our findings on the reconciliation of Hα and SED-derived SFRs for both individual and stacked spectra within stellar mass

bins. Finally, our conclusions are discussed in Section 4.5. All wavelengths are presented in the vacuum frame. We assume a flat cosmology with $H_0 = 70\,\mathrm{km\,s^{-1}}$, $\Omega_\Lambda = 0.7$, and $\Omega_m = 0.3$. Throughout this work, we adopt a Chabrier (2003) initial mass function (IMF).

4.2 Sample

4.2.1 MOSDEF: Rest-Frame Optical Spectroscopy

The MOSDEF survey (Kriek et al. 2015) acquired rest-frame optical spectra of around 1500 star-forming galaxies and active galactic nuclei (AGNs) using the Keck/MOSFIRE spectrograph (McLean et al. 2012). The target galaxies were located in the five CANDELS extragalactic fields (Grogin et al. 2011; Koekemoer et al. 2011): GOODS-S, GOODS-N, UDS, COSMOS, and AEGIS, and were selected to be within three redshift bins: $1.37 < z < 1.70$, $2.09 < z < 2.61$, and $2.95 < z < 3.80$. This selection ensured that several strong rest-frame optical emission lines, such as [OII]$\lambda 3727, 3730$, Hβ, [OIII]$\lambda\lambda 4960, 5008$, H$\alpha$, [NII]$\lambda\lambda 6550, 6585$, and [SII]$\lambda 6718, 6733$, were redshifted into the YJH, JHK, and HK transmission windows. For further details on the survey and MOSFIRE data reduction, refer to Kriek et al. (2015).

In this study, we use the emission line fluxes and spectroscopic redshifts measured by the MOSDEF survey. The spectroscopic redshifts were estimated based on the wavelength of the highest S/N emission line. Emission line fluxes were determined by fitting a Gaussian function with an underlying linear continuum. The Hα and Hβ emission lines and the [NII] doublet were fit simultaneously using three Gaussian functions. The Hα and

Hβ emission line measurements were corrected for underlying Balmer absorption using the best-fit stellar population models (Reddy et al. 2020).

The final sample utilized in reconciling Hα and SED SFRs (Section 4.4.1) comprises of 442 star-forming galaxies with redshifts between $1.25 < z < 2.65$, which meet several of the following criteria. All galaxies in the final sample must have secured systemic redshifts obtained from the MOSDEF spectroscopy, which is based on multiple emission features detected with $S/N \geq 2$ and strong detection of Hα and Hβ emission lines ($S/N \geq 3$). Only star-forming galaxies were included, while AGNs were excluded based on their X-ray luminosities, IR properties, or [NII]$\lambda6584$/Hα line ratios (Coil et al. 2015; Azadi et al. 2018; Leung et al. 2019). This sample is referred to as the "MOSDEF/Optical" sample throughout this work.

4.2.2 MOSDEF-LRIS: Rest-Frame Far-UV spectroscopy

A subset of MOSDEF galaxies were chosen for rest-frame far-UV (FUV) spectroscopic follow-up observations using the Keck I/Low-Resolution Imager and Spectrometer (LRIS; Oke et al. 1995; Steidel et al. 2004). This subset contains 259 objects selected based on the following prioritized criteria. First, targets with strong detection ($S/N \geq 3$) of BPT emission lines ([OIII], Hβ, [NI]$\lambda6584$, and Hα) were chosen. Next, objects with available Hα, Hβ, and [OIII] lines, as well as an upper limit on [NII], were included. Additionally, MOSDEF objects with or without secure MOSDEF spectroscopic redshift measurements were considered. Finally, objects within the MOSDEF survey redshift ranges that were not

part of the MOSDEF survey but had 3D-HST[1] (Brammer et al. 2012; Skelton et al. 2014) photometric redshifts and apparent magnitudes were given the lowest priority.

The rest-FUV LRIS spectra were obtained in GOODS-S, GOODS-N, AEGIS, and COSMOS extragalactic fields, encompassing nine multi-object slitmasks using $1''2$ slits. The blue and red sides of LRIS were recorded with the $400\,\mathrm{line/mm}$ grism and the $600\,\mathrm{line/mm}$ grating blazed at $4300\,\text{Å}$ and $5000\,\text{Å}$, respectively. The combined spectrum of each object features a continuous wavelength range extending from the atmospheric cutoff at $\lambda \simeq 3100\,\text{Å}$ to $\lambda \sim 7000\,\text{Å}$, with the reddest wavelength cutoff varying depending on the slit's location in the spectroscopic field of view. The spectral resolutions for the blue and red sides of LRIS are $R \sim 800$ and $R \sim 1300$, respectively. The final MOSDEF/LRIS sample employed in Section 4.4.3 contains 124 star-forming galaxies with redshifts range of $1.42 < z < 2.58$. These galaxies fulfill the same S/N ratio and redshift measurement criteria as outlined in Section 4.2.1.

4.3 measurements

4.3.1 SED modeling

We employ the Binary Population and Spectral Synthesis (BPASS) version 2.2.1 models (Eldridge et al. 2017; Stanway & Eldridge 2018) in this work to determine the physical properties of each galaxy, such as SFR (SFR[SED]), stellar continuum reddening $(\mathrm{E(B-V)_{cont}})$, stellar population age, and stellar mass $(\mathrm{M_*})$. The advantage of using BPASS models is that they incorporate the effect of binary stellar evolution, which has

---

[1] https://archive.stsci.edu/prepds/3d-hst/

been shown to be an important assumption for reproducing some FUV spectral features (e.g., HeII $\lambda1640$ Å) observed in the spectra of high redshift galaxies (Steidel et al. 2016; Eldridge et al. 2017; Reddy et al. 2022). Three sets of parameters are used to characterize the BPASS models: stellar metallicity (Z_*), the upper mass cutoff of the IMF (M_{cutoff}), and the choice to include binary stellar evolution. The stellar metallicity range of the models is $Z_* = [10^{-5}, 0.04]$ in terms of mass fraction of metals, with solar metallicity equal to $Z_\odot = 0.0142$. Two upper mass limits of $100\,M_\odot$, and $300\,M_\odot$ are considered for the IMF. These models are referred to as "100bin", "300bin", "100sin", and "300sin", where the first numbers indicate the upper mass cutoff of the IMF, and the terms "bin" or "sin" refer to the binary or singular stellar evolution assumptions, respectively (Reddy et al. 2022).

Previous studies have shown that SPS models with an assumption of constant star-formation history are better suited for modeling typical high redshift galaxies ($z \sim 2$) compared to models that assume instantaneous burst SFH (Shapley et al. 2001; Papovich et al. 2001; Reddy et al. 2012). The latter may be better suitable for age-sensitive individual massive star clusters, whereas the former is better suited for objects with large dynamical timescales ($\sim 100\,\mathrm{Myr}$), which is the case in high redshift galaxies (e.g., Shapley et al. 2001; Papovich et al. 2001; Reddy et al. 2012). The original instantaneous burst BPASS models are combined to create constant SF models for stellar ages ranging from 10^7 to 10^{10} yr, with increments of 0.1 dex. The SPS models are reddened using the SMC (Gordon et al. 2003b) and Calzetti et al. (2000b) dust curves for a stellar continuum reddening range of $E(B - V)_{\mathrm{cont}} = [0.00, 0.60]$. As mentioned earlier, these curves have been shown to be consistent with the attenuation curves derived for typical high redshift star-forming

galaxies. The `Cloudy` radiative transfer code version 17.02 (Ferland et al. 2017) is used to add the nebular continuum to the SPS models.

4.3.2 Composite Spectra

To investigate the average physical properties (e.g., SFR, stellar age, metallicity) of a group of galaxies, we create optical and FUV stacked spectra, which offer a higher S/N compared to individual spectra. We follow the same methods outlined in Reddy et al. (2016, 2020, 2022) and Shivaei et al. (2018a) for constructing the FUV and optical composite spectra. In brief, individual science and error spectra within a particular ensemble are shifted to the rest-frame based on their MOSDEF spectroscopic redshifts, converted to luminosity density, and interpolated to a linear wavelength grid with a spacing of $0.5\,\text{Å}$. At each wavelength point, a composite spectrum represents the average of the luminosity density values after excluding the 3σ outliers. An example of the optical and FUV composite spectrum is shown in Figure 4.1. To determine the error in a composite spectrum at each wavelength point, we employ bootstrap resampling to create 100 realizations. Individual spectra are perturbed according to their spectral errors, and the stacked spectra are built for each realization. The standard deviation of the luminosity density values at each wavelength point is assigned as the error in the composite spectrum. This error is utilized when calculating the chi-squared between the SPS models and the composite spectrum.

We use the SPS models to fit the FUV composite spectra, which allows us to calculate the average stellar age, stellar metallicity, stellar reddening, and SFR[SED] for collections of galaxies. The SPS models mentioned earlier are interpolated to incorporate
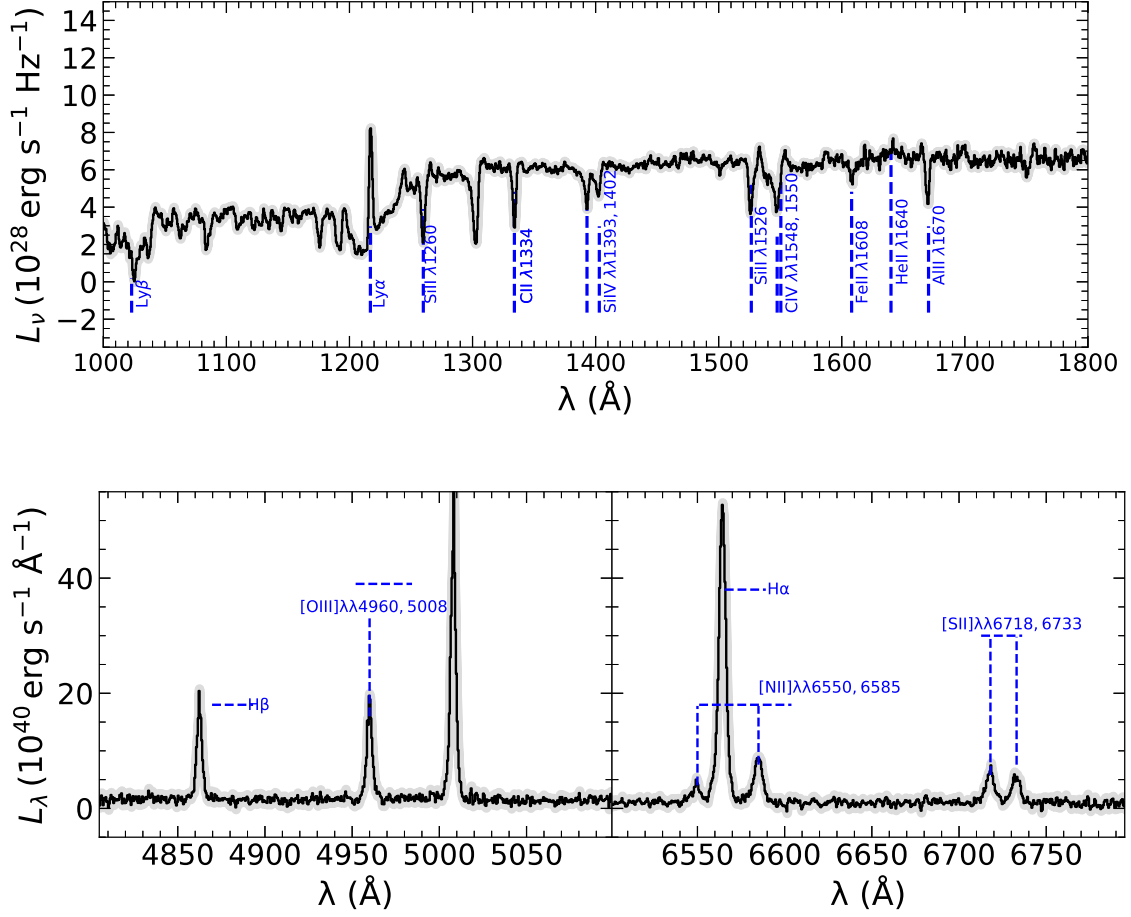
Figure 4.1: *Top* : FUV composite spectrum of the 124 star-forming galaxies in the MOS-DEF/LRIS sample. Some FUV spectral features are labeled in blue. The 1σ uncertainty in the spectrum is shown in grey. *Bottom* : optical composite spectrum of the 124 star-forming galaxies in the MOSDEF/LRIS sample alongside the 1σ uncertainty. Some optical spectral features including Balmer recombination lines are shown in blue.
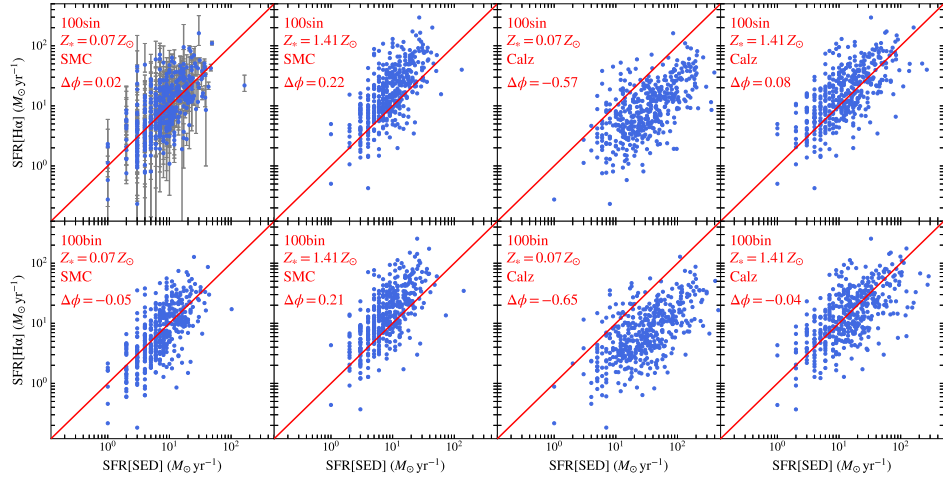
Figure 4.2: Comparison of the Hα and SED-inferred SFRs for different stellar population assumptions (sub-solar and solar metallicities, SMC and Calzetti et al. (2000b) dust attenuation curves, inclusion of binary stellar evolution) used for SED modeling of galaxies in the MOSDEF/Optical sample for which a $S/N \geq 3$ is required for detection of Hα and Hβ. The median log difference between SFR[Hα] and SFR[SED] is indicated in each panel as $\Delta\phi$.

stellar metallicities comparable to those estimated for $z \sim 2$ galaxies (Steidel et al. 2016). The ionization parameter and gas-phase oxygen abundance in the models remain fixed at the average values of the MOSDEF/LRIS sample ($\langle \log U \rangle = -3.0$, $\langle \log[Z_{\mathrm{neb}}/Z_\odot] \rangle = -0.4$; Topping et al. 2020; Reddy et al. 2022).

4.4   Results

4.4.1   Reconciling Hα and SED-Derived SFRs

In this section, we present the results of reconciling SFR[Hα] and SFR[SED] for different stellar population assumptions, using the 412 galaxies in the MOSDEF/Optical sample. We compare SFRs from models with metallicities of $0.07\,Z_*$ and $1.41\,Z_*$, considering the "100bin", "300bin", "100sin", and "300sin" model assumptions. The conversion factors between the dust-corrected Hα luminosity and SFR[Hα] are 2.675, 4.888, 2.102, and $4.236 \times 10^{-42}\,M_\odot \mathrm{yr}^{-1}\mathrm{erg}^{-1}\mathrm{s}$ for the "$0.07\,Z_\odot$ 100sin", "$1.41\,Z_\odot$ 100sin", "$0.07\,Z_\odot$ 100bin", and "$1.41\,Z_\odot$ 100bin", respectively, where a Chabrier (2003) IMF is assumed. Due to the inclusion of binary systems in some models, the main sequence lifetimes of O-stars can be up to three times longer than those of single stars with the same mass. Consequently, a larger H-ionizing flux per unit SFR and a lower Hα luminosity to SFR conversion factor are anticipated for models that include binary systems.

Our SFR comparison results for various model assumptions are summarized in Figure 4.2. We computed the median log difference between the Hα and SED-inferred SFRs, denoted as $\Delta\phi$, to provide a quantitative assessment of the agreement between SFR[Hα]
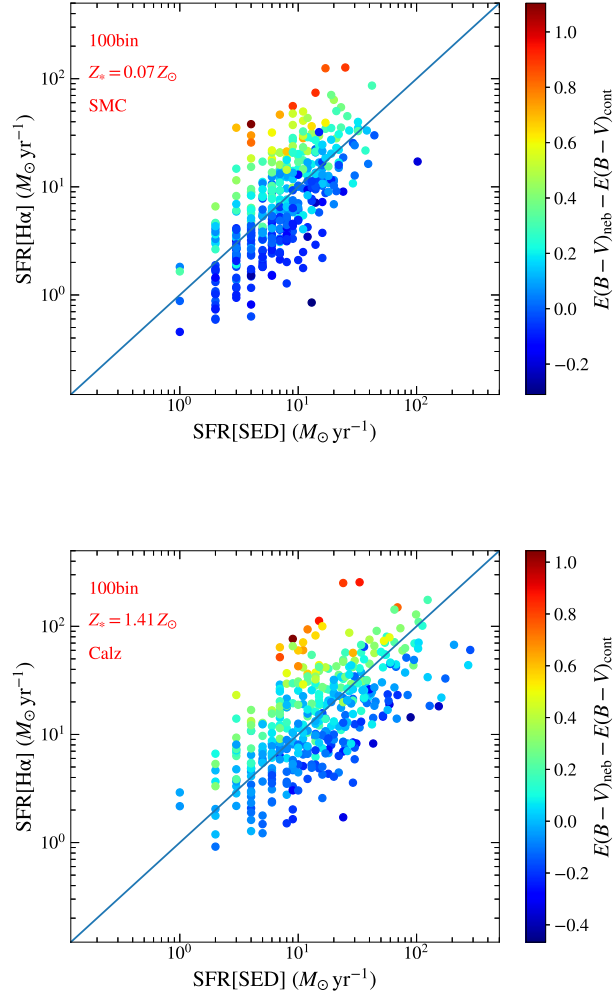
Figure 4.3: SFR[Hα] versus SFR[SED] color-coded by the differential reddening for the two model assumptions that include binary stellar evolution and yielded the lowest Δφ (The median log difference between SFR[Hα] and SFR[SED]) using the final MOSDEF/Optical sample (Section 4.2.1).

and SFR[SED]. When the dust curve remains constant, $\Delta\phi$ exhibits significant variation with stellar metallicity. However, the inclusion of binary systems does not notably impact $\Delta\phi$ when both stellar metallicity and the dust curve are fixed. Among all combinations of SPS models discussed, the best agreement between Hα and SED-inferred SFRs is achieved with subsolar metallicity models reddened by the SMC curve and solar metallicity models reddened by the Calzetti curve. These two combinations of stellar metallicity and dust curve are the same as those identified by Reddy et al. (2010, 2018b) as effectively predicting the relationship between dust attenuation and UV slope.

We investigate the observed discrepancies between SFR[Hα] and SFR[SED] for our sample galaxies in more detail. Focusing on the two models incorporating binary evolution with the lowest $\Delta\phi$, we explore the relationship between SFR and differential reddening $(E(B-V)_{\rm neb}$-$E(B-V)_{\rm cont})$. As illustrated in Figure 4.3, the discrepancies between SFR[Hα] and SFR[SED] increase as the differential reddening rises (due to extremely high $E(B-V)_{\rm neb}$). Notably, for galaxies with very high differential reddenings $(E(B-V)_{\rm neb} \sim 1)$, SFR[H$\alpha$] is considerably larger (on average by a factor of ~ 6) than the SFRs predicted through SED-fitting. Reddy et al. (2015) also observed these offsets and suggested that they are due to optical depth effects, as the UV/optical stellar continuum is mainly sensitive to less-reddened stellar populations. To further investigate this hypothesis, we utilize the available IR data for MOSDEF galaxies to study the bolometric SFR and compare it to other SFR indicators.
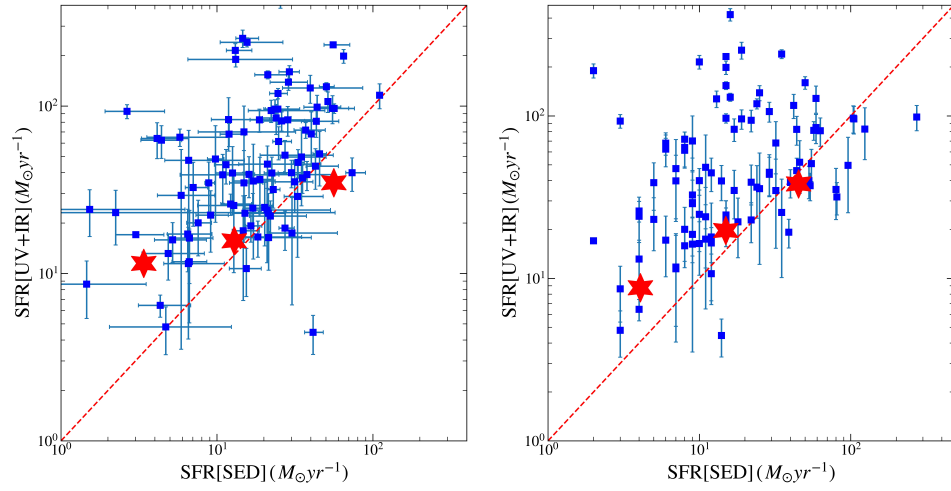
Figure 4.4: Comparison of the Hα and SED-inferred SFRs with IR+UV SFRs for objects (blue points) that are directly detected at 160, 100, and/or 24 μm. . The red stars show the average bolometric SFRs estimated by stacking the Herschel/PACS data in bins of SFR[Hα] and SFR[SED] without the IR detection requirement considered for the blue points.

4.4.2 Bolometric SFRs

Infrared emission primarily arises from dust heated by radiation in star-forming regions, as it re-emits absorbed light. By combining dust-obscured SFRs obtained from IR emission with unobscured SFRs derived from UV emission, we can achieve a more comprehensive and reddening-insensitive calculation of bolometric SFRs. This approach effectively compensates for the impact of dust obscuration, which can hinder the accuracy of SFR measurements when relying solely on UV or optical observations. To further investigate into this possibility, we compare SFR(IR + UV) with SFR[Hα], and SFR[SED].

To estimate SFR[IR + UV] for galaxies detected only in the Spitzer/MIPS 24μm band, we applied the metallicity-dependent conversion factor between rest-frame 7.7μm emission and IR luminosity (L(IR)) from Shivaei et al. (2017), and the Kennicutt (1989) conversion factor between L(IR) and SFR[IR], adapted for a Chabrier (2003) IMF. For galaxies detected in Herschel/PACS 100μm and 160μm bands, we computed L(IR) by fitting a dust SED model to the PACS data using Rieke et al. (2009) models, which yield L(IR) values within 20% of those from Chary & Elbaz (2001) templates. As most galaxies lack direct PACS bands detection, we stacked available data, fit dust SED models to stacked PACS photometry, and determined L(IR) and SFR[IR]. To explore the agreement between various SFRs, we divided IR data into three bins of both SFR[Hα] and SFR[SED]. The lowest SFR bin contains twice the number of galaxies compared to the middle and high SFR bins.

Figure 4.4 presents a comparison between the bolometric SFR and SFR[Hα] in the left panel, as well as the bolometric SFR and SFR[SED] in the right panel. The com-

parison is shown for both individual galaxies with IR detection and stacked data in bins of SFR[Hα] and SFR[SED] regardless of IR detection. The requirement for IR detection introduces a selection bias, which leads to the preferential selection of galaxies with larger SFRs and more dust-obscured. We notice considerable discrepancies between SFR[IR+UV] and both SFR[Hα] and SFR[SED]. These differences are more evident in galaxies within the lower SFR bins. In particular, galaxies with SFR[Hα] $\lesssim 11\,M_\odot/\mathrm{yr}$ exhibit an average $\langle\mathrm{SFR[IR+UV]}\rangle$ that is higher by a factor of approximately 3.3. Similar offsets are found with SFR[SED], where galaxies with SFR[SED] $\lesssim 11\,M_\odot/\mathrm{yr}$ have an average $\langle\mathrm{SFR[IR+UV]}\rangle$ that is higher by a factor of 2.0. These discrepancies can be attributed to galaxies with optically-thick star-forming regions. In these regions, the dust absorbs a significant portion of the emitted Hα radiation, leading to an underestimation of the ionized gas and, consequently, the star formation rate. In addition, in galaxies with optically-thick star-forming regions, the heavy dust obscuration can alter the observed UV-Optical SED, making it difficult to accurately estimate the contribution of the obscured star formation to the overall SED. This can be seen in dusty galaxies that have unexpectedly blue SEDs, as noted in various studies (e.g., Frayer et al. 2000; Goldader et al. 2002; Smail et al. 2004; Chapman et al. 2005; Reddy et al. 2006b; Casey et al. 2009; Howell et al. 2010; Hodge et al. 2012; Fu et al. 2012; Casey et al. 2014; Miettinen, O. et al. 2017). These findings suggest a decoupling between IR and UV emissions in such galaxies.

In the prior section, our examination revealed inconsistencies between SFR[Hα] and SFR[SED]. We noticed a pattern between these discrepancies and SFR, such that the inconsistencies become more pronounced at higher SFR[Hα]. Furthermore, it was high-

lighted that these differences are more pronounced at higher levels of differential reddening. As a result, we attributed these discrepancies to the decoupling between the less-reddened regions dominating the UV emission and the dust-obscured regions dominating the Hα emission. If this were the case, we would expect discrepancies between SFR[IR+UV] and SFR[SED] in the high SFR bin. However, when stacking galaxies into bins based on SFR, we observed a good agreement between the $<$ SFR[Hα] $>$ and $<$ SFR[SED] $>$ for the high SFR bin. This result suggests that the estimated SFRs using the Hα emission line in galaxies with high SFRs may be over-estimated. This could potentially be attributed to the variation of the nebular attenuation curve with SFR. Specifically, higher SFR galaxies could exhibit a steeper attenuation curve at rest-frame optical wavelengths or a lower ratio of total-to-selective absorption at the V-band ($R_{\rm V}$) compared to lower SFR galaxies. In a study of MOSDEF galaxies conducted by Reddy et al. (2020), the shape and normalization of the nebular dust attenuation curve were found to be most similar to that of the MW curve. The authors suggest that in order to investigate variations in the shape of the curve with physical properties a galaxy, a larger sample size with high signal-to-noise detection of both Balmer and Paschen lines is required. Aperture uncertainties is also another factor causing discrepancies between SFR[Hα] and SFR[SED], and also affect the differential reddening. Since Hα and Hβ luminosity are measured through slit spectroscopy while SFR[SED] and stellar reddening are measured through SED fitting to broadband photometry. Fetherolf et al. (2021) used a MOSDEF sample comparable to the sample used in this work in terms of the range of physical properties and found that aperture correction cannot

explain the observed differences between SFR[Hα] and SFR[SED] for the high SFR[Hα] and high $E(B-V)_{\mathrm{neb}}$.

Another factor that could influence the conversion factor between dust-corrected L(Hα) and SFR[Hα] is stellar metallicity. A lower stellar metallicity leads to a higher ionizing photon production rate per unit SFR, and consequently, for a given Hα luminosity, a lower metallicity model would imply a lower SFR. As pointed out in Section 4.4.1, the $0.07\,Z_*$ models have a conversion factor that is approximately 2 times lower than the models with $1.41\,Z_*$. It is improbable for the galaxies in our sample to have such extensive variations in stellar metallicities. Indeed, a number of high redshift studies propose that galaxies akin to those in the sample for this work are characterized by sub-solar metallicity (e.g., Erb et al. 2006; Somerville & Primack 1999; Steidel et al. 2016; Reddy et al. 2022). Nonetheless, it is essential to further investigate this possibility by constraining the average stellar metallicity of MOSDEF/LRIS galaxies to examine its variations.

Table 4.1: Stellar mass (M_* ($10^{10} M_\odot$)) subsamples

Attenuation Curve[a]	Subsample	$\langle M_* \rangle$[b]	$\langle \log[\mathrm{Age/yr}] \rangle$[c]	$\langle Z_*/Z_\odot \rangle$[d]	$\langle E(B-V) \rangle_{\mathrm{cont}}$[e]	$\langle E(B-V) \rangle_{\mathrm{neb}}$[f]
SMC	low−mass	0.45 ± 0.03	8.5 ± 0.1	0.183 ± 0.008	0.067 ± 0.002	0.42 ± 0.03
	high−mass	2.34 ± 0.18	8.8 ± 0.2	0.153 ± 0.014	0.146 ± 0.005	0.50 ± 0.02
Calzetti+00	low−mass	0.45 ± 0.03	8.5 ± 0.1	0.172 ± 0.007	0.168 ± 0.005	0.39 ± 0.02
	high−mass	2.34 ± 0.18	8.8 ± 0.2	0.141 ± 0.012	0.374 ± 0.011	0.47 ± 0.02

[a] Dust attenuation curve used for the reddening of the stellar continuum.

[b] Mean stellar mass.

[c] Mean stellar population age.

[d] Mean stellar metallicity.

[e] Mean stellar reddening.

[f] Mean nebular reddening.

[g] Mean Hα star-formation rate.

[h] Mean SED star-formation rate.

4.4.3 Stellar Mass, Metallicity, and SFR Reconciliation

In this section, we further explore the reconciliation between Hα and SED-derived SFRs by analyzing stacked rest-frame FUV and optical spectra of MOSDEF sample galaxies, binned by stellar mass. We divide the MOSDEF/LRIS sample into two equal-number subsamples based on stellar masses (Table 4.1), enabling us to investigate the most relevant attenuation curve that brings the best agreement between SFR[Hα] and SFR[SED] for galaxies across different stellar masses. We also constrain the stellar metallicity as a function of mass by modeling the FUV stacked spectra with SPS models. By constraining the stellar metallicity of ensembles of galaxies, we can further investigate the stellar metallicity variation across our sample galaxies.

We stack the rest-frame FUV and optical spectra to calculate the average SFR[Hα] and SFR[SED] of galaxies in each bin. The best-fit SPS model to the FUV composite spectrum is used to estimate the stellar population age, stellar metallicitiy, SFR[SED], and the conversion factor that relates $L(\text{H}\alpha)$ to SFR[Hα] for each bin. Table 4.1 presents the derived physical properties for each stellar mass bin. The dividing threshold in stellar mass between the low- and high-mass subset is $10^{10}\,M_\odot$. When assuming the SMC curve for reddening of the SPS models, the high-mass subset exhibits, on average, a stellar population age of $\log[\text{Age/yr}] = 8.8$ and a stellar metallicity of $Z_* = 0.153\,Z_\odot$, compared to $\log[\text{Age/yr}] = 8.5$ and $Z_* = 0.183\,Z_\odot$ for the low-mass galaxies. The difference in stellar age and metallicity of the two subsets are significant at 2σ and 3σ level, respectively. Figure 4.5 illustrates the comparison between the average SFR[Hα] and SFR[SED] derived for the stellar mass subsets, assuming SMC or Calzetti curves for the reddening of the SPS models. We find

a better agreement between the mean Hα and SED SFRs when assuming an SMC curve for both subsets. This finding contradicts the general consensus in the literature that high-mass galaxies are better described by a Calzetti curve (Shivaei et al. 2020b). However, it is consistent with our previous conclusion that the SMC curve offers the best agreement between the Hα and SED SFRs for galaxies with sub-solar stellar metallicity.

As discussed in the previous section, if the discrepancies observed between the SFR[Hα] and SFR[SED] for the high SFRs are due to the variations in the stellar metallicity of sample galaxies, our expectation is that the average metallicities derived for the low- and high-mass subsets would differ significantly, which is not the case observed here. Regardless of the shape of the attenuation curve assumed for the reddening of the SPS models, we find that the estimated stellar metallicities for the low- and high-mass subsets are consistent within the 3σ measurement uncertainties. Considering this finding, it is more likely that the alternative explanation, where the shape of the nebular attenuation curve differs for high SFR galaxies compared to low SFR ones, is true.

4.5   Summary and Conclusion

In the first part of this analysis, we examine the agreement between Hα and SED-inferred SFRs for different stellar population assumptions using a sample of 412 MOS-DEF galaxies with deep rest-frame optical spectra (Figure 4.2). Comparing models with metallicities of $0.07\,Z_\odot$ and $1.41\,Z_\odot$, we find that the best agreement between SFR[Hα] and SFR[SED] is achieved with subsolar metallicity models reddened by the SMC curve and solar metallicity models reddened by the Calzetti curve. Investigating discrepan-
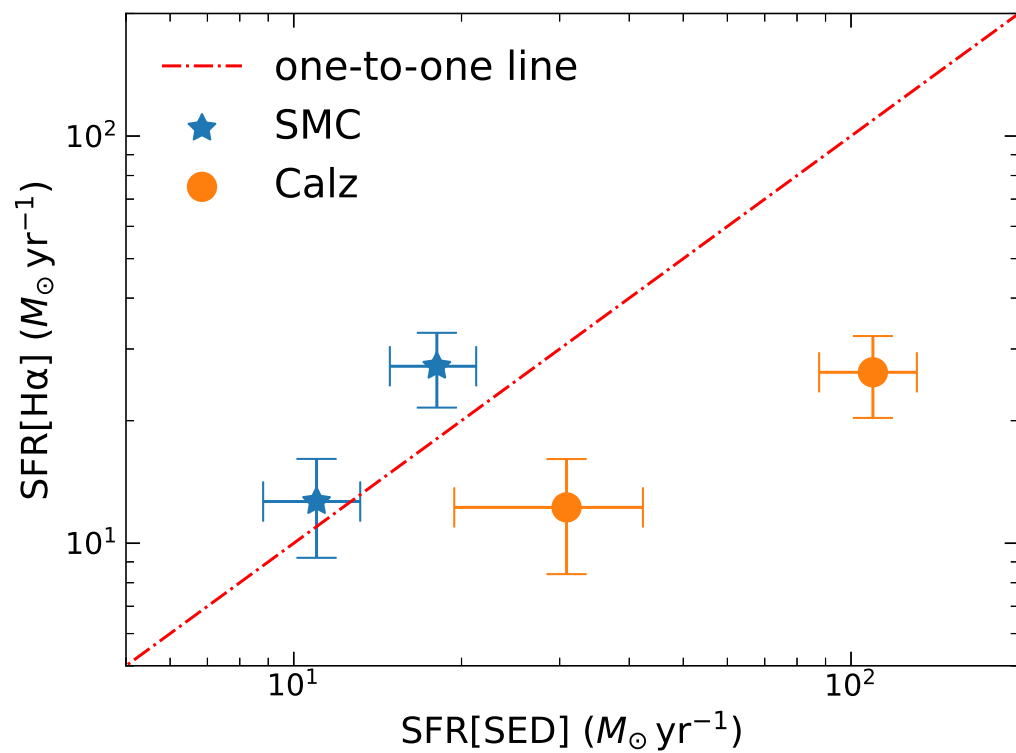
Figure 4.5: ⟨SFR[Hα]⟩ versus ⟨SFR[SED]⟩ derived from the rest-frame optical and FUV spectra for the two stellar mass bins listed in Table 4.1. Orange circles and blue stars indicate the derived average SFRs using the SPS models reddened with the Calzetti and SMC curve, respectively.

cies between Hα and SED-inferred SFRs, we focus on the role of differential reddening $(E(B-V)_{\text{neb}} - E(B-V)_{\text{cont}})$ and find that discrepancies between the two SFRs increase as differential reddening rises. In particular, SFR[Hα] is found to be significantly larger than SFR[SED] for galaxies with very high differential reddening values. We propose that these discrepancies could be due to the separation of the regions responsible for the majority of optical and UV emissions. To further investigate this possibility, we examine the bolometric SFR of sample galaxies.

In the second part of this analysis, we examine the bolometric SFR by combining both dust-obscured SFR from IR emission and unobscured SFR from UV emission. This allows us to investigate into the disconnection between IR and UV/optical emissions. When stacking sample galaxies into bins of SFRs, we find discrepancies between SFR[IR+UV] and both SFR[Hα] and SFR[SED], especially in lower SFR bins (Figure 4.4). We attribute these discrepancies to optically-thick star-forming regions in a galaxy, hosting most of its star formation. We find a good agreement between the average bolometric SFR and both SFR[Hα] and SFR[SED] for high SFR bins. Given this result, the discrepancies between Hα and SED-inferred SFRs for those galaxies with high SFRs cannot be attributed to decoupling between the less-reddened regions dominating the UV emission and the dust-obscured regions dominating the Hα emission. This finding suggests that SFR[Hα] might be overestimated at high SFRs. It is possible that such galaxies follow a nebular attenuation curve that is either steeper at rest-optical wavelengths or has a lower R_{V} compared to galaxies with lower SFRs. As proposed by Reddy et al. (2020), to investigate possible variations of the nebular attenuation curve with physical properties of a $z \sim 2$ galaxy such

as SFR, a larger sample with high S/N detection of the Balmer and longer wavelength Paschen lines is required.

Another factor that can lead to the overestimation of SFR[Hα] is stellar metallicity, as higher metallicity models have higher conversion factors relating $L(\mathrm{H}\alpha)$ and SFR[Hα]. We investigate the possible variation of the stellar metallicity among MOSDEF/LRIS sample galaxies by dividing the sample into two subsets with low and high stellar mass. We stack the rest-frame FUV spectra of galaxies in each subset and fit the stacked spectra with SPS models to constrain the stellar metallicity of each bin. We find that, regardless of the attenuation curve assumed for the reddening of the SPS models, the estimated stellar metallicities of the low- and high-mass subsets are within the range of subsolar metallicity ($\sim 0.2\,Z_{\odot}$) and consistent within 3σ measurement uncertainties. Our findings confirm that variation in the stellar metallicity of sample galaxies cannot be the reason for the discrepancies observed between SFR[Hα] and SFR[SED] for high SFRs.

We also analyze the average SFR[Hα] and SFR[SED] of the low- and high-mass subsets derived from the rest-frame optical and FUV composite spectra to investigate potential variations in the stellar attenuation curve with stellar mass. Our findings show that models reddened with the SMC curve provide the best agreement between the mean Hα and SED-inferred SFRs for both low- and high-mass subsets. This result supports the earlier conclusion that the SMC curve is better suited for galaxies with sub-solar metallicities in terms of reconciling SFRs, given that the estimated stellar metallicities for both low- and high-mass subsets are consistent and close to sub-solar metallicity.

Our results indicate a connection between the shape of the stellar dust attenuation curve and stellar metallicity. Given that many essential galaxy properties are determined through SED modeling, which is highly dependent to the impact of dust reddening, it is crucial to constrain dust curves to obtain more reliable inferred quantities.

Chapter 5

Conclusions

We study the variation of the nebular and stellar dust attenuation curves with the properties of local and $z \sim 2$ star-forming galaxies, respectively. We also examine the reliability of the Hα-to-UV luminosity ratio as a commonly used tracer of bursty SFH for a sample of $z \sim 2$ galaxies. We use the Sloan Digital Sky Survey (SDSS) data release (DR8) (Aihara et al. 2011) for our study of local galaxies. The MOSFIRE Deep Evolution Field (MOSDEF) Kriek et al. (2015), MOSDEF/LRIS (Topping et al. 2020), and 3D/HST surveys are used for our studies of $z \sim 2$ galaxies (Brammer et al. 2012; Skelton et al. 2014; Momcheva et al. 2016). An average nebular attenuation curve for local star-forming galaxies with a redshift range of $0.04 < z < 0.1$ was derived in Chapter 2. A morphology analysis using resolved HST imaging of $1.37 < z < 2.61$ galaxies with the focus on the resolved distribution of star-formation-rate surface density as well as stellar age and their correlations with the globally measured Hα-to-UV luminosity ratio was described in Chapter 3. In addition, Chapter 3 presented a stacked analysis of rest-FUV spectroscopy using the Keck

Low Resolution Imager and Spectrometer (LRIS) to examine the correlation between the average Hα-to-UV ratio and the strength of the P-Cygni and stellar wind spectral features. Using stellar population synthesis models along with observations from the MOSDEF and MOSDEF/LRIS surveys, reconciliation of the observed and model-based star-formation rates was described in Chapter 4.

5.1 Broader Implications and Addressed Questions

The questions that were addressed in this dissertation are as follows:

1. How does the nebular dust attenuation curve varies with physical properties of local star-forming galaxies?

2. Is Hα-to-UV luminosity ratio a reliable tracer of bursty SFH at $z \sim 2$ galaxies?

3. What are the optimum stellar metallicity and dust attenuation curve combinations that bring the best agreement between the observed and model-based SFRs?

The first question was addressed in Chapter 2 where the average nebular attenuation curve derived for the sample galaxies was similar to that of the MW curve (Cardelli et al. 1989b) in terms of shape and normalization. No varition was found in the shape of the nebular attenuation curve with physical properties of the sample galaxies such as stellar mass, sSFR, and gas-phase abundances. Since the nebular attenuation curve serves as the foundation for determining many key properties of the ISM in galaxies, this study holds significant importance in the field of galaxy evolution.

The second question was addressed in Chapter 3 where our results cast doubt upon the reliability of the Hα-to-UV luminosity ratio in tracing bursty SFH of typical

star-forming galaxies at $z \sim 2$. One significant implication of this study relates to the hypothesis that star-forming galaxies may enter a bursty phase of star formation at the onset of the reionization epoch, generating sufficient ionizing photons to reionize the intergalactic medium. If this is true, it is crucial to verify the burstiness tracer commonly employed in existing literature and to identify any other factors that could influence the Hα-to-UV ratio.

The third question was tackled in Chapter 4, where our findings revealed a connection between stellar metallicity and the stellar dust attenuation curve. We found that subsolar metallicity models reddened with the SMC curve (Gordon et al. 2003a) and solar metallicity models reddened with the Calzetti curve (Calzetti et al. 2000b) most accurately represent the observed star formation rates of the sample galaxies. Given that many essential galaxy properties are determined through SED modeling, which is highly dependent to the impact of dust reddening, it is crucial to constrain dust curves to obtain more reliable inferred quantities.

5.2   Future Work

The work presented in Chapter 2 of this dissertation (and also the work presented in Reddy et al. 2020) can be extended using James Webb Space Telescope spectroscopic data with detection of the Balmer, Paschen, and Bracket recombination lines (Reddy et al. 2023). Varition of the neular attenuation curve with SFR may potentially be one of the reasons for the discripencies found between the observed and model-based SFRs. To investigate such

possibility, a large number of galaxies with high S/N spectroscopic data is required (Reddy et al. 2020).

The work presented in Chapter 3 can be extended using JWST resolved imaging. Either a pixel-by-pixel or Voronoi binning SED fitting can be used to make resolved maps of the dust, stellar mass, and star-formation properties of bursty and non-bursty systems. Such maps would give insight into how SF activity is distributed in galaxies (e.g., central, disk, clumpy, etc.).

Bibliography

Aihara, H., Allende Prieto, C., An, D., et al. 2011, ApJS, 193, 29, doi: 10.1088/0067-0049/193/2/29

Aird, J., Coil, A. L., & Georgakakis, A. 2017, MNRAS, 465, 3390, doi: 10.1093/mnras/stw2932

Andrews, B. H., & Martini, P. 2013, ApJ, 765, 140, doi: 10.1088/0004-637X/765/2/140

Asplund, M., Grevesse, N., Sauval, A. J., & Scott, P. 2009, Annual Review of Astronomy and Astrophysics, 47, 481, doi: 10.1146/annurev.astro.46.060407.145222

Asquith, R., Pearce, F. R., Almaini, O., et al. 2018, MNRAS, 480, 1197, doi: 10.1093/mnras/sty1870

Atek, H., Furtak, L. J., Oesch, P., et al. 2022, MNRAS, 511, 4464, doi: 10.1093/mnras/stac360

Azadi, M., Coil, A. L., Aird, J., et al. 2017, ApJ, 835, 27, doi: 10.3847/1538-4357/835/1/27

Azadi, M., Coil, A., Aird, J., et al. 2018, ApJ, 866, 63, doi: 10.3847/1538-4357/aad3c8

Basu-Zych, A. R., Lehmer, B. D., Hornschemeier, A. E., et al. 2013a, ApJ, 762, 45, doi: 10.1088/0004-637X/762/1/45

—. 2013b, ApJ, 774, 152, doi: 10.1088/0004-637X/774/2/152

Battisti, A. J., Calzetti, D., & Chary, R. R. 2016, ApJ, 818, 13, doi: 10.3847/0004-637X/818/1/13

—. 2017, ApJ, 840, 109, doi: 10.3847/1538-4357/aa6fb2

Bauer, F. E., Alexander, D. M., Brandt, W. N., et al. 2002, AJ, 124, 2351, doi: 10.1086/343778

Bertin, E., & Arnouts, S. 1996, Astron. Astrophys. Suppl. Ser., 117, 393, doi: 10.1051/aas:1996164

Bianchi, L., Clayton, G. C., Bohlin, R. C., Hutchings, J. B., & Massey, P. 1996a, ApJ, 471, 203, doi: 10.1086/177963

—. 1996b, ApJ, 471, 203, doi: 10.1086/177963

Bicker, J., & Fritze-v. Alvensleben, U. 2005, A&A, 443, L19, doi: 10.1051/0004-6361:
200500194

Boselli, A., Boissier, S., Cortese, L., et al. 2009, ApJ, 706, 1527, doi: 10.1088/0004-637X/
706/2/1527

Brammer, G. B., van Dokkum, P. G., Franx, M., et al. 2012, ApJS, 200, 13, doi: 10.1088/
0067-0049/200/2/13

Brinchmann, J., Charlot, S., White, S. D. M., et al. 2004, MNRAS, 351, 1151, doi: 10.
1111/j.1365-2966.2004.07881.x

Brorby, M., Kaaret, P., Prestwich, A., & Mirabel, I. F. 2016, MNRAS, 457, 4081, doi: 10.
1093/mnras/stw284

Broussard, A., Gawiser, E., & Iyer, K. 2022, The Astrophysical Journal, 939, 35, doi: 10.
3847/1538-4357/ac94c2

Broussard, A., Gawiser, E., Iyer, K., et al. 2019, The Astrophysical Journal, 873, 74,
doi: 10.3847/1538-4357/ab04ad

Bruzual, G., & Charlot, S. 2003, MNRAS, 344, 1000, doi: 10.1046/j.1365-8711.2003.
06897.x

Buat, V., Boquien, M., Małek, K., et al. 2018, A&A, 619, A135, doi: 10.1051/0004-6361/
201833841

Buat, V., Giovannoli, E., Heinis, S., et al. 2011, A&A, 533, A93, doi: 10.1051/0004-6361/
201117264

Buat, V., Noll, S., Burgarella, D., et al. 2012a, A&A, 545, A141, doi: 10.1051/0004-6361/
201219405

—. 2012b, A&A, 545, A141, doi: 10.1051/0004-6361/201219405

Calabrò, A., Castellano, M., Pentericci, L., et al. 2021, A&A, 646, A39, doi: 10.1051/
0004-6361/202039244

Calzetti, D. 1997, AJ, 113, 162, doi: 10.1086/118242

—. 2001, PASP, 113, 1449, doi: 10.1086/324269

Calzetti, D., Armus, L., Bohlin, R. C., et al. 2000a, ApJ, 533, 682, doi: 10.1086/308692

—. 2000b, ApJ, 533, 682, doi: 10.1086/308692

Calzetti, D., Kinney, A. L., & Storchi-Bergmann, T. 1994, ApJ, 429, 582, doi: 10.1086/
174346

Cantiello, M., Yoon, S.-C., Langer, N., & Livio, M. 2007, A&A, 465, L29, doi: 10.1051/0004-6361:20077115

Capak, P., Abraham, R. G., Ellis, R. S., et al. 2007, The Astrophysical Journal Supplement Series, 172, 284, doi: 10.1086/518424

Caplar, N., & Tacchella, S. 2019, MNRAS, 487, 3845, doi: 10.1093/mnras/stz1449

Cappellari, M., & Copin, Y. 2003, Monthly Notices of the Royal Astronomical Society, 342, 345, doi: 10.1046/j.1365-8711.2003.06541.x

Cardelli, J. A., Clayton, G. C., & Mathis, J. S. 1989a, ApJ, 345, 245, doi: 10.1086/167900

—. 1989b, ApJ, 345, 245, doi: 10.1086/167900

Casey, C. M., Chapman, S. C., Beswick, R. J., et al. 2009, Monthly Notices of the Royal Astronomical Society, 399, 121, doi: 10.1111/j.1365-2966.2009.15291.x

Casey, C. M., Scoville, N. Z., Sanders, D. B., et al. 2014, The Astrophysical Journal, 796, 95, doi: 10.1088/0004-637X/796/2/95

Cassata, P., Le Fèvre, O., Charlot, S., et al. 2013, A&A, 556, A68, doi: 10.1051/0004-6361/201220969

Chabrier, G. 2003, PASP, 115, 763, doi: 10.1086/376392

Chapman, S. C., Blain, A. W., Smail, I., & Ivison, R. J. 2005, The Astrophysical Journal, 622, 772, doi: 10.1086/428082

Charlot, S., & Fall, S. M. 2000a, ApJ, 539, 718, doi: 10.1086/309250

—. 2000b, ApJ, 539, 718, doi: 10.1086/309250

Chary, R., & Elbaz, D. 2001, The Astrophysical Journal, 556, 562, doi: 10.1086/321609

Chevallard, J., Charlot, S., Wandelt, B., & Wild, V. 2013, MNRAS, 432, 2061, doi: 10.1093/mnras/stt523

Chisholm, J., Rigby, J. R., Bayliss, M., et al. 2019, The Astrophysical Journal, 882, 182, doi: 10.3847/1538-4357/ab3104

Chisholm, J., Tremonti, C., & Leitherer, C. 2018, MNRAS, 481, 1690, doi: 10.1093/mnras/sty2380

Choi, J., Conroy, C., & Byler, N. 2017, ApJ, 838, 159, doi: 10.3847/1538-4357/aa679f

Clayton, G. C. 2020, in American Astronomical Society Meeting Abstracts, Vol. 235, American Astronomical Society Meeting Abstracts #235, 217.01

Clayton, G. C., Gordon, K. D., Bianchi, L. C., et al. 2015, ApJ, 815, 14, doi: 10.1088/0004-637X/815/1/14

Coil, A. L., Aird, J., Reddy, N., et al. 2015, ApJ, 801, 35, doi: 10.1088/0004-637X/801/1/35

Collaboration, T. A., Price-Whelan, A. M., Sipőcz, B. M., et al. 2018, The Astronomical Journal, 156, 123, doi: 10.3847/1538-3881/aabc4f

Conroy, C. 2013, ARA&A, 51, 393, doi: 10.1146/annurev-astro-082812-141017

Conroy, C., Schiminovich, D., & Blanton, M. R. 2010a, ApJ, 718, 184, doi: 10.1088/0004-637X/718/1/184

Conroy, C., White, M., & Gunn, J. E. 2010b, ApJ, 708, 58, doi: 10.1088/0004-637X/708/1/58

Crowther, P. A. 2007, ARA&A, 45, 177, doi: 10.1146/annurev.astro.45.051806.110615

Crowther, P. A., Caballero-Nieves, S. M., Bostroem, K. A., et al. 2016, MNRAS, 458, 624, doi: 10.1093/mnras/stw273

da Silva, R. L., Fumagalli, M., & Krumholz, M. 2012, ApJ, 745, 145, doi: 10.1088/0004-637X/745/2/145

da Silva, R. L., Fumagalli, M., & Krumholz, M. R. 2014, MNRAS, 444, 3275, doi: 10.1093/mnras/stu1688

Daddi, E., Dickinson, M., Morrison, G., et al. 2007, The Astrophysical Journal, 670, 156, doi: 10.1086/521818

Dalcanton, J. J. 2007, The Astrophysical Journal, 658, 941, doi: 10.1086/508913

Dale, D. A., Beltz-Mohrmann, G. D., Egan, A. A., et al. 2016, AJ, 151, 4, doi: 10.3847/0004-6256/151/1/4

Dale, D. A., Anderson, K. R., Bran, L. M., et al. 2020, AJ, 159, 195, doi: 10.3847/1538-3881/ab7eb2

De Barros, S., Reddy, N., & Shivaei, I. 2016, ApJ, 820, 96, doi: 10.3847/0004-637X/820/2/96

de Mello, D. F., Schaerer, D., Heldmann, J., & Leitherer, C. 1998, ApJ, 507, 199, doi: 10.1086/306317

de Mink, S. E., Langer, N., Izzard, R. G., Sana, H., & de Koter, A. 2013, The Astrophysical Journal, 764, 166, doi: 10.1088/0004-637x/764/2/166

Dickey, C. M., Starkenburg, T. K., Geha, M., et al. 2021, ApJ, 915, 53, doi: 10.3847/1538-4357/abc014

Dobbs, C. L., & Pringle, J. E. 2009, MNRAS, 396, 1579, doi: 10.1111/j.1365-2966.2009.14815.x

Domínguez, A., Siana, B., Brooks, A. M., et al. 2015, MNRAS, 451, 839, doi: 10.1093/mnras/stv1001

Douna, V. M., Pellizza, L. J., Mirabel, I. F., & Pedrosa, S. E. 2015, A&A, 579, A44, doi: 10.1051/0004-6361/201525617

Draine, B. 2003, Annual Review of Astronomy and Astrophysics, 41, 241–289, doi: 10.1146/annurev.astro.41.011802.094840

Draine, B. T., & Li, A. 2007, ApJ, 657, 810, doi: 10.1086/511055

Du, X., Shapley, A. E., Reddy, N. A., et al. 2018, ApJ, 860, 75, doi: 10.3847/1538-4357/aabfcf

Eldridge, J. J. 2012, MNRAS, 422, 794, doi: 10.1111/j.1365-2966.2012.20662.x

Eldridge, J. J., Stanway, E. R., Xiao, L., et al. 2017, PASA, 34, e058, doi: 10.1017/pasa.2017.51

Elmegreen, B. G. 2006, ApJ, 648, 572, doi: 10.1086/505785

Emami, N., Siana, B., Weisz, D. R., et al. 2019, The Astrophysical Journal, 881, 71, doi: 10.3847/1538-4357/ab211a

Erb, D. K., Shapley, A. E., Pettini, M., et al. 2006, The Astrophysical Journal, 644, 813, doi: 10.1086/503623

Faisst, A. L., Capak, P. L., Emami, N., Tacchella, S., & Larson, K. L. 2019, ApJ, 884, 133, doi: 10.3847/1538-4357/ab425b

Fanelli, M. N., O'Connell, R. W., & Thuan, T. X. 1988, ApJ, 334, 665, doi: 10.1086/166869

Feldmann, R., Quataert, E., Hopkins, P. F., Faucher-Giguère, C.-A., & Kereš, D. 2017, MNRAS, 470, 1050, doi: 10.1093/mnras/stx1120

Ferland, G. J., Chatzikos, M., Guzmán, F., et al. 2017, Rev. Mexicana Astron. Astrofis., 53, 385. https://arxiv.org/abs/1705.10877

Fetherolf, T., Reddy, N. A., Shapley, A. E., et al. 2020, MNRAS, 498, 5009, doi: 10.1093/mnras/staa2775

—. 2021, MNRAS, 508, 1431, doi: 10.1093/mnras/stab2570

Fitzpatrick, E. L., & Massa, D. 1990a, ApJS, 72, 163, doi: 10.1086/191413

—. 1990b, ApJS, 72, 163, doi: 10.1086/191413

Fitzpatrick, E. L., & Massa, D. 2007, The Astrophysical Journal, 663, 320, doi: 10.1086/518158

Fitzpatrick, E. L., & Massa, D. 2007, ApJ, 663, 320, doi: 10.1086/518158

Fornasini, F. M., Kriek, M., Sanders, R. L., et al. 2019, ApJ, 885, 65, doi: 10.3847/1538-4357/ab4653

Förster Schreiber, N. M., Genzel, R., Bouché, N., et al. 2009a, ApJ, 706, 1364, doi: 10.1088/0004-637X/706/2/1364

—. 2009b, ApJ, 706, 1364, doi: 10.1088/0004-637X/706/2/1364

Frayer, D. T., Smail, I., Ivison, R. J., & Scoville, N. Z. 2000, The Astronomical Journal, 120, 1668, doi: 10.1086/301571

Freeman, W. R., Siana, B., Kriek, M., et al. 2017, arXiv e-prints, arXiv:1710.03230. https://arxiv.org/abs/1710.03230

Fu, H., Jullo, E., Cooray, A., et al. 2012, The Astrophysical Journal, 753, 134, doi: 10.1088/0004-637X/753/2/134

Fudamoto, Y., Oesch, P. A., Faisst, A., et al. 2020, A&A, 643, A4, doi: 10.1051/0004-6361/202038163

Fujimoto, Y., Chevance, M., Haydon, D. T., Krumholz, M. R., & Kruijssen, J. M. D. 2019, MNRAS, 487, 1717, doi: 10.1093/mnras/stz641

Fumagalli, M., da Silva, R. L., & Krumholz, M. R. 2011, ApJ, 741, L26, doi: 10.1088/2041-8205/741/2/L26

Genzel, R., Tacconi, L. J., Gracia-Carpio, J., et al. 2010, MNRAS, 407, 2091, doi: 10.1111/j.1365-2966.2010.16969.x

Gilbank, D. G., Baldry, I. K., Balogh, M. L., Glazebrook, K., & Bower, R. G. 2010, MNRAS, 405, 2594, doi: 10.1111/j.1365-2966.2010.16640.x

Gilfanov, M., Grimm, H. J., & Sunyaev, R. 2004, MNRAS, 347, L57, doi: 10.1111/j.1365-2966.2004.07450.x

Glazebrook, K., Blake, C., Economou, F., Lilly, S., & Colless, M. 1999, MNRAS, 306, 843, doi: 10.1046/j.1365-8711.1999.02576.x

Goldader, J. D., Meurer, G., Heckman, T. M., et al. 2002, The Astrophysical Journal, 568, 651, doi: 10.1086/339165

Gordon, K. D., Clayton, G. C., Misselt, K. A., Land olt, A. U., & Wolff, M. J. 2003a, ApJ, 594, 279, doi: 10.1086/376774

Gordon, K. D., Clayton, G. C., Misselt, K. A., Landolt, A. U., & Wolff, M. J. 2003b, ApJ, 594, 279, doi: 10.1086/376774

Governato, F., Brook, C., Mayer, L., et al. 2010, Nature, 463, 203, doi: 10.1038/nature08640

Gräfener, G., & Vink, J. S. 2015, A&A, 578, L2, doi: 10.1051/0004-6361/201425287

Green, A. W., Glazebrook, K., Gilbank, D. G., et al. 2017, MNRAS, 470, 639, doi: 10.1093/mnras/stx1119

Grimm, H. J., Gilfanov, M., & Sunyaev, R. 2003, MNRAS, 339, 793, doi: 10.1046/j.1365-8711.2003.06224.x

Grogin, N. A., Kocevski, D. D., Faber, S. M., et al. 2011, ApJS, 197, 35, doi: 10.1088/0067-0049/197/2/35

Gutkin, J., Charlot, S., & Bruzual, G. 2016, MNRAS, 462, 1757, doi: 10.1093/mnras/stw1716

Hao, C.-N., Kennicutt, R. C., Johnson, B. D., et al. 2011, ApJ, 741, 124, doi: 10.1088/0004-637X/741/2/124

Hayward, C. C., & Hopkins, P. F. 2017, MNRAS, 465, 1682, doi: 10.1093/mnras/stw2888

Hemmati, S., Miller, S. H., Mobasher, B., et al. 2014, The Astrophysical Journal, 797, 108, doi: 10.1088/0004-637x/797/2/108

Hoang, T., Tram, L. N., Lee, H., & Ahn, S.-H. 2019, Nature Astronomy, 3, 766, doi: 10.1038/s41550-019-0763-6

Hodge, J. A., Carilli, C. L., Walter, F., et al. 2012, The Astrophysical Journal, 760, 11, doi: 10.1088/0004-637X/760/1/11

Hopkins, A. M., & Beacom, J. F. 2006, ApJ, 651, 142, doi: 10.1086/506610

Hopkins, P. F., Kereš, D., Oñorbe, J., et al. 2014, MNRAS, 445, 581, doi: 10.1093/mnras/stu1738

Hoversten, E. A., & Glazebrook, K. 2008, ApJ, 675, 163, doi: 10.1086/524095

Howell, J. H., Armus, L., Mazzarella, J. M., et al. 2010, The Astrophysical Journal, 715, 572, doi: 10.1088/0004-637X/715/1/572

Hunter, D. A., Elmegreen, B. G., & Ludka, B. C. 2010, AJ, 139, 447, doi: 10.1088/0004-6256/139/2/447

Hunter, J. D. 2007, Computing in Science & Engineering, 9, 90, doi: 10.1109/MCSE.2007.55

Iglesias-Páramo, J., Boselli, A., Gavazzi, G., & Zaccardo, A. 2004, A&A, 421, 887, doi: 10.1051/0004-6361:20034572

Jafariyazani, M., Mobasher, B., Hemmati, S., et al. 2019, ApJ, 887, 204, doi: 10.3847/1538-4357/ab5526

Johnson, B. D., Schiminovich, D., Seibert, M., et al. 2007, ApJS, 173, 392, doi: 10.1086/522960

Kashino, D., Silverman, J. D., Rodighiero, G., et al. 2013a, ApJ, 777, L8, doi: `10.1088/2041-8205/777/1/L8`

—. 2013b, ApJ, 777, L8, doi: `10.1088/2041-8205/777/1/L8`

Kauffmann, G., Heckman, T. M., Tremonti, C., et al. 2003, MNRAS, 346, 1055, doi: `10.1111/j.1365-2966.2003.07154.x`

Keel, W. C., Holberg, J. B., & Treuthardt, P. M. 2004, AJ, 128, 211, doi: `10.1086/421367`

Kennicutt, Robert C., J. 1989, ApJ, 344, 685, doi: `10.1086/167834`

Kennicutt, Robert C., J., Hao, C.-N., Calzetti, D., et al. 2009, ApJ, 703, 1672, doi: `10.1088/0004-637X/703/2/1672`

Kennicutt, R. 1998, in ESA Special Publication, Vol. 429, LIA Colloq. 34: The Next Generation Space Telescope: Science Drivers and Technological Challenges, ed. B. Kaldeich-Schürmann, 81. `https://arxiv.org/abs/astro-ph/9807188`

Kennicutt, R. C., & Evans, N. J. 2012a, ARA&A, 50, 531, doi: `10.1146/annurev-astro-081811-125610`

—. 2012b, ARA&A, 50, 531, doi: `10.1146/annurev-astro-081811-125610`

Kereš, D., Katz, N., Davé, R., Fardal, M., & Weinberg, D. H. 2009, MNRAS, 396, 2332, doi: `10.1111/j.1365-2966.2009.14924.x`

Kewley, L. J., Geller, M. J., Jansen, R. A., & Dopita, M. A. 2002, AJ, 124, 3135, doi: `10.1086/344487`

Kewley, L. J., Jansen, R. A., & Geller, M. J. 2005, PASP, 117, 227, doi: `10.1086/428303`

Knapen, J. H., & James, P. A. 2009, The Astrophysical Journal, 698, 1437, doi: `10.1088/0004-637x/698/2/1437`

Koekemoer, A. M., Faber, S. M., Ferguson, H. C., et al. 2011, The Astrophysical Journal Supplement Series, 197, 36, doi: `10.1088/0067-0049/197/2/36`

Koyama, Y., Shimakawa, R., Yamamura, I., Kodama, T., & Hayashi, M. 2019, PASJ, 71, 8, doi: `10.1093/pasj/psy113`

Kreckel, K., Groves, B., Schinnerer, E., et al. 2013, ApJ, 771, 62, doi: `10.1088/0004-637X/771/1/62`

Kriek, M., & Conroy, C. 2013, ApJ, 775, L16, doi: `10.1088/2041-8205/775/1/L16`

Kriek, M., Shapley, A. E., Reddy, N. A., et al. 2015, The Astrophysical Journal Supplement Series, 218, 15, doi: `10.1088/0067-0049/218/2/15`

Kroupa, P. 2001, MNRAS, 322, 231, doi: `10.1046/j.1365-8711.2001.04022.x`

Lamers, H. J. G. L. M., Haser, S., de Koter, A., & Leitherer, C. 1999, ApJ, 516, 872, doi: 10.1086/307127

Lara-López, M. A., Cepa, J., Bongiovanni, A., et al. 2010, A&A, 521, L53, doi: 10.1051/0004-6361/201014803

Lee, J. C., de Paz, A. G., Tremonti, C., et al. 2009, The Astrophysical Journal, 706, 599, doi: 10.1088/0004-637x/706/1/599

Lee, J. C., Gil de Paz, A., Kennicutt, Robert C., J., et al. 2011, ApJS, 192, 6, doi: 10.1088/0067-0049/192/1/6

Lehmer, B. D., Alexander, D. M., Bauer, F. E., et al. 2010, ApJ, 724, 559, doi: 10.1088/0004-637X/724/1/559

Lehmer, B. D., Brandt, W. N., Alexander, D. M., et al. 2008, ApJ, 681, 1163, doi: 10.1086/588459

Lehmer, B. D., Basu-Zych, A. R., Mineo, S., et al. 2016, ApJ, 825, 7, doi: 10.3847/0004-637X/825/1/7

Leitherer, C. 2005, A Far-Ultraviolet View of Starburst Galaxies, ed. R. de Grijs & R. M. González Delgado, Vol. 329, 89, doi: 10.1007/1-4020-3539-X_16

Leitherer, C., & Heckman, T. M. 1995, ApJS, 96, 9, doi: 10.1086/192112

Leitherer, C., Leão, J. R. S., Heckman, T. M., et al. 2001, ApJ, 550, 724, doi: 10.1086/319814

Leitherer, C., Ortiz Otálvaro, P. A., Bresolin, F., et al. 2010, ApJS, 189, 309, doi: 10.1088/0067-0049/189/2/309

Leung, G. C. K., Coil, A. L., Aird, J., et al. 2019, ApJ, 886, 11, doi: 10.3847/1538-4357/ab4a7c

Li, A., & Draine, B. T. 2001, ApJ, 554, 778, doi: 10.1086/323147

Lilly, S. J., Carollo, C. M., Pipino, A., Renzini, A., & Peng, Y. 2013, ApJ, 772, 119, doi: 10.1088/0004-637X/772/2/119

Liu, G., Calzetti, D., Hong, S., et al. 2013, ApJ, 778, L41, doi: 10.1088/2041-8205/778/2/L41

Ma, X., Hopkins, P. F., Garrison-Kimmel, S., et al. 2018, MNRAS, 478, 1694, doi: 10.1093/mnras/sty1024

Madau, P., & Dickinson, M. 2014, Annual Review of Astronomy and Astrophysics, 52, 415, doi: 10.1146/annurev-astro-081811-125615

Madau, P., Ferguson, H. C., Dickinson, M. E., et al. 1996, MNRAS, 283, 1388, doi: 10.1093/mnras/283.4.1388

Martínez-González, S., Wünsch, R., & Palouš, J. 2017, ApJ, 843, 95, doi: 10.3847/1538-4357/aa7510

Mas-Ribas, L., Dijkstra, M., & Forero-Romero, J. E. 2016, The Astrophysical Journal, 833, 65, doi: 10.3847/1538-4357/833/1/65

McLean, I. S., Steidel, C. C., Epps, H. W., et al. 2012, in Society of Photo-Optical Instrumentation Engineers (SPIE) Conference Series, Vol. 8446, Ground-based and Airborne Instrumentation for Astronomy IV, ed. I. S. McLean, S. K. Ramsay, & H. Takami, 84460J, doi: 10.1117/12.924794

McLure, R. J., Dunlop, J. S., Cullen, F., et al. 2018, MNRAS, 476, 3991, doi: 10.1093/mnras/sty522

Mehlert, D., Noll, S., Appenzeller, I., et al. 2002, A&A, 393, 809, doi: 10.1051/0004-6361:20021052

Meurer, G. R., Wong, O. I., Kim, J. H., et al. 2009, The Astrophysical Journal, 695, 765, doi: 10.1088/0004-637x/695/1/765

Miettinen, O., Delvecchio, I., Smolci´c, V., et al. 2017, A&A, 597, A5, doi: 10.1051/0004-6361/201628128

Mineo, S., Gilfanov, M., & Sunyaev, R. 2012, MNRAS, 419, 2095, doi: 10.1111/j.1365-2966.2011.19862.x

Momcheva, I. G., Brammer, G. B., van Dokkum, P. G., et al. 2016, ApJS, 225, 27, doi: 10.3847/0067-0049/225/2/27

Nanayakkara, T., Brinchmann, J., Boogaard, L., et al. 2019, A&A, 624, A89, doi: 10.1051/0004-6361/201834565

Nandra, K., Mushotzky, R. F., Arnaud, K., et al. 2002, The Astrophysical Journal, 576, 625, doi: 10.1086/341888

Nandy, K., Morgan, D. H., Willis, A. J., et al. 1980, Nature, 283, 725, doi: 10.1038/283725a0

Nandy, K., Thompson, G. I., Jamar, C., Monfils, A., & Wilson, R. 1975, A&A, 44, 195

Narayanan, D., Conroy, C., Davé, R., Johnson, B. D., & Popping, G. 2018a, ApJ, 869, 70, doi: 10.3847/1538-4357/aaed25

—. 2018b, ApJ, 869, 70, doi: 10.3847/1538-4357/aaed25

Noeske, K. G., Weiner, B. J., Faber, S. M., et al. 2007, ApJ, 660, L43, doi: 10.1086/517926

Oke, J. B., Cohen, J. G., Carr, M., et al. 1995, PASP, 107, 375, doi: 10.1086/133562

Oliphant, T. E. 2007a, Computing in Science & Engineering, 9, 10, doi: 10.1109/MCSE.2007.58

—. 2007b, Computing in Science & Engineering, 9, 10, doi: 10.1109/MCSE.2007.58

Osterbrock, D. E. 1989, S&T, 78, 491

Pannella, M., Carilli, C. L., Daddi, E., et al. 2009, The Astrophysical Journal, 698, L116, doi: 10.1088/0004-637x/698/2/l116

Papovich, C., Dickinson, M., & Ferguson, H. C. 2001, ApJ, 559, 620, doi: 10.1086/322412

Peeples, M. S., & Shankar, F. 2011, MNRAS, 417, 2962, doi: 10.1111/j.1365-2966.2011.19456.x

Pei, Y. C. 1992, ApJ, 395, 130, doi: 10.1086/171637

Pellerin, A., Fullerton, A. W., Robert, C., et al. 2002, ApJS, 143, 159, doi: 10.1086/342268

Persic, M., & Rephaeli, Y. 2007, A&A, 463, 481, doi: 10.1051/0004-6361:20054146

Persic, M., Rephaeli, Y., Braito, V., et al. 2004, A&A, 419, 849, doi: 10.1051/0004-6361:20034500

Pettini, M., Steidel, C. C., Adelberger, K. L., Dickinson, M., & Giavalisco, M. 2000, ApJ, 528, 96, doi: 10.1086/308176

Pflamm-Altenburg, J., Weidner, C., & Kroupa, P. 2007, ApJ, 671, 1550, doi: 10.1086/523033

—. 2009, MNRAS, 395, 394, doi: 10.1111/j.1365-2966.2009.14522.x

Prestwich, A. H., Tsantaki, M., Zezas, A., et al. 2013, ApJ, 769, 92, doi: 10.1088/0004-637X/769/2/92

Prevot, M. L., Lequeux, J., Maurice, E., Prevot, L., & Rocca-Volmerange, B. 1984, A&A, 132, 389

Price, S. H., Kriek, M., Brammer, G. B., et al. 2014, ApJ, 788, 86, doi: 10.1088/0004-637X/788/1/86

Quider, A. M., Pettini, M., Shapley, A. E., & Steidel, C. C. 2009, MNRAS, 398, 1263, doi: 10.1111/j.1365-2966.2009.15234.x

Reddy, N., Dickinson, M., Elbaz, D., et al. 2012, ApJ, 744, 154, doi: 10.1088/0004-637X/744/2/154

Reddy, N. A., Erb, D. K., Pettini, M., Steidel, C. C., & Shapley, A. E. 2010, ApJ, 712, 1070, doi: 10.1088/0004-637X/712/2/1070

Reddy, N. A., Pettini, M., Steidel, C. C., et al. 2012, The Astrophysical Journal, 754, 25, doi: 10.1088/0004-637x/754/1/25

Reddy, N. A., & Steidel, C. C. 2004, ApJ, 603, L13, doi: 10.1086/383087

Reddy, N. A., Steidel, C. C., Erb, D. K., Shapley, A. E., & Pettini, M. 2006a, ApJ, 653, 1004, doi: `10.1086/508851`

Reddy, N. A., Steidel, C. C., Fadda, D., et al. 2006b, ApJ, 644, 792, doi: `10.1086/503739`

Reddy, N. A., Steidel, C. C., Pettini, M., & Bogosavljević, M. 2016, ApJ, 828, 107, doi: `10.3847/0004-637X/828/2/107`

Reddy, N. A., Topping, M. W., Sanders, R. L., Shapley, A. E., & Brammer, G. 2023, arXiv e-prints, arXiv:2301.07249, doi: `10.48550/arXiv.2301.07249`

Reddy, N. A., Kriek, M., Shapley, A. E., et al. 2015, ApJ, 806, 259, doi: `10.1088/0004-637X/806/2/259`

Reddy, N. A., Shapley, A. E., Sanders, R. L., et al. 2018a, ApJ, 869, 92, doi: `10.3847/1538-4357/aaed1e`

Reddy, N. A., Oesch, P. A., Bouwens, R. J., et al. 2018b, ApJ, 853, 56, doi: `10.3847/1538-4357/aaa3e7`

Reddy, N. A., Shapley, A. E., Kriek, M., et al. 2020, ApJ, 902, 123, doi: `10.3847/1538-4357/abb674`

Reddy, N. A., Topping, M. W., Shapley, A. E., et al. 2022, ApJ, 926, 31, doi: `10.3847/1538-4357/ac3b4c`

Rezaee, S., Reddy, N., Shivaei, I., et al. 2021, Monthly Notices of the Royal Astronomical Society, 506, 3588, doi: `10.1093/mnras/stab1885`

Rezaee, S., Reddy, N. A., Topping, M. W., et al. 2022, arXiv e-prints, arXiv:2208.12371. `https://arxiv.org/abs/2208.12371`

Richards, S. N., Bryant, J. J., Croom, S. M., et al. 2016, MNRAS, 455, 2826, doi: `10.1093/mnras/stv2453`

Rieke, G. H., Alonso-Herrero, A., Weiner, B. J., et al. 2009, The Astrophysical Journal, 692, 556, doi: `10.1088/0004-637X/692/1/556`

Rix, S. A., Pettini, M., Leitherer, C., et al. 2004, ApJ, 615, 98, doi: `10.1086/424031`

Rocca-Volmerange, B., Prevot, L., Ferlet, R., Lequeux, J., & Prevot-Burnichon, M. L. 1981, A&A, 99, L5

Rodighiero, G., Renzini, A., Daddi, E., et al. 2014, MNRAS, 443, 19, doi: `10.1093/mnras/stu1110`

Salim, S., Boquien, M., & Lee, J. C. 2018, ApJ, 859, 11, doi: `10.3847/1538-4357/aabf3c`

Salim, S., & Narayanan, D. 2020, ARA&A, 58, 529, doi: `10.1146/annurev-astro-032620-021933`

Salim, S., Rich, R. M., Charlot, S., et al. 2007, ApJS, 173, 267, doi: 10.1086/519218

Salmon, B., Papovich, C., Long, J., et al. 2016, ApJ, 827, 20, doi: 10.3847/0004-637X/827/1/20

Sanders, R. L., Shapley, A. E., Kriek, M., et al. 2018, The Astrophysical Journal, 858, 99, doi: 10.3847/1538-4357/aabcbd

Saxena, A., Pentericci, L., Mirabelli, M., et al. 2020, A&A, 636, A47, doi: 10.1051/0004-6361/201937170

Schaerer, D. 1996, ApJ, 467, L17, doi: 10.1086/310193

Schaerer, D., Fragos, T., & Izotov, Y. I. 2019, A&A, 622, L10, doi: 10.1051/0004-6361/201935005

Schmidt, M. 1959, ApJ, 129, 243, doi: 10.1086/146614

Scoville, N., Faisst, A., Capak, P., et al. 2015, The Astrophysical Journal, 800, 108, doi: 10.1088/0004-637X/800/2/108

Seaton, M. J. 1979, MNRAS, 187, 73, doi: 10.1093/mnras/187.1.73P

Seibert, M., Heckman, T. M., & Meurer, G. R. 2002, The Astronomical Journal, 124, 46, doi: 10.1086/341043

Senchyna, P., Stark, D. P., Vidal-García, A., et al. 2017, MNRAS, 472, 2608, doi: 10.1093/mnras/stx2059

Seon, K.-I., & Draine, B. T. 2016, The Astrophysical Journal, 833, 201, doi: 10.3847/1538-4357/833/2/201

Shapley, A. E., Steidel, C. C., Adelberger, K. L., et al. 2001, ApJ, 562, 95, doi: 10.1086/323432

Shapley, A. E., Steidel, C. C., Pettini, M., & Adelberger, K. L. 2003, ApJ, 588, 65, doi: 10.1086/373922

Shapley, A. E., Steidel, C. C., Pettini, M., Adelberger, K. L., & Erb, D. K. 2006, ApJ, 651, 688, doi: 10.1086/507511

Shirazi, M., & Brinchmann, J. 2012, MNRAS, 421, 1043, doi: 10.1111/j.1365-2966.2012.20439.x

Shivaei, I., Reddy, N. A., Shapley, A. E., et al. 2015, ApJ, 815, 98, doi: 10.1088/0004-637X/815/2/98

Shivaei, I., Reddy, N. A., Shapley, A. E., et al. 2017, The Astrophysical Journal, 837, 157, doi: 10.3847/1538-4357/aa619c

Shivaei, I., Reddy, N. A., Siana, B., et al. 2018a, ApJ, 855, 42, doi: 10.3847/1538-4357/aaad62

—. 2018b, ApJ, 855, 42, doi: 10.3847/1538-4357/aaad62

Shivaei, I., Reddy, N., Rieke, G., et al. 2020a, ApJ, 899, 117, doi: 10.3847/1538-4357/aba35e

—. 2020b, ApJ, 899, 117, doi: 10.3847/1538-4357/aba35e

Siana, B., Teplitz, H. I., Colbert, J., et al. 2007, ApJ, 668, 62, doi: 10.1086/521185

Skelton, R. E., Whitaker, K. E., Momcheva, I. G., et al. 2014, The Astrophysical Journal Supplement Series, 214, 24, doi: 10.1088/0067-0049/214/2/24

Smail, I., Chapman, S. C., Blain, A. W., & Ivison, R. J. 2004, The Astrophysical Journal, 616, 71, doi: 10.1086/424896

Smith, L. J., Norris, R. P. F., & Crowther, P. A. 2002, MNRAS, 337, 1309, doi: 10.1046/j.1365-8711.2002.06042.x

Smith, M. V., van Zee, L., Salim, S., et al. 2021, MNRAS, 505, 3998, doi: 10.1093/mnras/stab1530

Smith, N., Götberg, Y., & de Mink, S. E. 2018, MNRAS, 475, 772, doi: 10.1093/mnras/stx3181

Somerville, R. S., & Primack, J. R. 1999, MNRAS, 310, 1087, doi: 10.1046/j.1365-8711.1999.03032.x

Sparre, M., Hayward, C. C., Feldmann, R., et al. 2017, MNRAS, 466, 88, doi: 10.1093/mnras/stw3011

Springel, V. 2000, MNRAS, 312, 859, doi: 10.1046/j.1365-8711.2000.03187.x

Springel, V., Di Matteo, T., & Hernquist, L. 2005, MNRAS, 361, 776, doi: 10.1111/j.1365-2966.2005.09238.x

Stanway, E. R., & Eldridge, J. J. 2018, MNRAS, 479, 75, doi: 10.1093/mnras/sty1353

Stanway, E. R., Eldridge, J. J., & Becker, G. D. 2016, MNRAS, 456, 485, doi: 10.1093/mnras/stv2661

Steidel, C. C., Pettini, M., & Adelberger, K. L. 2001, ApJ, 546, 665, doi: 10.1086/318323

Steidel, C. C., Shapley, A. E., Pettini, M., et al. 2004, The Astrophysical Journal, 604, 534, doi: 10.1086/381960

Steidel, C. C., Strom, A. L., Pettini, M., et al. 2016, ApJ, 826, 159, doi: 10.3847/0004-637X/826/2/159

The Astropy Collaboration, Robitaille, Thomas P., Tollerud, Erik J., et al. 2013, A&A, 558, A33, doi: 10.1051/0004-6361/201322068

Theios, R. L., Steidel, C. C., Strom, A. L., et al. 2019, The Astrophysical Journal, 871, 128, doi: 10.3847/1538-4357/aaf386

Topping, M. W., Shapley, A. E., Reddy, N. A., et al. 2020, MNRAS, 495, 4430, doi: 10.1093/mnras/staa1410

Tremonti, C. A., Heckman, T. M., Kauffmann, G., et al. 2004a, ApJ, 613, 898, doi: 10.1086/423264

—. 2004b, ApJ, 613, 898, doi: 10.1086/423264

van der Wel, A., Chang, Y.-Y., Bell, E. F., et al. 2014, ApJ, 792, L6, doi: 10.1088/2041-8205/792/1/L6

Vidal-García, A., Charlot, S., Bruzual, G., & Hubeny, I. 2017, MNRAS, 470, 3532, doi: 10.1093/mnras/stx1324

Visbal, E., Haiman, Z., & Bryan, G. L. 2015, MNRAS, 450, 2506, doi: 10.1093/mnras/stv785

Walborn, N. R., Nichols-Bohlin, J., & Panek, R. J. 1985, NASA Reference Publication, 1155

Weingartner, J. C., & Draine, B. T. 2001, ApJ, 548, 296, doi: 10.1086/318651

Weisz, D. R., Johnson, B. D., Johnson, L. C., et al. 2012, ApJ, 744, 44, doi: 10.1088/0004-637X/744/1/44

Wild, V., Charlot, S., Brinchmann, J., et al. 2011a, MNRAS, 417, 1760, doi: 10.1111/j.1365-2966.2011.19367.x

Wild, V., Groves, B., Heckman, T., et al. 2011b, MNRAS, 410, 1593, doi: 10.1111/j.1365-2966.2010.17536.x

Witt, A. N., & Gordon, K. D. 2000, ApJ, 528, 799, doi: 10.1086/308197

Wuyts, S., Förster Schreiber, N. M., Lutz, D., et al. 2011, ApJ, 738, 106, doi: 10.1088/0004-637X/738/1/106

Wuyts, S., Schreiber, N. M. F., Lutz, D., et al. 2011, The Astrophysical Journal, 738, 106, doi: 10.1088/0004-637x/738/1/106

Wuyts, S., Schreiber, N. M. F., Genzel, R., et al. 2012, The Astrophysical Journal, 753, 114, doi: 10.1088/0004-637x/753/2/114

Wuyts, S., Förster Schreiber, N. M., Nelson, E. J., et al. 2013, ApJ, 779, 135, doi: 10.1088/0004-637X/779/2/135

Yoshikawa, T., Akiyama, M., Kajisawa, M., et al. 2010, ApJ, 718, 112, doi: 10.1088/0004-637X/718/1/112

Zahid, H. J., Dima, G. I., Kudritzki, R.-P., et al. 2014, ApJ, 791, 130, doi: 10.1088/0004-637X/791/2/130

Zeimann, G. R., Ciardullo, R., Gronwall, C., et al. 2015, ApJ, 814, 162, doi: 10.1088/0004-637X/814/2/162